Doctoral Thesis

Evaluation of the Performance of the Wave Boundary Layer Model with the OpenIFS

Nefeli Makrygianni

Hydro-Environmental Research Centre

School of Engineering

Cardiff University

Supervised by:

Dr Michaela Bray, Prof. Shunqi Pan and Dr Jean Bidlot (ECMWF)

A thesis submitted in fulfilment of the requirements
for the degree of Doctor of Philosophy

July 13, 2022

Dedicated to the memory of my grandpa Philippos

Acknowledgments

First of all, I would like to thank my supervisors Prof Shunqi Pan and Dr Michaela Bray for believing in me. Especially, Prof Shunqi Pan for giving me this project. I would not be here if it wasn't for him. And Dr Michaela Bray who always supported me in the difficult moments and was a big help during the final corrections of the thesis. This thesis would not be possible without the support grant from the EPSRC (grant number EP/L016214/1).

A big thank you to my external advisor Dr Jean R. Bidlot (ECMWF) who has worked with me and helped me more than what his responsibilities required. I can easily say that without his help this project would not be the same. Jean I am entirely grateful that you were a part of my PhD. Thank you and sorry for being a pain sometimes.

I would also like to thank Dr Jianting Du and the DTU for kindly providing me with the WBLM code for SWAN, which guided me during the implementation process. I would also like to acknowledge Supercomputing Wales (SCW) for providing the resources for running the OpenIFS. Especially, I would like to thank Thomas Green from the SCW support, who was always helping me with the supercomputer and fixed anything I ruined in the Hawk system during the time I spent on it.

I would like to also thank my family for always supporting me, my mother Katia, my elder sister Danae and a special thank you to my middle sister Lydia, who was the one I was calling on the phone every time I was thinking I cannot continue. She was the one pushing me to overcome any issues and sometimes believing in me more than I believed in myself. She even proof-read conference abstracts, presentations, and she introduced me to python pandas, which was a big help to my analysis.

Here, I would also like to acknowledge my always mentor, Prof Katsafados, who never let me think for one moment to give up. After ten years, he is always the one I turn to for advice, and he never refuses to have a chat with me.

All this time would not be the same without my friends and departmental colleagues: Filipa, Ben, Giovanni, Corentin, Arthur, Pablo, Nejc, my beloved cohort girls Giulia, Catherine and Stephanie, and the one who left us but never really did, Lucy. Finally, a special thank you to my closest friends and quarantine companions Nansi, Pinelopi (who also proof-read this thesis), Laura, Pedro and Guillermo, who were the ones keeping me sane during this difficult period!

Abstract

The impact of the air–sea interactions on the atmospheric and the ocean processes has been extensively studied for over three decades, showing the importance of the input term and the transfer of momentum in the air-sea interface for wind and wave predictions. Despite the significant improvement in modelling of the atmosphere, accurate predictions of the sea state under tropical cyclone conditions still remain highly challenging. Evidence shows that the air-sea-waves interaction over the ocean surface can significantly impact on the coupled atmosphere-ocean systems, through momentum, mass, and energy exchanges. In particular, the momentum exchanges have been found to affect both the structure of the wave boundary layer and the sea state, through the wave evolution. For many decades, studies suggested different parameterisations of the momentum fluxes, through the drag coefficient (C_d) and the roughness length (z_0).

The analysis of the Wave Boundary Layer (WBL) has been used in several studies to improve the wind and wave predictions. In recent years, research has been focused on the theoretical approaches of the momentum parameterisation within the WBL in order to obtain the best computation of surface stresses. However, the WBL was used only to resolve the z_0 and C_d, but with no change in the computation of the source functions in wave models. Only recently, Du et al. (2017, 2019) proposed the use of the WBL model (WBLM) in the calculation of the input source function. However, the work was based on a standalone model, and not in a coupled system. Nevertheless, as the atmosphere and ocean need to be consider as one system the importance of fully shifting towards coupled systems, in order to improve the wind and wave predictions, has been proved even in early studies (Janssen et al., 1989; Janssen, 1991)

Based on the above, in this study the WBLM is implemented and evaluated in a coupled system (OpenIFS). The main aim is to test if and how this resent approach can improve the wind and wave predictions, and became an available source input function choice for operational forecasting. The new wind input term is then tested using numerical model simulations for four tropical cyclone cases, and its validation is based on in-situ (buoy) and altimeter (satellite) data. In addition, the WBLM, as well as the observations are compared also to the default source input function of OpenIFS (Janssen, 1991), in order to understand the possible improvements of the new approach. Results of this study hint that the use of the WBLM, reduced the commonly overestimated C_d

and in times shifts the wind and wave predictions, coming in agreement with previous studies of the literature. However, comparisons with the observations showed that in cases Janssen (1991) still gives better predictions of wind and wave. Most importantly, it is also found here that the WBLM is more computationally costly (for about 50%) than the default parameterisation, which is a key issue for operational forecasting.

Publications

Conferences

1 Makrygianni, N., Pan, S., Bray, M., and , Bidlot, J.: Evaluation of the performance of the Wave Boundary Layer Model with OpenIFS WISE Meeting, Bergen, Norway, 5 – 9 September 2021 (Oral Presentation)

2 Makrygianni, N., Pan, S., Bidlot, J., and Bray, M.: A new approach of implementation of Wave Boundary Layer in OpenIFS, EGU General Assembly 2021, online, 19–30 Apr 2021, EGU21-9617, https://doi.org/10.5194/egusphere-egu21-9617, 2021. (PICO)

3 Makrygianni, N., Bidlot, J. R., Bray, M., and Pan, S.: Implementation of the wave boundary layer model in the OpenIFS model, EGU General Assembly 2020, Online, 4–8 May 2020, EGU2020-3605, https://doi.org/10.5194/egusphere-egu2020-3605, 2020. (Poster)

Contents

List of Figures

List of Tables

Nomenclature

Abbreviations

CC	Correlation Coefficient
CDL	C_d lower bound
CDU	C_d upper bound
$IPHYS$	New model switch for source input function
JS	Janssen's Scheme
RMS	Root-mean-square error
ST	Source Term
STD	Standard Deviation
$U10$	Wind Speed at 10m
$UVISL$	Wind lower bound
$UVISU$	Wind upper bound
$WBLM$	Wave Boundary Layer Model

Greek Symbols

α	Charnock Parameter
β_g	Wave Growth Rate
β_{max}	Tunable Constant
ϵ	Air-water Density Ratio
κ	von Karman Constant
λ	Non-dimensional Critical Height
ν_a	Kinematic Air Viscosity
ϕ	Energy Density Spectrum
ρ_a	Air Density
ρ_w	Water Density
σ	Angular Frequency
τ	Total Stress
τ_ν	Viscous Stress

τ_t	Turbulent Stress
τ_{tot}	Total stress
θ	Wave Direction
θ_w	Wind Direction

Latin Symbols

C_β	Mile's Parameter
C_d	Drag Coefficient
g	Gravity Acceleration
h	Water Depth
L	Obukov Length
N	Action Density Spectrum
q	Moisture
S_{in}	Source Input
T	Temperature
U	Horizontal Component of Wind Speed (x direction)
u	Wind Speed
u_*	Friction Velocity
u_{10}	Wind Speed at 10m
V	Horizontal component of Wind Speed (y direction)
z	Reference Height
z_0	Roughness Length
z_α	Wave Age Tuning Parameter
z_c	Critical Height

Chapter 1

Introduction

1.1 Motivation

Accurate wind and wave predictions have significant impact on humans life, as well as coastal and offshore applications. In addition to every day human activities, during the last decades, accurate ocean predictability has been necessary for many social and economic sectors as well as areas of research. These cover a broad range, such as navigation, coastal overtopping, flooding due to combination of waves and surge, and as a result management of coastal structures designs, transport and offshore wind farming, as well as different areas of research (e.g. pollution studies) (Wu et al., 2018; Furevik and Haakenstad, 2012). Moreover, studies have indicated that cyclonic events have increased in frequency and magnitude. This increase mainly comes from the rise in the sea surface temperature by 0.5 degrees in the Tropics, due to the changing climate (Webster et al., 2005). During these extreme events, accurate predictions are more vital, since small errors can cause significant disruptions.

Additionally, the momentum exchanges between the atmosphere and the oceans (accompanied with other fluxes), have been found to play a significant role in the forecasting accuracy. Moreover, these exchanges (air-sea interactions) revealed that the atmosphere and the oceans are one system and hence they need to be considered as coupled. This coupling should therefore be represented in numerical models (ECMWF, 2020).

1.2 Air-Sea Interaction Overview

In general, the wave generation starts by turbulent pressure fluctuations in the air that cause small ripples on the ocean surface (Phillips, 1957). That is simply the action of the wind onto the ocean surface (wind stress), which causes the momentum transfer from the atmosphere to the sea (Peng et al., 2013). Continued interactions of the wind on the sea surface cause waves generations and storm surges.

The interactions between oceans and the atmosphere, known as air - sea or wind - wave interactions, have been proven to impact on the different processes in the atmospheric and oceanic boundary layer. Often the air - sea interactions are divided in two categories: a) the dynamical interactions, which affect the momentum and mass balance between the layers (e.g. Janssen, 2004; Edson et al., 2013) and b) the thermodynamic interactions, that are based on enthalpy exchanges (e.g. Bao et al., 2000; Drennan et al., 2003; Varlas et al., 2018). Figure 1.1 schematically shows the total number of interactions taking place at the interface between the atmosphere and the ocean, based on the exchange of momentum and mass (e.g. wind input, wind stress, dust) and enthalpy exchanges (e.g. radiation, sensible heat transfer). The focus on this thesis is on the wind and waves part.

Since air and sea constantly communicate through the coupled momentum and enthalpy exchanges, it is broadly accepted this thin layer around the Earth should be considered as one fluid system, and it should be studied as one (Bao et al., 2000).

During extreme conditions, deep understanding of wind wave interaction mechanisms becomes more crucial, as these processes have a vital role in the development and the maintenance of tropical cyclones, and mid latitude wind storms.

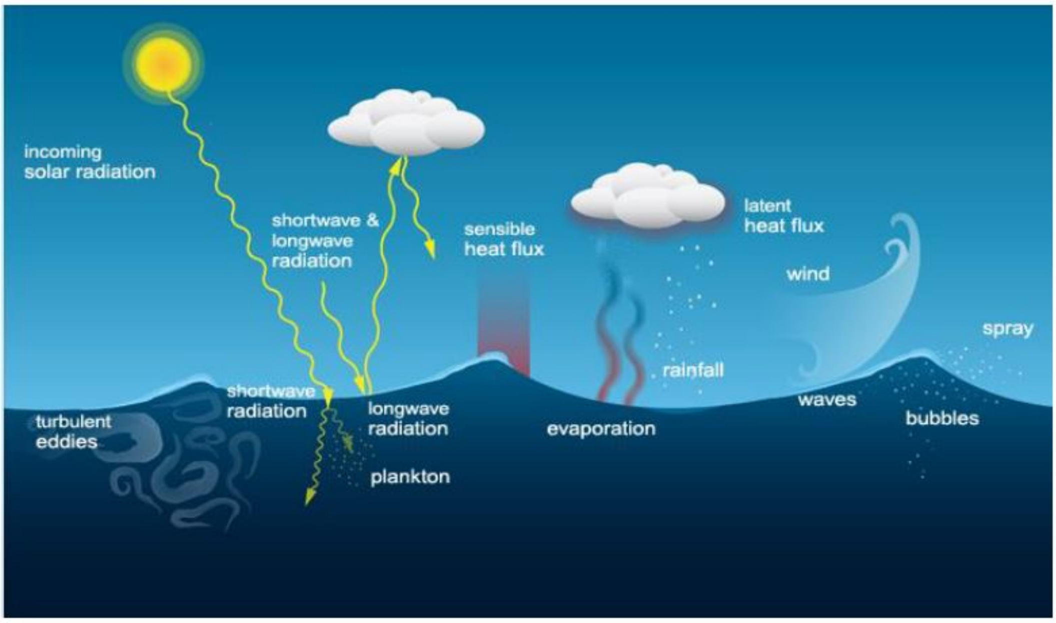

FIGURE 1.1: Schematic of all interactions in the atmosphere-ocean system. Illustration by Amy Caracappa-Qubeck, Woods Hole Oceanographic Institution.

These systems produce extreme winds, rain, and severe storm surges, which can lead to floods, and serious damages of coastal structures and renewable energy devices both inland and offshore (Fan et al., 2009; Liu et al., 2011). Under the changing climate and as the extreme events increase in frequency and magnitude, there is still limited understanding of these phenomena. Even though, wind - wave interactions, have been studied for more than three decades, they are not yet fully understood.

This limited understanding of the conditions in the air - sea interface arise from the nonlinear nature of the wind-wave interactions. These non-linear processes render an explicit physical description of the fluxes and the mechanism of exchanges elusive (Donelan and A., 1990; Komen et al., 1994; Csanady, 2001; Hristov et al., 2003).

Accurate model predictions from the models are highly dependent on the wind-forcing, water level, currents, as well as the source terms and the numerical methods used (Du et al., 2019).

Focusing on the dynamical interactions, momentum exchanges result in the specification of a roughness length scale at the interface between atmosphere and ocean. That is because the turbulence in the lower part of the atmosphere known as Wave Boundary Layer (WBL) is determined by the aerodynamic roughness and, as a result, the wind stress from the turbulence is also based on the same roughness (Johnson et al., 1999). For years, studies on the roughness, have found that one of the bigger issues in accurate predictions of the wind speeds, and wave heights, is the relatively high predicted values of drag coefficient (C_d), which is linked to the roughness during extreme winds speeds.

In addition, for many years, due to the strong link between the ocean and the atmosphere, the wave predictions have often been part of the atmospheric forecast (Bolaños-Sanchez et al., 2007; ECMWF, 2020). However, during more recent years a shift to fully coupled atmosphere-ocean-wave models has been made.

1.3 Objectives and Thesis Outline

This PhD project aims to explore and improve the description of the processes that occur in the interface between the atmosphere and the ocean. More specifically, it attempt to improve the momentum exchanges of air-sea interactions, and subsequently, the wind and wave predictions during extreme events. The project using a new method to calculate the momentum input of the winds into the waves (Du et al., 2017, 2019) that was originally introduce in a standalone model, in the coupled atmosphere-wave model OpenIFS/ECWAM, since the importance of the coupled models is nowadays clear. Simulations are made with a coupled model, in which the atmospheric and wave components communicate every timestep. Results show that this new approach successfully reduces the high values of drag coefficient, with some improvement in wind and wave predictions. However, this scheme is very recent and there is still room for improvement.

The remaining of this thesis is structured as follows:

Chapter 2 - Literature Review

For more than three decades studies worked on improving the understanding and modelling of air-sea interactions. The aim of this Chapter is to:

1. to present the basic theoretical background on the Wave Boundary Layer (WBL)
2. summarise the work previous made on the improvements of the parameterisation of the air-sea interactions and the main gaps and limitations that still exist.

For the completeness of the thesis, different approaches are presented in this Chapter, but greater focus is given on the momentum fluxes improvement and the use of coupled models.

Chapter 3: Methods and Data

The main aim of Chapter 3 is to present:

1. detailed description of the modelling of the waves, with the system used in this study,
2. overview of the code changes made in order to implement the WBLM in the modelling system, and
3. description of data used in the study.

In order to achieve these aims, the principle analytical description of the atmospheric and wave components of the system used from this study for is presented in Chapter 3. Hence, the description it may differ in other systems. For the wave part, both the default scheme (Janssen, 1991) and the new approach (WBLM) are described here. Additionally, all sources of data used, both for initial conditions as well as for validation of the model, are presented and their characteristics are explained. The model configuration is also described in this chapter.

Chapter 4: Testing of the WBLM

The new approach (WBLM) is tested on how it impacts on the diagnostics from the atmosphere and wave outputs, namely the drag and Charnock coefficients. Additionally, the possible improvements of the use of coupled systems is also important to be given. Hence, the aim of Chapter 4 is to:

1. present the impact of the new source input function on the main parameters
2. testing its sensitivity and robustness, as well as
3. the presentation of the impact of the 2-way coupling.

Chapter 5: Impact of the WBLM Scheme on Simulations During Tropical Cyclones

For the forecasting modelling, it is of great interest to improve the air-sea interactions representations and their results during extreme events. Hence, after the model is checked for its stability and main impact in Chapter 4, Chapter 5 aims to

1. analyse the impact of the WBLM during tropical cyclone periods, both globally and locally in the area of the cyclonic events.

In order to achieve this aim, four different case studies of tropical cyclones are tested for the impact of WBLM on the main parameters (C_d and Charnock coefficient) compare to the default scheme. The comparisons are made in global scale using the initial conditions for each case study, as well as in wind and waves results, both globally and locally in the area of the cyclones.

Chapter 6: Validation of WBLM with in-situ Observations

Comparing the WBLM with the default source input function parameterisation, can give a good representation of the changes that the new approach makes in the foresting outputs. However, in reality the main aim is the improvement of the wind and wave predictions. That can only be seen by comparing the model results with real observations. Hence, the aim of this chapter is to:

1. validate the model predictions based on in-situ (buoy) data, as well as

2. testing if the WBLM improves the predictions compare to the default parameterisation.

In order to achieve these aims, this chapter focuses on comparisons of the modelled wind speeds and significant wave height using in-situ (buoy) observations, and comparing with results from the default scheme. The validation is made for the locations of the cyclones, while comparisons are made for wind and wave observations, as well as minimum sea level pressure and the trajectory of the cyclones. Appropriate stations were chosen based on the trajectory of the cyclones. At the same time, basic statistical analysis of the model results, from both schemes compare to the the observations is made.

Chapter 7: Validation of WBLM with Altimeter Data

As data from buoys are covering only one point and in areas are spares with not many stations to cover the whole area, other data sources are needed for increasing the sample. Hence Chapter 7 aims to:

1. increase the sample of observations and validate the model results with altimeter (satellite) data.

The process approach is similar to Chapter 6.

Chapter 8 Synthesis and Conclusions.

This chapter gives the discussion of the results and recommendations for further work on the subject. Major contributions of this thesis include:(i) the testing of the WBLM for a coupled system, and not in a standalone model, (ii) the reduction of the overestimated drag coefficient and Charnock coefficient, using the new source input function, (iii) the improvement of wind and wave predictions in cases, and finally (iv) the presentation of limitations of the WBLM for operational use. The last section of this Chapter summarise the conclusions of the study.

Chapter 2

Literature Review

2.1 The Wave Boundary Layer

If we think of the atmosphere as a domain, then the Earth's surface can be considered as a boundary of that domain. Fluxes in this boundary influence the lowest part of the atmosphere. Hence, even if the troposphere extends from the ground up to about 11 kilometres, only the first couple of kilometres are directly affected by the surface (both terrestrial and maritime). This part of the troposphere is generally known as Atmospheric Boundary Layer (or Planetary Boundary Layer), and is the layer in which all process are directly governed by Earth's surface (Stull, 1988; Arya, 2001). As a result, there are forced rapid changes to the Boundary Layer (from few hours up to a day). The processes include drag due to friction and momentum exchange with the ocean, sensible heat exchange and evapotranspiration, pollutant emission and flow alterations of the surface. The height of the boundary layer can vary in time and space from hundreds metres to few kilometres. For areas above the ocean the depth of the Atmospheric Boundary Layer is usually between 200 and 2000 m (Stull, 1988). A schematic representation of the Atmospheric Boundary Layer is shown in Figure 2.1

As shown in Figure 2.1 the Boundary Layer can mainly be divided in two sub-layers: (i) the inner layer and (ii) the outer layer.

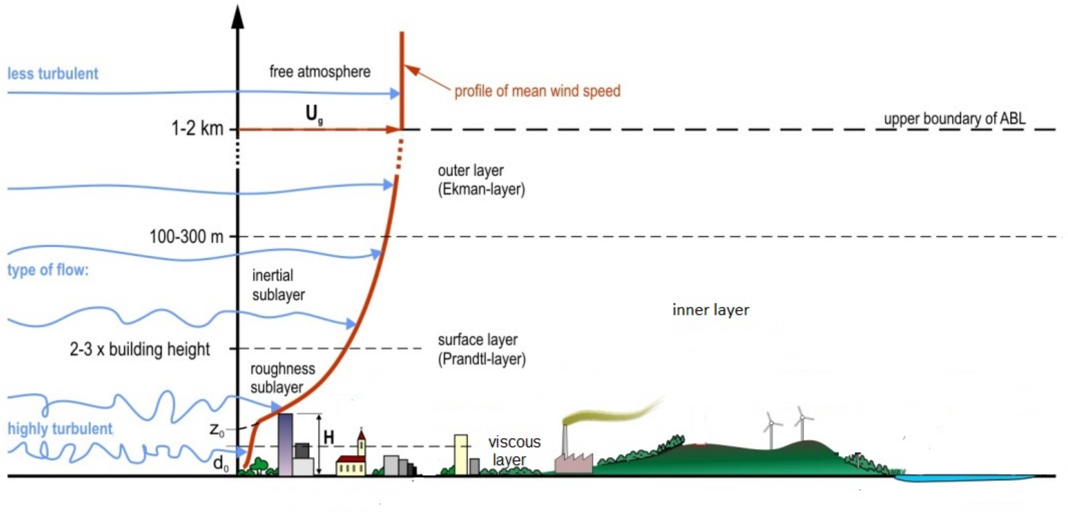

FIGURE 2.1: Schematic presentation of the atmospheric Boundary Layer. Based on illustration by Establishment of an Atmospheric Flow Laboratory (https://bmeafl.com/jav_hatarreteg_en/)

The outer layer, also known as Ekman layer, is the main part of the atmospheric boundary layer, and it is where the wind speeds are changing gradually with height, until they reach the free atmosphere and become geostrophic.

The inner layer, where most changes occur, can be further divided in extra sub-layers; the viscous and the surface layer. The viscous layer is the very thin layer touching the surface, where viscous forces are dominant. Its height reaches only some centimeters in height. Above the viscous and below the outer layer, the surface layer is expanded. This layer covers the 10% of the Atmospheric Boundary Layer depth, spanning from 20 to 200 m. Inside this layer the wind vertical gradients are strong until winds become zero on the surface. In the surface layer, wind stress is considered constant with height. In the Atmospheric Boundary Layer homogeneous stratification gives neutral conditions, while in non-neutral conditions, the stratification can be either stable (positive buoyancy) or un-stable (negative buoyancy) (Stull, 1988; Arya, 2001).

In the Marine Boundary Layer (MBL), fluxes can be divided in radiative and turbulent fluxes. The turbulent fluxes include the sensible (temperature differences) and latent (evapotranspiration) heat, transferred from the sea to the atmosphere. The momentum flux is due to the horizontal transfer of momentum. This transfer is caused by the drag of the sea surface on the wind (Taylor, 2003). In the this work, we only focus on the momentum fluxes through the wind stress. The wind (or turbulent) stress is the turbulence in the surface layer, it is considered proportional to the friction velocity and it is defined as:

$$\tau = -\rho_\alpha \overline{u'w'} = \rho_\alpha u_*^2 \tag{2.1}$$

where, ρ_α is the air density, u' and w' denote turbulent terms and u_* the friction velocity.

When there are neutral conditions (i.e. homogeneous stratification) measurements of wind speeds in different heights, showed that the profile closely follows a logarithmic shape which is described by:

$$u(z) = \frac{u_*}{\kappa} ln(\frac{z + z_0}{z_0}) \tag{2.2}$$

where u_* is the friction velocity, κ is the von Karman constant, z_0 is the roughness length and z the height in the profile.

Under non-neutral conditions the theory of Monin and Obukhov (1954) is applied, where the wind profile takes into consideration the thermal stratification through the stability correction function (ψ_m) which only depends on the dimensionless stability parameter $\xi = z/L$. The Obukhov length, L, is expressed as:

$$L = \frac{-u_*^3 T_v}{\kappa g Q_{v0}} \tag{2.3}$$

where, T_v is the is the virtual potential temperature, Q_{v0} is a kinematic virtual temperature flux at the surface and g is the gravitational constant. The dimensionless stability parameter (ξ) is positive for stable conditions, negative for unstable conditions, and close to zero for neutral conditions, with the wind profile becoming:

$$u(z) = \frac{u_*}{\kappa}[ln(\frac{z + z_0}{z_0}) - \psi(z/L)] \tag{2.4}$$

In the above formulations, the roughness length (z_0) directly impacts on the wind, which decreases as the surface roughness increases. In general, the roughness length represents the height above the surface (ocean) where wind speeds equals zero. More precisely, seven decades ago, Charnock (1955) using a reservoir of 1.6kmx1km measured the vertical distribution of the horizontal mean wind in the lowest 8m over the reservoir. Profiles were close to logarithmic. Plotting their slope u_*/k in relation to their intercept z_0, Charnock found the relationship

$$z_0 = \alpha \frac{u_*^2}{g} \tag{2.5}$$

where α is known as the Charnock's parameter.

For many years, this parameter was considered to be constant. However, as ongoing research improved the understanding of the air-sea interactions, and coupled systems, it was shown that both the Charnock parameter and the roughness length required better parameterisation in the modelling systems. Some of the most important studies on this area are presented in the next section.

2.2 Modelling of the Momentum Fluxes

Surface momentum fluxes are very important for accurate wind and wave predictions. In the modelling systems, the aerodynamic exchanges not only yield the conditions of the boundary layer in the atmospheric part, but also affect the wind - input source function for the ocean wave models (Du et al., 2019). As a result, many studies suggested that wind airflow generate waves, which increase the surface roughness as a result of the extraction of momentum and energy from the atmosphere (e.g. Janssen, 1991; Drennan et al., 2003; Du et al., 2017, 2019). Thus, successful predictions that match observations of surge and winds are highly dependent on accurate wind stress estimation (e.g. Doyle, 2002; Moon, 2005).

Without an active coupling to a wave model, wind stress is typically parameterised in forecasting models through drag coefficient (C_d) and/or the roughness length (z_0). Their parameterisation, and how to improve it, has been a research subject for more than three decades. Most studies based their wind stress estimations on various wind and wave parameters, including the 10m wind speed, wave age and wave steepness.

One of the first studies that tried to parameterise the drag coefficient (C_d) was from Wu (1982). This study suggested a calculation of C_d based on empirical methods and linked the C_d with the wind speed. The method was found to work well also under hurricane conditions.

A height wave steepness dependent parameterisation was suggested by Taylor and Yelland (2001). The parameterisation achieved a good agreement with tank and field data. The method implied that roughness changes due to limited duration or fetch are of the order of 10% or less, and was validated with reference field data. Some issues have been found for extremely young seas, with observed values being larger than the predicted ones.

Foreman and Emeis (2010) introduced a neutral drag coefficient in the wave boundary layer, for moderate to high wind speeds. Their formulation was based on field measurements reported in literature. Measurements were covering a big range of areas, such as open sea, coast and fetch limited areas. Their drag coefficient is based on mean wind speed, for a valid constant Charnock's coefficient of

0.018. Their approach showed that the magnitude of the new neutral drag coefficient has an upper limit compared to the traditional definition. This approach have been found to work well for deep water areas (i.e. no surface currents). However, it is less effective in areas of limited water depth, where the traditional definition in conjunction with Charnock's relation proved a better choice.

In their study Zijlema et al. (2012) re-evaluated the bottom friction formulation of the Joint North Sea Wave Project (JONSWAP) project (Hasselmann et al., 1973), which has observed swell in shallow waters ($kd \leq 3$ where k is wave number and d is depth). Based on observations, a different wind drag parameterisation was also presented. The new parameterisation resulted to lower values of bottom drag coefficient, compared to the earlier study using the same storm case study. The parameterisation was found to significantly impact the estimation of waves and storm surges of off-shore and coastal areas. This parameterisation is suggested for both local and swell generated waves.

One of the best known stress parameterisations, often used as a reference for new approaches, comes from the comprehensive study of Edson et al. (2013).This study focused on the momentum exchanges between the ocean and the atmosphere, based on data collected from four oceanic field experiments. The Coupled Ocean–Atmosphere Response Experiment (COARE) 3.0 bulk flux algorithm was refined to COARE 3.5 for high wind speeds. The results of this study showed that stresses estimations were improved, with estimations for wind speeds above 13 m/s to have significant improvement. The study also explored wave-age and slope dependent parameterisations, but it was found that a parameterisation based only on wind was satisfactory.

In a more recent study from Pineau-Guillou et al. (2018) an alternative wind stress parameterisation was proposed, based on empirically adjusted Charnock coefficient, in order to simulate wind speeds closer to the observations. For the simulations the study used the coupled wave-atmosphere model of the European Centre for Medium-range Weather Forecasts (ECMWF), IFS Cy41r1. This model was in operational use at ECMWF, between 2015 and 2016, when the Cy41r2 was published. Results showed that the new parameterisation was increasing the underestimated winds from the IFS model (Cy41r1). Moreover, simple wave - age dependent parameterisation was found to still give higher values of drag coefficient than measurements, and was therefore determined not to being appropriate for coupled models.

In one of the latest studies, Curcic and Haus (2020) estimated the drag coefficient during strong winds, in a 15m long tank in the laboratory. They were based on an older study from Donelan et al. (2004). Equally to Donelan et al. (2004) they found a saturation of C_d for large winds; however, they found an error that resulted in an overestimation of the 10m wind speed and an underestimation of the drag coefficient. In their latest study Curcic and Haus (2020) managed to correct the error, while their results kept the the saturation of the drag coefficient, without underestimating it. This correction was important, as Donelan et al. (2004) data were used in parameterisation of the surface flux in many studies and operational weather model systems for extreme conditions.

Even though, the approaches discussed until here have helped in the improvement of the wind and wave predictions, through the correction of the momentum fluxes, these approaches have many weaknesses. The main problem comes from the fact that these parameterisation schemes, are usually based on empirical methods using limited measurements that do not cover the whole range of wind and wave conditions, and more importantly during extreme events.

A theoretical approach on the parameterisation of the aerodynamic fluxes, was initially introduced by Janssen et al. (1989). In this study the quasi-linear theory of the air-sea interaction is used, in which both the air turbulence and wave impacts on the wind profile are taken into account. Results from numerical calculations for a specific wave spectrum for a steady - state wind profile showed that for young seas there is a strong coupling, since most of the stress in the boundary layer results from the momentum transfer from winds to waves. In old seas rarely any coupling was found. That proved that there is a wave-age dependence of the drag coefficient. In addition, as well as drag coefficient, it was found that wave-age impacts on the wave growth, which indicates the impact of the waves on the wind profile. Based on all the above, Janssen et al. (1989) suggested that successful wind and wave prediction can only be achieved by fully describing the momentum fluxes in the wave boundary layer, using a coupled atmospheric and ocean-wave system.

Following his previous work Janssen (1991) presented the quasi-linear theory on coupled wave forecasting. Initially, for one grid point and time evolution of the wave height, stress and drag coefficient, but also then using it for hindcast on the North Sea. Results from both methods show that the wave-induced stress significantly impacts the stress in the surface layer. This work, which is also referred as ST3, has been used by different teams and has been implemented in many wave models as source input function. Some of the most used and well known models that include the Janssen parameterisation are WAM, the wave part of the IFS model of European Centre of Mediu-Range Weather Forecasts (ECMWF) Komen et al. (1984), the SWAN developed by Delft University of Technology, in The Netherlands (DTU) Booij et al. (1999) and WAVEWATCHIII developed at NOAA/NCEP in the US (Tolman and Chalikov, 1996).

Even though wind and wave predictions were improved with the Janssen (1991) source function, the parameterisation was found to overestimate the wind stress under extreme conditions (Jenssen and Cardone, 2006). Equivalent overestimation was also observed using different wind input source functions (Moon et al., 2004, 2009). Several methods were then tried to overcome this issue and reduce the stress predictions, mainly in extreme conditions.

One of the first attempts used a cap limit of u_*/u_{10} in the range of 0.05-0.06 (Jenssen and Cardone, 2006). This work revealed that the scheme needed corrections and that further consideration of the impacts of the momentum fluxes needed further analysis. The study suggested keeping the cap limit until further corrections were published.

A popular study has been published by Ardhuin et al. (2010). This method, which is commonly referred to as Source Term 4 (ST4), can be used a maximum value of z_0 (0.0015) in the Janssen (1991) source term. Moreover, the source input term of Janssen was modified in order to include the concept of the sheltering mechanism, which helps to reduce the overestimated stress. Information for the sheltering mechanism can be found in a range of studies (e.g. Belcher and Hunt, 1993; Makin and Kudryavtsev, 1999; Kudryavtsev et al., 1999; Chen and Belcher, 2000; Hara and Belcher, 2002; Makin et al., 2007).

In a different approach, a new set of source input physics, which is commonly referred to as Source Term 6 (ST6) has been introduced by Babanin et al. (2010) and tested for both open and coastal areas, as well as for different storms intensities. In their study the input functions are observation based, meaning that the parameterisations are based on experiments. This allows the parameters to be fully calculated and the parameterisation to not be based on parameter-tuning. However, the main issue here is that the data used covered only a limited range of parameters, and so far, there have been only limited studies of this new approach in fully coupled system (e.g. Zieger et al., 2015; Christakos et al., 2020; Valiente et al., 2021).

In their attempt to fully consider the wave breaking in the open ocean, Banner and Morison (2010) introduced in Janssen (1991) the approach of the sheltering mechanism at high frequencies. That reduced the stress, as the sheltering mechanism for longer waves the turbulent stress is absorbed by the wind, and as a result shorter wave growth is reduced (Chen and Belcher, 2000). In that way the total stress in Janssen (1991) source function is replaced by the reduced stress due to the sheltering mechanism. The study showed that more accurate wind input and dissipation functions will significantly improve the wind and wave forecasts, especially on the aim of coupling the atmosphere with the oceans. The need for improvement of the understanding and prediction of the WBL, in addition to the wind input terms, was emphasised by this study.

Studies used the Wave Boundary Layer Model (WBLM), in order to include the sheltering mechanism and perform more accurate predictions of winds and waves under hurricane prediction. The WBLM takes into account the sheltering mechanism and the conservation of momentum, as well as the conservation of the Turbulent Kinetic Energy (TKE) in the WBL (Du et al., 2017).

Moon et al. (2004) explicitly calculated the wind stress using the equilibrium wave spectrum model from Hara and Belcher (2002) and the wave boundary layer model from Hara and Belcher (2004), in order to explore the impact of the momentum fluxes on the sea state. For their work they used the WAVE-WATCHIII prediction model. Runs with constant wind speeds between 10 and 45 m/s over growing and mature seas, showed that drag coefficient is generally larger for younger seas. However, they found a different trend to earlier studies, where the drag for winds above 30m/s increases with wind speed. In a later study Moon et al. (2009) investigated the impact of their method in hurricane conditions using different resolutions. The study showed that the combination of a high-resolution storm surge model and the coupled wind - wave model significantly improved the storm surge prediction in typhoon conditions. In a more recent study, Chen and Yu (2016) also used the wave boundary layer model, aiming to improve it under storm conditions. They modified the method by adding the energy dissipation through the sea spray, which is found to be crucial for air–sea interaction under extreme conditions. Results from idealised tropical cyclone runs showed that the wind stress meets its maximum value at wind speeds of about 40 m/s and after that decreases for further increase of the surface winds, which is in agreement with observations.

However, the aforementioned studies, used the WBLM only for calculating the drag coefficient and roughness length, and did not include it as a wind - input source function. Only recently Du et al. (2017, 2019) used the WBLM in order to fully calculate the wind input of the wave model SWAN. In Du et al. (2017) the source input function of Janssen (1991) was modified by introducing the wave boundary layer model as used in Moon et al. (2004). Hence, the sheltering mechanism was fully taken into account. Runs for fetch-limited cases showed that the WBLM achieved good estimations of the drag coefficient as well as wave height predictions. It was also shown that the drag coefficient for different wind speeds is related to the sea state. In Du et al. (2019) corrections in the source and dissipation term are done, improving the predictions of the drag coefficient even more.

Focusing on extreme (typhoon) winds, in their recent study Li et al. (2021) implemented a new parameterisation for roughness length in a limited area coupled model. Their work is based on the work carried out and implemented in the ECMWF operational model (CY47R1) (Bidlot et al., 2020; ECMWF, 2020).

Their parameterisation is focused on taking into consideration the reduction of roughness length under extreme conditions. Their results showed that this method can improve the model predictions of large-scale circulation, track and minimum sea level pressure under typhoon conditions.

Only recently a study carried out by the UK Met Office (Valiente et al., 2021) examined the differences in the storm predictions using the two different aforementioned physics schemes (ST4 and ST6) for the coupled model used operationally. The study used the Met Office Unified Model coupled with the WAVEWATCHIII wave model, referred as UKC4. Results showed that ST6 physics increased the momentum transfer from the atmosphere to the ocean and, compared to the ST4, of Ardhuin et al. (2010) allowed faster wave growths, with the difference between the two schemes to be greater for higher winds speeds.

Operationally at ECMWF, several changes have recently been made in order to generate a reduced drag coefficient. These changes were done in the last three versions (from IFS Cycle 47r1) of the model, and include a cap on the maximum spectral steepness, the wind input and whitecap dissipation terms of Ardhuin et al. (2010) (ST4 like), as well as a capping of Charnock coefficient for wind speeds above 33 m/s (based on the same approach as implemented later in Li et al. (2021)). Simulations for tropical cyclones showed improvement on the minimum central pressure - maximum wind speeds relation (Bidlot et al., 2020).

Chapter 3

Methods and Data

3.1 Introduction

This chapter provides a description of the methods and data used for this PhD project. A brief explanation of the atmospheric core of the model is given. For the wave part of the model, the calculation of the source input function and the details of the two different parameterisations used are also presented. The two schemes are the default parameterisation used in ECWAM model of OpenIFS Cy40r1v2, which is based on the theoretical approach from Janssen (1991), and the recent approach of the WBLM scheme that follows Du et al. (2017, 2019), and was implemented in the model during the project. The basic calculations for the stresses, the drag coefficient and the wind profile are given for both source input functions, while their main differences are pointed out. Furthermore, an overview of the changes of the code is provided, in order to better describe the required actions for the implementation of the scheme in the model. The description of the case studies used for the analysis, as well as the data for the model validation in the last sections of the chapter are outlined.

3.2 Model description

For this project the OpenIFS cycle 40r1v2 (released in October 2018) is used for the implementation of the scheme and the simulations for both the WBLM and Janssen (1991). This version of the OpenIFS was based on the IFS cycle40r1, which was the operational model used by ECMWF from 19th of November 2013 to 12th of May 2015. In general model's cycle 40 was important since it was the first time that vertical levels had been increased from 91 to 137 (with the option of 91 levels to remain). In addition, the wave model was made available, with coupled simulations active from initial time. OpenIFS 40r1v2 was the third release of that cycle after 40r1 and 40r1v1.1. This version had only minor corrections and changes from the two previous releases, which were necessary for correcting the atmospheric simulations. For that reason the forecasts taken from the latter version were different from the forecasts taken from the other two. Some corrections included evaluation packages for the users, as well as protections from overflow variables for the long runs. Corrections in the coupled runs were also made. It is important to point out here that as the operational model version used in ECMWF, is significantly ahead the open versions of the model. As a result some futures (e.g. the wave current interactions) are not available in the open versions. So, one need to keep in mind that anything discussed here about the capabilities of the model is for the version used in this project only, as some capabilities of this version may be significantly different from the operational forecast.

The following two subsections briefly describe the atmospheric and wave parts of the model, and provide a brief description of how the coupling works. The information for these sections has been taken from the User Guide (IFS documentation) of the model, that can be found on ECMWF's website. For a more detailed description the same document is recommended (ECMWF, 2013).

3.3 Modelling the Atmosphere

As in most forecasting models OpenIFS transports are calculated from the continuity equations. Specifically, OpenIFS use the Eulerian reformulation of the continuous equation. Firstly, a semi-Lagrangian version of the ECMWF spectral model was developed in order to modify the Eulerian vorticity-divergence (ζ – D) to a U-V formulation, with U and V the known horizontal components of the wind speed defined as $U = ucos\theta$ and $V = vcos\theta$ respectively, and θ the latitude, based on the momentum, thermodynamic and moisture equations which are given by:

$$\frac{\partial U}{\partial t}+\frac{1}{\alpha cos^2\theta}\{U\frac{\partial U}{\partial \lambda}+Vcos\theta\frac{\partial U}{\partial \theta}\}+\dot{\eta}\frac{\partial U}{\partial \eta}-fV+\frac{1}{\alpha}\{\frac{\partial \phi}{\partial \lambda}+R_{dry}T_v\frac{\partial}{\partial \lambda}(lnp)\} = P_U+K_U \tag{3.1}$$

$$\begin{aligned}\frac{\partial V}{\partial t} + \frac{1}{\alpha cos^2\theta}\{U\frac{\partial V}{\partial \lambda} + Vcos\theta\frac{\partial V}{\partial \theta} + sin\theta(U^2+V^2)\} + \dot{\eta}\frac{\partial V}{\partial \eta} \\ +fU + \frac{cos\theta}{\alpha}\{\frac{\partial \phi}{\partial \theta} + R_{dry}T_v\frac{\partial}{\partial \theta}(lnp)\} = P_V + K_V\end{aligned} \tag{3.2}$$

where,

$$T_v = T[1 + \{(R_{vap}/R_{dry}) - 1\}q] \tag{3.3}$$

$$\frac{\partial T}{\partial t} + \frac{1}{\alpha cos^2\theta}\{U\frac{\partial T}{\partial \lambda} + Vcos\theta\frac{\partial T}{\partial \theta}\} + \dot{\eta}\frac{\partial T}{\partial \eta} - \frac{\kappa T_v \omega}{(1+(\delta-1)q)p} = P_T + K_T \tag{3.4}$$

$$\frac{\partial q}{\partial t} + \frac{1}{\alpha cos^2\theta}\{U\frac{\partial q}{\partial \lambda} + Vcos\theta\frac{\partial q}{\partial \theta}\} + \dot{\eta}\frac{\partial q}{\partial \eta} = P_q + K_q \tag{3.5}$$

$$\frac{\partial}{\partial t}(\frac{\partial p}{\partial \eta}) + \nabla(v_H \frac{\partial p}{\partial \eta}) + \frac{\partial}{\partial \eta}(\dot{\eta}\frac{\partial p}{\partial \eta}) = 0 \tag{3.6}$$

The discretisation is divided into the model in vertical, horizontal and time. For the vertical discretisation of U,V,T and q the atmosphere is divided in n number of layers, which are defined by the pressure the half layers interfaces as:

$$p_{k+1/2} = A_{k+1/2} + B_{k+1/2}p_s \tag{3.7}$$

where k is the number of the level, A and B are constants that define the vertical coordinates and p_s is the surface pressure.

The A, B values are then stored in the GRIB header of all the fields that are archived by the model to allow the rebuild of the full pressure, with the prognostic variable to be defined with their full - level pressure. Values of the full - level pressure are not explicitly required from the vertical finite - difference scheme.

Horizontally, the Gaussian grid is used. This method allows the latitude points to be selected in a way where the local east-west grid length remains approximately constant. In this version a small amount of noise close to the poles was successfully removed by increasing the grid points in the three most northerly and southerly rows.

The time discretisation, including the semi-implicit corrections, had the form of:

$$\delta_t X = (X^+ - X^-)/2\Delta_t \tag{3.8}$$

and in second order:

$$\Delta_{tt} X = (X^+ - 2X + X^-) \tag{3.9}$$

where X is the value of a parameter at time t, X^+ is the value of the parameter at time $(t + \Delta_t)$, and X^- is the value of the parameter at time $(t - \Delta_t)$.

Based on the vertical exchanges, the main prognostic variables (u,v,T and q) are computed by the parameterisation of the turbulent transfer of the momentum, heat and moisture. The computation of these is made in two layers, the lowest part of the atmosphere (surface layer) and the outer layer, in which the same variables are predicted plus the liquid and ice water between the layers (q_l, q_i). These predictions made in an implicit time-step from t to t+1, with all the prognostic computations are made in the t time-step. For this version of the model there is still explicit division of the land and ocean points, and no full mixture of land and ocean is made. This means that each grid point is either land or water/ice.

For the surface and the outer layers the calculations of the vertical turbulent transports are made differently. For the surface layer the use of K-diffusion closure is used, while for the outer turbulent layer in addition to the K-diffusion turbulent closure, the Eddy-Diffusivity Mass-flux is used for the well -mixed unstable parts of the boundary layer (mixed layer).

Generally for any variable ϕ the vertical turbulent transport is described as:

$$\frac{\partial \phi}{\partial t} = \frac{1}{\rho}\frac{\partial}{\partial z}(\rho K_\phi \frac{\partial \phi}{\partial z} - M(\phi_u - \bar{\phi})) = \frac{1}{\rho}\frac{\partial J_\phi}{\partial z} \tag{3.10}$$

where, J_ϕ is the vertical turbulent flux and K_ϕ is the exchange coefficient.

Here we focus on the surface layer which in the model is between the lower model level (about 10 metres above surface) and the surface. OpenIFS assumes that the turbulent fluxes are constant with height, keeping their surface values, and can be described using the Monin-Obukov similarity theory. The theory describes the wind energy and humidity gradients, and specifically for wind it gives:

$$\frac{\kappa z}{u_*}\frac{\partial u}{\partial z} = \Phi_M(\frac{z}{L}) \tag{3.11}$$

The scaling parameter of friction velocity u_* is given based on the surface fluxes J_ϕ as:

$$\rho u_* = J_M \tag{3.12}$$

and L is the stability parameter called Obukov length given by:

$$L = -u_*^3/(\frac{\kappa g}{T_n}Q_0v) \tag{3.13}$$

where, Q_0v is the virtual temperature flux in the surface layer:

$$Q_{0v} = \frac{u_*s_* - (c_{pvap} - c_{pdry})T_n u_* q_*}{c_p} + \epsilon T_n u_* q_* \tag{3.14}$$

κ is the Von Karman constant (=0.4), T_n is the near surface temperature used as reference and $\epsilon = (\frac{R_{vap}}{R_{dry}} - 1)$, with $\frac{R_{vap}}{R_{dry}} - 1$, where R_{vap} and R_{dry} the vapour and dry air gas constants.

The gradient can be then integrated in the wind profile in the surface layer as:

$$u = \frac{\tau_x}{\kappa\rho u_*}\{log(\frac{z_n + z_{0M}}{L}) + \Psi_M(\frac{z_0M}{L})\} \tag{3.15}$$

and

$$v = \frac{\tau_y}{\kappa\rho u_*}\{log(\frac{z_n + z_{0M}}{L}) + \Psi_M(\frac{z_0M}{L})\} \tag{3.16}$$

where, z_{0M} is the roughness length for momentum and Ψ the stability profile function. This equation combined with the profiles for moisture and heat are used for defining the atmosphere, surface interactions, as well as for post - processing the 10m wind speed, the 2m temperature and the moisture variables.

When L reaches very small positive values, i.e. in extremely stable conditions (no wind), where the ratio z/L becomes very large, the profile shapes can become very unrealistic. In order to avoid that, z/L has a limit (=5) based on a height h where h/L=5. The profile equations are used up to that height, and above that, profiles are assumed to be uniform.

Surface fluxes are defined in the model as the difference of parameters at the first level (n) above surface (z_n) and the surface values. So for momentum:

$$J_M = \rho C_M |u_n|^2 \tag{3.17}$$

with the transfer coefficient C_M to be equal to:

$$C_M = \frac{\kappa^2}{[log(\frac{z_n + z_{0M}}{z_{0M}}) - \Psi_M(\frac{z_n + z_{0M}}{L}) + \Psi_M(\frac{z_{0M}}{L})]^2} \tag{3.18}$$

3.4 Modelling of the Waves

In this sub-section, the basic calculations for the wave part of OpenIFS (ECWAM) will be briefly presented. The comparison between the two schemes used is also given here.

In ECWAM the wave spectrum is described by the action balance equation (or energy balance equation). For deep waters this can be written as:

$$\frac{dN}{dt} = S_{in} + S_{nl} + S_{ds} \tag{3.19}$$

where $N(\sigma, \theta, \vec{x}, t) = \phi/\sigma$, being the action density spectrum, with $\phi(\sigma, \theta, \vec{x}, t)$ is the energy density spectrum. $\sigma, \theta, \vec{x}, t$ are the radian frequency, wave direction, spatial coordinate, and time, respectively. The terms on the right-hand side of Eq. 3.19 are the source terms namely: wave growth by the wind S_{in}, nonlinear four-wave interaction S_{nl}, and wave dissipation due to whitecapping S_{ds}.

The study focuses on the momentum exchange at the air-sea interface (S_{in}). S_{in} following Janssen (1991) is given by:

$$S_{in} = \gamma N \tag{3.20}$$

where β_g the growth rate found in:

$$\frac{\beta_g}{\sigma} = \epsilon C_\beta x^2 \tag{3.21}$$

with σ the angular frequency, ϵ the air–water density ratio and C_β the Miles' parameter.

3.4.1 Janssen's (1991) wind input source function (S_{in})

Early studies have tried to numerically calculate the momentum balance in the air-sea interface (e.g. Janssen et al., 1989; Janssen, 1991; Moon et al., 2004; Ardhuin et al., 2010). All studies have agreed that the rate of wave growth mainly depends on the friction velocity and the phase speed, as well as the atmospheric density stratification, the wind gustiness and the wave age.

Janssen's approach focused on the impact of the wave age on the wave growth and as a result, on the dependence of the aerodynamic drag on the sea state. Based on the assumption that even for young wind seas, where the surface is rougher, the waves are steeper and the wind profile is logarithmic, Janssen gave a theoretical approach on the parameterisation of air-sea interaction in a coupled environment, with the roughness length (z_0) to depend on the wave - induced stress (τ_w).

Based on the Miles (1957) theory the wind induced wave growth depends only on two parameters:

$$x = (u_*/c)max(cos(\theta - \theta_w), 0) \tag{3.22}$$

and

$$\Omega_m = g\kappa^2 z_0/u_*^2 \tag{3.23}$$

where, u_* is the friction velocity, c the phase speed, θ_w the wind direction, θ the direction of the waves and z_0 the roughness length. Ω_m is the profile parameter which describes the state of the air flow based on its dependence on the roughness length. As a result, the wave growth depends on the air flow and therefore the sea state (through z_0).

Based on the above and the results from numerical simulations Janssen introduced a growth rate of:

$$\beta_g = \sigma \frac{\rho_\alpha}{\rho_w} C_\beta x^2 \tag{3.24}$$

where, as before β_g is the wave growth rate, σ the angular frequency, ρ_α air density, ρ_w water density, and C_β is the Miles' parameter.

In general, the wind input source function is described as the growth rate multiplied by the action density spectrum:

$$S_{in} = \beta_g(\sigma, \theta) * N(\sigma, \theta) \tag{3.25}$$

For the growth rate β_g the ECWAM model originally uses the Janssen (1991) expression as:

$$\beta_g(\sigma, \theta) = C_\beta \sigma \frac{\rho_\alpha}{\rho_w} (\frac{u_*}{c})^2 max(cos(\theta - \theta_w), 0)^2 \tag{3.26}$$

where, c is the wave phase velocity as obtained from the dispersion relation of gravity surface waves.

The Miles parameter C_β is defined as function of non-dimensional critical height λ:

$$C_{\beta} = \frac{\beta_{max}}{\kappa^2}\lambda ln^4\lambda \tag{3.27}$$

where , $\kappa = 0.41$ is the von Kármán constant, g the gravity acceleration and $\beta_{max} = 1.2$ is a tunable constant. The non-dimensional critical height, λ, which is the height where the phase speed of the surface waves equal the wind speed, is given by:

$$\lambda = \frac{gz_0}{c^2} exp[\frac{\kappa}{(u_*/c + z_\alpha)cos(\theta - \theta_w)}], \lambda \leq 1 \tag{3.28}$$

where, g is the gravity acceleration; z_α is a tuning parameter for the wave age (ECMWF, 2013); and z_0 is the roughness length.

Originally, z_α was equal to 0.011, based on the value of β_{max}, which was derived by numerical results of the Miles theory. However, from IFS CY38R1 z_α has been reduced to 0.008, since the model was generating too much waves at low frequencies with $z_a = 0.011$. In Figure 3.1 the difference in the wave growth for the two values of z_α shows that the new value of $z - \alpha$ reduces the wind input of long waves.

Janssen (1991)'s method for the wave growth rate considers completely the wave effect on the momentum flux in the air-sea interface, through coupling of the wind and the waves. The method assumes that above the sea, in neutral conditions the wind profile has a logarithmic profile, and uses the parameterisation of Charnock (1958) for the calculation of the roughness length as:

$$u_z = \frac{u_*}{\kappa} ln(\frac{z}{z_0}) \tag{3.29}$$

while the roughness length is calculated through the Charnock relation (1958) as:

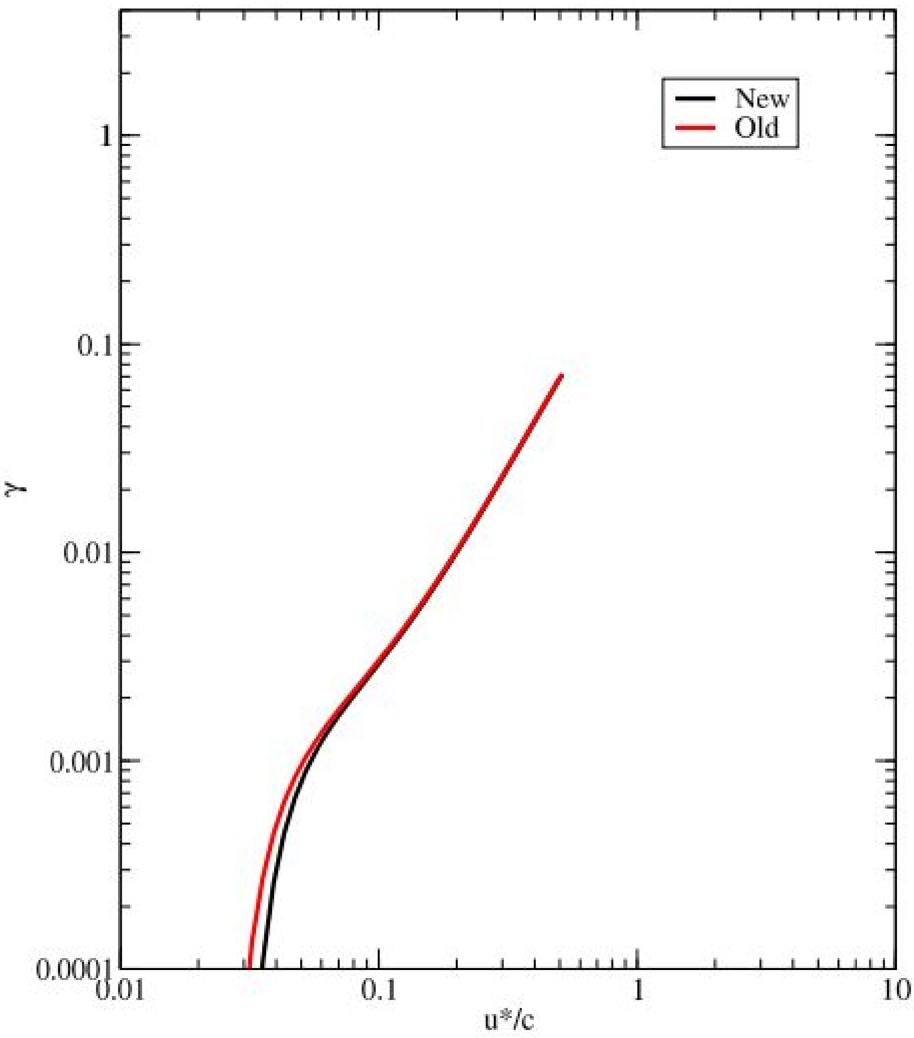

FIGURE 3.1: Non-dimensional growth rate versus the relationship between friction velocity and wave speed computed using a Charnock parameter of 0.0144 and $\alpha = 0.0144$ and z_α of 0.008 (black/new) and 0.011 (red/old). Figure taken from the IFS guide CY40R1.

$$z_0 = \alpha \frac{u_*^2}{g} \tag{3.30}$$

where the Charnock parameter (α) in Janssen (1991) depends on the wave stress as:

$$\alpha = \alpha_0 (1 - \frac{\vec{\tau}_w}{\vec{\tau}_{tot}})^{-1/2} \tag{3.31}$$

where, $\vec{\tau}_{tot}$ is the total surface wind stress; $\vec{\tau}_w$ is the wave - induced stress; and $\alpha_0 = 0.006$ for the model version used here.

The wave depended stress for Janssen (1991) is:

$$\vec{\tau}_w(z) = \rho_w \int_0^\infty \sigma^2 \beta_g(\sigma,\theta) * N(\sigma,\theta)\frac{\vec{k}}{k} d\theta d\sigma \tag{3.32}$$

where k is the wave number.

Even though the integral in Eq. 3.32 in reality extends to infinity, in the model only the low frequency part (up to about 1Hz) will be explicitly modeled. For the higher frequency part, a f^{-5} spectral shape is assumed and the higher frequency gravity-capillary waves are handled as small-scale roughness. That means that in practice, the wave stress is resolved as pointing in the wind direction, since it is basically determined by the high frequency waves, which have a fast response to the wind direction changes.

The drag coefficient (C_d) with respect to the 10m wind speed, is then derived from Eqs. 3.29 and 3.31 with $u_* = \sqrt{C_d}u_{10}$ as:

$$C_d = [\kappa/(ln(10/z_0)]^2 \tag{3.33}$$

It has been shown that in general the parameterisation Janssen (1991) wave growth rate as well as the approximation surface stress in the model, are in good agreement with observations (Wu (1982) and HEXOS respectively).

3.4.2 WBLM wind input source function (S_{in})

Du et al. (2017, 2019) aimed to improve Janssen's scheme and wind-input source term function following the Boundary Layer Model(WBLM), which was developed from Hara and Belcher (2004) and Moon et al. (2004) and is based on the momentum conservation of the atmospheric boundary layer above the sea surface (wave boundary layer).

The wave growth for the WBLM follows the sheltering mechanism, according to which the turbulent stress rather than the total stress impacts the wave growth. As a result this scheme use a modified Janssen's wave growth β_g, which is proportional to the local friction velocity, $u_*^l = \sqrt{|\vec{\tau}_t(z)/\rho_\alpha|}$ instead of the total friction velocity u_*:

$$\beta_g(\sigma,\theta) = C_\beta \sigma \frac{\rho_\alpha}{\rho_w}(\frac{u_*^l}{c})^2 max(cos(\theta-\theta_w),0)^2 \tag{3.34}$$

while Miles parameter C_β is defined as in Janssen's scheme (Eq. 3.27) with $\beta_{max} = 1.6$

Originally in Du et al. (2017) the non-dimensional critical height (λ) was derived by the assumption of a logarithmic profile following Janssen (1991) (Eq. 3.28). However, it was then found that Eq. 3.28 led to numerical instability. This is because, within the WBLM, the wind profile under the wave effect is not a logarithmic one. So, using a logarithmic profile was shown to slow down the computation and to cause the failure of the convergence for some cases. Hence, when the WBLM is used for S_{in}, λ needs to be adapted accordingly for the new wind profile.

Following Miles' theory procedure to find λ, Du et al. (2019) gave the following expression for it as:

$$\lambda = kz_c \tag{3.35}$$

where k is the wave number and z_c is the critical height, i.e. the height where the wave phase velocity c is equal to the wind speed component in the phase velocity direction

$$c = u(z_c)cos(\theta-\theta_w) \tag{3.36}$$

where $\theta - \theta_w$ is the angular separation between wind and wave directions.

Assuming that the wind profile is approximately logarithmic in the vicinity of the critical height (z_c), we have:

$$\frac{du}{dz} = \frac{u_*^l}{\kappa z} \tag{3.37}$$

The wind speed in any other height z can be found from:

$$u(z) = \frac{u_*^l}{\kappa} ln(z) + c \tag{3.38}$$

where c is constant. So by introducing 3.38 to 3.36, the wind speed at the critical height is:

$$u(z_c) = \frac{c}{cos(\theta - \theta_w)} = \frac{u_*^2}{\kappa} ln(z_c) + z_0^l \tag{3.39}$$

And the critical height z_c is computed as:

$$ln(z_c) = \frac{\kappa}{u_*^l}(U(z_c) - z_0^l) \tag{3.40}$$

$$z_c = z \cdot \exp[\frac{\kappa}{(u_*^l/c)cos(\theta - \theta_w)}] \tag{3.41}$$

So using $\lambda = kz_c$ and considering the shallow water dispersion $k = (g/c^2)tanh(kh)$, with h being the water depth, λ becomes:

$$\lambda = \frac{gz}{c^2} tanh(kh) \cdot \exp[\frac{\kappa}{(u_*^l/c)cos(\theta - \theta_w)}] \tag{3.42}$$

As equation 3.42 was found to underestimate the wave growth (Jenssen and Cardone, 2006), WAM's tuning parameter z_α =0.011 (Bidlot, 2012) was used giving:

$$\lambda = \frac{gz}{c^2} tanh(kh) \cdot \exp[\frac{\kappa}{(u_*^l/c + z_\alpha)cos(\theta - \theta_w)}] \tag{3.43}$$

Finally, λ as a function of height above the sea surface (z) is saved and passed to the next timesteps.

From Du et al. (2017) the wind profile near the sea surface is expressed for the different sub-layers divided into three options as shown in 3.44. The first part gives the heights where the profile can be considered as logarithmic, the second part is where the under wave effects the wind profile is not logarithmic and the last part is the viscous part, which is the layer in direct contact with the sea surface.

$$\begin{aligned}
\frac{d\vec{u}}{dz} &= \frac{u_*}{\kappa z}, \ z \geq \frac{g\delta}{\sigma_{min}^2} \\
\frac{d\vec{u}}{dz} &= \left[\frac{\delta}{z^2}\tilde{F}_w + \frac{\rho_\alpha}{\kappa z} \left| \frac{\vec{\tau}_t(z)}{\rho_\alpha} \right|^{\frac{3}{2}} \right] * \frac{\vec{\tau}_t(z)}{\vec{\tau}_t(z) \cdot \vec{\tau}_{tot}}, \ \frac{g\delta}{\sigma_{max}^2} \leq \ z \leq \frac{g\delta}{\sigma_{min}^2} \\
\frac{d\vec{u}}{dz} &= \frac{\rho_\alpha}{\kappa z} \left| \frac{\vec{\tau}_v}{\rho_\alpha} \right|^{\frac{3}{2}} * \frac{\vec{\tau}_v}{\vec{\tau}_v \cdot \vec{\tau}_{tot}}, \ z_v \leq \ z \leq \frac{g\delta}{\sigma_{max}^2}
\end{aligned} \tag{3.44}$$

where the viscosity term $z_v = 0.1\frac{v_\alpha}{\sqrt{|\vec{\tau}_v/\rho_\alpha|}}$, with v_α the air viscosity and

$$\tilde{F}_w = \rho_w \int_{-\pi}^{\pi} \beta_g(\sigma, \theta) g\sigma N(\sigma, \theta) d\theta \tag{3.45}$$

δ following Belcher and Hunt (1993) means $kL(k) = \delta = const.$, as the wave-induced stress penetrates a distance L(k) into the airflow.

The calculation of the WBLM based on Du's scheme starts with an initial estimation of τ_{tot} and calculates S_{in}, τ_t and τ_w for all frequencies and then calculates the wind profile. The best value for the stresses are then found through iteration and convergence process. Because of Eq. 3.44, there is relationship between height (z) and frequency (sigma). Since frequencies are discretised, so is z. Hence, the whole wind profile is calculated based on the frequencies (and therefore height), using a first guess of drag coefficient as:

$$C_d = (8.75 + 0.6214 * u_{10} - 0.005685 * u_{10}^2) * 10^{-4} \tag{3.46}$$

The roughness length for the WBLM by Du et al. (2019) is:

$$z_0 = \frac{z_{10}}{\exp\left(\kappa \frac{u_{10}}{u_*}\right)} \tag{3.47}$$

In ECMWF model, z_0 (Eq. 3.30) is computed including the viscous contribution as:

$$z_0 = \frac{\delta * \nu_\alpha}{u_*} + \alpha * u_*^2/g \tag{3.48}$$

where $\delta = 0.11$, ν_α the kinematic air viscosity $1.5 * 10^{-5}\ m^2/s$.

3.4.3 The coupled system

IFS (and therefore OpenIFS) was the first model and still is one of the limited number of models that work as fully coupled, without the need of any third part system acting as coupler, because the wave model code is fully integrated with the rest of the IFS. This helps to avoid miscomputation of the stresses.

For every coupling time step the 10m neutral winds from the atmospheric model are passed to the wave model. In return the wave model pass an updated Charnock coefficient into the atmospheric model, as resolved by the sea state in the wave model. This updates the surface roughness for the atmospheric model.

Charnock is then used in order to estimate the slowing down of the surface winds due to momentum loss with the surface in the next coupling time step (Figure 3.2).

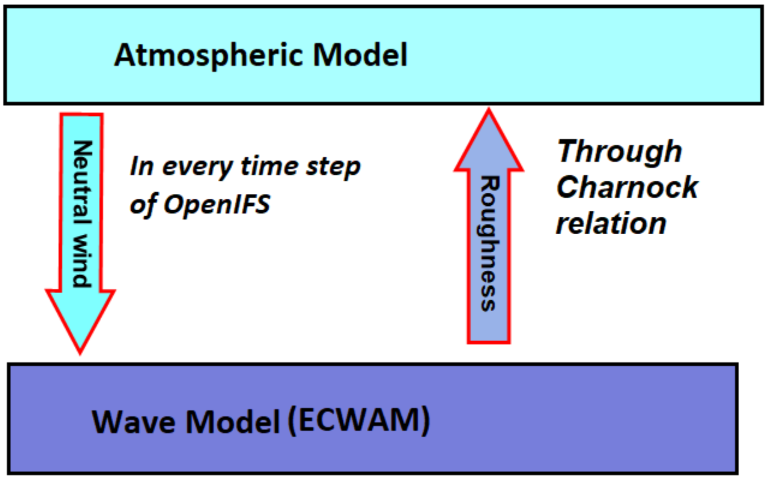

FIGURE 3.2: The coupled system in OpenIFS. Neutral winds entering the wave model (compute waves) the sea state (surface roughness) through Charnock coefficient is then updated for the atmospheric model

3.5 Model Configuration

In order to implement the WBLM scheme in the OpenIFS a new subroutine for the source input function (WBLMINPUT) was introduced in addition to the existing source input function subroutine (called SINPUT) for Janssen's source input function. For the original subroutine the wind profile is considered to be logarithmic. On the contrary, in the new subroutine the wind profile is fully calculated for each height. An important technical aspect, when new schemes are implemented in the system are the so called switches. In order to make the new subroutine callable from the model, a switch (IPHYS) has been introduced in the user and main calling subroutines of OpenIFS.

In the WBLMINPUT the process starts by calculating the first guess of the drag coefficient ($C_d = (8.75 + 0.6214 * u_{10} - 0.005685 * u_{10}^2) * 10^{-4}$), based on the estimated total stress from which the source input function is calculated. Then the wave and turbulent stresses as well as the wind profile are calculated based on the frequencies (and hence heights) discretisation (Eq. 3.44). In addition to this, a different first guess (Edson et al. (2013)) is checked, and passed in the code, in order to examine the sensitivity of the scheme in the initial C_d.

The convergence of the scheme is achieved by the secant method (Figure 3.3).

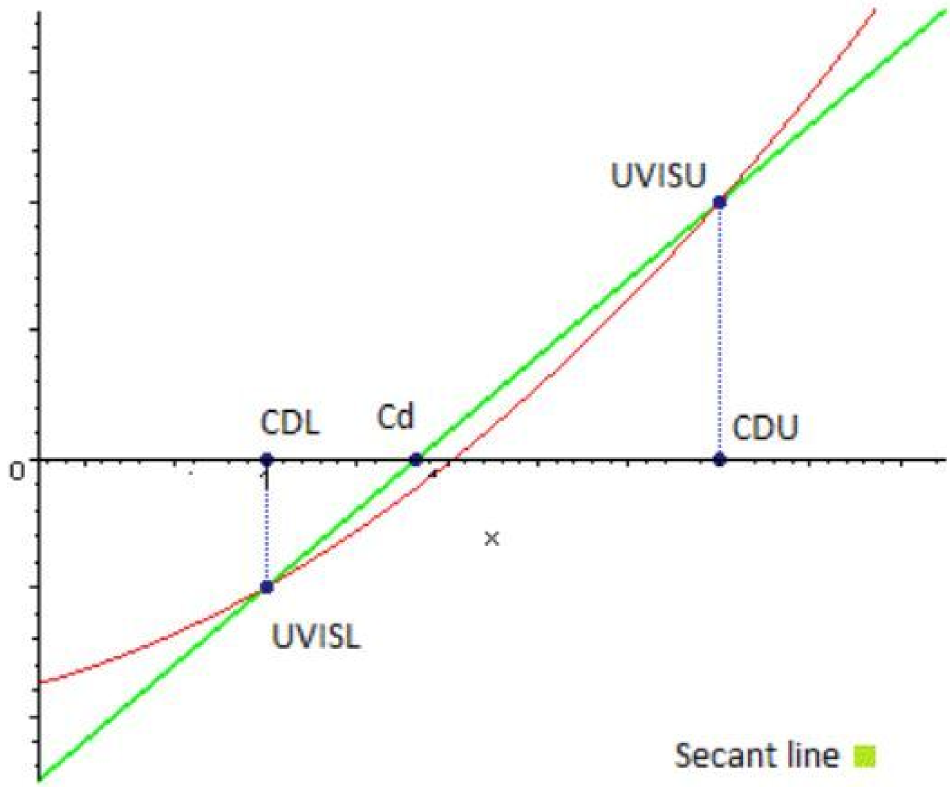

FIGURE 3.3: Illustration of the Secant method to determine C_d and its upper and lower limits.

The secant method finds the best C_d by choosing two points on either side of the first guess of the drag (C_d upper, CDU and C_d lower CDL), and their respective points of wind (UVISL, UVISU). The line where the points of (CDU,UVISU) and (CDL, UVISL) cross the x-axis is then found by calculating:

$$C_d = \frac{CDL * UVISU - CDU * UVISL}{UVISU - UVISL} \tag{3.49}$$

The C_d replaces either the CDL or CDU as follows:

C_d = CDL, if f(C_d) has the same sign as f(CDL) and,

C_d = CDU if f(C_d) has the same sign as f(CDU).

The operational system of IFS is available to run in fine resolution for different domains specified by the user. However, the open version of the model, OpenIFS, only holds the option of global simulations. The native global Gaussian grid data were interpolated to regular latitude-longitude grid for the areas of interest using Metview v.5.6.1, which was provided by ECMWF along with OpenIFS. More specifically, Metview is a meteorological workstation application for data process and visualisation, both operational and for research purposes.

The global domain runs can cause some inaccuracy in the predictions, so in order to have the best possible simulations for each point but mainly close to the coast (where most issues could occur), all runs have been performed in the highest possible spatial resolution. These are; for the atmospheric model TL1279 (16km) and for the wave model 0.25 degrees (28km). As for the vertical resolution, the option of 91 vertical layers was chosen. As the focus of interest in this study is in the wave boundary layer, it was decided that more layers would create extra computational costs, without offering any improvement on the model simulations.

The chosen resolution determines the number of directions and frequencies in the model. For the resolution of the model used here there are 36 directions and 36 frequencies. The minimum frequency is 0.035Hz and the maximum frequency is 1 Hz. The general configuration of the model is shown in Table 3.1

TABLE 3.1: Model configuration

Atm. Resolution	**Wave Resolution**	**Directions**	**Frequencies**	**Vertical Levels**	**Domain**
16 km	28 km	36	36	91	Global

Simulations are made with both options for source input functions; all cases run with the default Janssen (1991) parameterisation and the implementation of the WBLM. The simplified parameterisation of z_0 is kept when running Janssen, while the viscous correction (equation 3.48) is used with the WBLM.

Even though, the deep water mode option is still available (switch ISHALLO=1) in the model, there is a general shift to only shallow water runs (switch ISHALLO=0 or else). In this project we follow this tendency, due to the fact it has been seen that results with the deep water option it have been found to be off when comparing with buoys, mainly the ones close to the land. Hence, all the runs done and presented in the thesis are with the shallow waters option. The option of shallow water takes into consideration the water depth, which controls the maximum energy and shoaling (i.e. change in wave length but not frequency). This creates steeper waves with an increase in height and shorter wave length. However, the wave refraction option was not activated as 28 km is far too coarse for that option. Dissipative effects due to ocean bottom are also accounted for, based on Hasselmann et al. (1973). Finally, investigated the results of both options of coupled (atmosphere and wave interaction) and un-coupled runs were also performed, where the feedback from the waves to the atmosphere are not considered.

All runs were made on the Hawk system of Supercomputing Wales located in Cardiff University. For the simulations, 144 processors were used with 40 tasks per node. In order to achieve computational stability in that high resolution, a 600 second time step was used.

3.6 Case studies

The implementation was initially tested using the initial conditions of a lower impact mid-latitude storm (Storm Ciara, initial conditions 6 of February 2020). In this case a five days global forecast with 3 hours timestep was use, as the aim was to initially examine the robustness of the model. The sensitivity of the scheme was based on two drag coefficients (Edson et al. (2013) and Du et al. (2019)). Additionally the importance of the 2-way atmosphere-wave coupling is examined based on this case study. The main analysis and validation of the WBLM was based on four initial conditions datasets, during which active hurricanes were crossing the Atlantic (hurricanes Dorian with peak winds around the 6-7th of September 2019 and hurricane Teddy with peak winds on the 21st of September of 2020) or typhoons the Yellow sea (typhoon Lingling with peak winds on the 7th of September 2019 and typhoon Bavi with peak winds on the 26th of August 2020). For these cases a seven days global forecast with one hour timestep was used. The different configuration for each case study is shown in Table 3.2.

TABLE 3.2: Configuration of model runs for each case study

Case Study	2-way coupling	IPHYS	Cd	Forecast
Ciara	ON and OFF	ON and OFF	Du et al. (2019) & Edson et al. (2013)	5 days every 3 hr
Dorian	ON	ON and OFF	Du et al. (2019)	7 days every 1 hr
Teddy	ON	ON and OFF	Du et al. (2019)	7 days every 1 hr
Lingling	ON	ON and OFF	Du et al. (2019)	7 days every 1 hr
Bavi	ON	ON and OFF	Du et al. (2019)	7 days every 1 hr

3.6.1 Extratropical Cyclone

The passage of low pressure areas called extra-tropical cyclones result in strong wind and waves and they are dominant events in the mid-latitudes, including the UK Gentile et al. (2021).

Storm Ciara (3.4) was chosen because it was the most intense cyclone that hit the UK after 2014. It was formed South-East of the US in an area of weak low pressure on the February the 5th, 2020. During 8 and mainly 9 of February 2020 passed through the whole area of the UK. Its strongest gusts reached 97 mph and its minimum mean sea lever pressure was 950 hPa. Waves reached 10 m, exposing the Irish, Walsh, and Cornish coastlines, that over-topped many sea defences. In addition to its intensity, Ciara was also very interesting, as it had a complex frontal structure (with a possible frontal wave), which indicates that the boundary layer depth, rather than the temperature, influenced the cyclone characteristics (Gentile et al., 2021). This case is used for testing the scheme's stability.

3.6.2 Tropical Cyclones

For the main analysis two hurricanes (Dorian and Teddy) and two typhoons (Lingling and Bavi) were selected, as extreme conditions are the focus of interest this project.

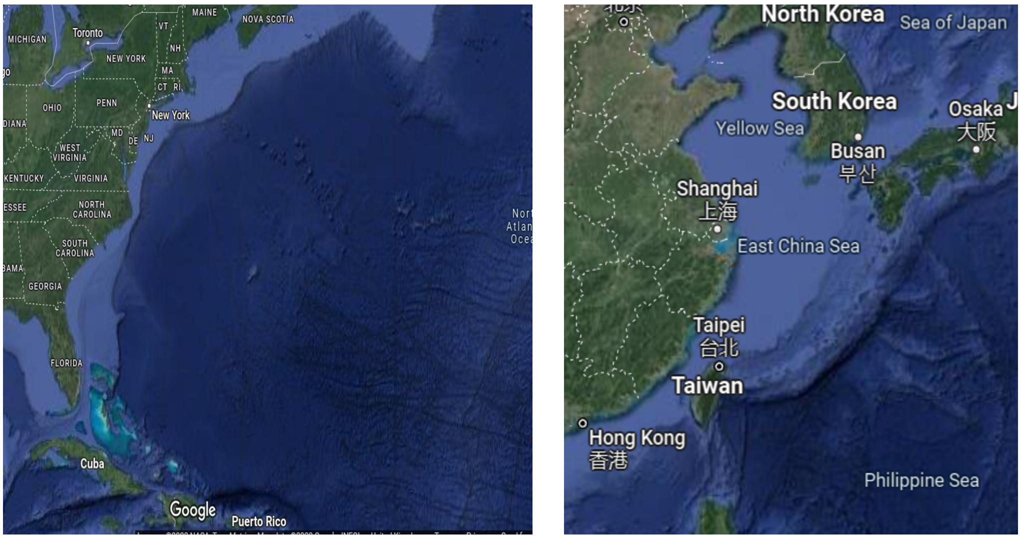

FIGURE 3.4: Areas of interest

Figure can be used as a reference for the covered area and the locations affected by the cyclones

Both hurricanes and typhoons describe the same weather phenomenon generally known as tropical cyclones. Tropical cyclones identify an organised rotating system of clouds and thunderstorms with closed, low-level circulation, that occurs above tropical and subtropical areas. At their weakest point tropical cyclones are called tropical depressions and with a minimum wind speed of 39 mph in order to initially being characterised as tropical storms. When they further intensify with winds of 74 mph and above they are described as hurricanes, typhoons or tropical cyclones depending on the region where they occur. Typhoons are found in the North Pacific, while hurricanes occur in the North Atlantic, central North and eastern North Pacific.

In order for a tropical cyclone to develop and intensify, specific atmospheric and oceanic conditions are required. These include warm tropical oceans, moisture and pre-existing weather disturbances. If these conditions persist long enough, the disturbances can evolve into these extreme cyclonic events. For the Northern hemisphere, where both hurricanes and typhoons appear, the tropical cyclone season lasts from June to November.

All tropical cyclones, regardless of the area of development, can be classified using the Saffir-Simpson Hurricane Wind Scale (Table 3.3). The classification is based on the wind speeds and impacts, and it was originally introduced in the US National Hurricane Centre by Herbert Saffir and Bob Simpson in 1971, but then used worldwide. The scale has five points of hurricane intensity. Category 1 has maximum winds of 74-95 mph, and can cause minimal damages, including uproot of trees and some flooding. For Category 2 the maximum winds are between 96 and 110 mph with moderate damages. Category 3 can be described as extreme, having wind speeds reaching 111 to 129 mph winds, causing structural damages to small buildings and serious coastal floods. Category 5 is described as catastrophic with winds greater than 156 mph and evacuations taking place for up to 10 miles inland.

Table 3.3: Saffir-Simpson Hurricane Wind Scale

Category	mph	m/s	Characteristics
1	**74-95**	**33-42**	**Very dangerous winds/some damages**
2	**96-110**	**43-49**	**Extremely dangerous winds/extensive damages**
3	**111-129**	**50-58**	**Devastating damage**
4	**130-156**	**58-70**	**Catastrophic damage**
5	**$\geq$ 156**	**$\geq$ 70**	**Catastrophic damage**

Dorian (Table 3.4) reached Category 5 hurricane that formed on the 24th of August 2019 in the central Atlantic. It was then rapidly intensifying in the following days, until it reached its peak, on the 1st of September with highest wind speed of 185 mph and its lowest estimated pressure of 950 hPa. At that time it hit the Abaco Islands in the Bahamas with its maximum winds. After its landfall it started to weaken while propagating offshore of the US south-eastern coast and by the 6th of September it crossed Cape Hatteras as Category 2. It then hit Nova Scotia as an extra-tropical cyclone on the 7th of September and finally dissipated over Greenland on the 10th of September. Dorian affected many areas, including Puerto Rico, the Bahamas, Florida, Georgia and South Carolina. The cost of the damages caused by Dorian exceeded 5.1 billion US dollars.

Hurricane Teddy (Table 3.4) was a Category 4 hurricane that formed in September 2020. Its highest sustained winds reached 140 mph, and minimum pressure was 945 hPa at its peak. The hurricane started as a tropical depression on the 12th of September 2020, and it then rapidly intensified to a Category 2 hurricane on the 16th of September, with further intensification to Category 4 hurricane on the 17th of September 2020. It later started to weaken and passed by Bermuda as a Category 2 hurricane. It finally dissipated on the 24th of September 2020. Damages by Teddy costed more than 35 million US dollars.

Typhoon Lingling (Table 3.4) reached Category 4. It formed on the 31st of August 2019 and it was originally named Linwayway. After its intensification to a tropical storm on the 2nd of September, the Japanese Meteorological Agency renamed it to Lingling. It was upgraded to a typhoon on the 5th of September. While crossing south of China it evolved as a category 2 typhoon and progress to Category 4 while passing east of Taiwan. The highest sustained winds were estimated to 140 mph and the lowest pressure was 940hPa. Damages in Philippines, China and Korea were about 236 million US dollars.

Typhoon Bavi (Table 3.4) was a Category 3 typhoon, which formed on the 20th of August 2020. Bavi started as an area of low pressure close to the Philippines and soon intensified to a severe tropical storm. On the 24th of August it became a Category 2 typhoon and the next day intensified further to a Category 3. Its highest wind speeds were 115 mph and its lowest pressure was 950 mph. Damages cost 11.7 million US dollars.

Table 3.4: Case Studies Characteristics

Case Study	Maximum Intensity	Maximum Winds	Date
Storm Ciara	-	**97 mph**	**8-9/02/2020**
Hurricane Dorian	Category 5	**185 mph**	**24/08-10/09/2019**
Hurricane Teddy	Category 4	**140 mph**	**12-24-09/2020**
Typhoon Lingling	Category 4	**110 mph**	**31/08-08/09/2019**
Typhoon Bavi	Category 3	**100 mph**	**20-30/08/2020**

3.7 Data

3.7.1 Model Initialisation

The data used to initialise OpenIFS were taken from the operational analysis data produced at ECMWF, and they were provided by the Centre. These data come from the operational analysis method. This method is used in order to examine the current and historical performance of the model. The data are time consistent and they cover the whole globe without gaps.

3.7.2 In-situ observations

For the validation of the results from the two schemes, in-situ data from buoys, obtained from the Global Telecommunication Systems (GTS) and archived by ECMWF in a database maintained by the wave forecasting team (Jean Bidlot personal communication), were used. The Global Telecommunication System (GTS) is an integrated network including both surface-based and satellite-based telecommunications, in order to achieve round the clock and near-real-time collection and distribution of the data, forecasts and alerts, both point-to-point circuits and multi-point circuits interconnecting meteorological telecommunication centres operated by countries. More information for this type of data can be found in the web page of the Word Meteorological Organisation (WMO). Based on the above, GTS is the main system of data and information exchange that supports multi-hazard, multi-purpose early warning systems. Hence, the system includes all meteorological and seismic parametric data, as well as weather, water and climate analyses and forecasts and tsunami information and warnings.

More specifically, moored buoys were used for the extraction of observations of wind speed and significant wave height. Generally, buoys measure vertical acceleration, which are then integrated twice in time to produce the vertical displacement due to waves. A record of about 20 to 30 minutes is then analysed using Fourier analysis to produce the wave spectrum from which the wave integrated parameters such as the significant wave height and wave periods are derived. These buoys are quite often also instrumented with atmospheric sensors, such as anemometer for wind speed and direction estimates.

The database might contain missing data, either due to lack of reporting, or flagged as invalid by the quality control carried by ECMWF. Stations with many missing values were avoided and interpolation was performed using the cubic method in Python in stations with a few missing values. Station data used in the study were chosen based on the hurricane and typhoon trajectories. The stations used, as well as their details, such as the location, the depth and anemometer height are given on Table 3.5. Their location is also shown in Figure 3.6.

Specifically for hurricane Teddy, additional GTS data from drifting buoys (Figure 3.5) were available. Drifting buoys are smaller than the mooring options. Wave observations from drifting buoys have become more wide spread in recent years, due to coordinated efforts and deployments. For instance, a line of those buoys was deployed ahead of the Hurricane Teddy in order to specifically study waves around the hurricane.

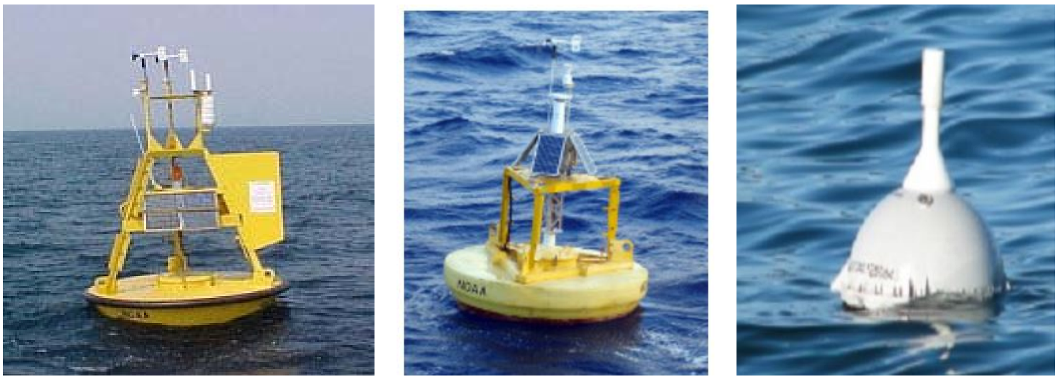

(a) (b) (c)

FIGURE 3.5: Type of Buoys: (a) 3-meter Discus Buoy (b) 3-meter Foam Buoy (c) Drifting Buoy. Photos were found in NOAA and ECMWF web-pages.

3.7.3 International Best - Track Archive for Climate Stewardship (IBTrACS)

In order to examine the cyclone trajectories, both for selecting the buoys, and for reviewing the model's success, the International Best-Track Archive for Climate Stewardship (IBTrACS) data were used. These data provide global tropical cyclone best-track data and aim to improve the understanding of the distribution, frequency, and intensity of tropical cyclones worldwide. IBTrACS is the official archive by the World Meteorological Organization Tropical Cyclone Program.The data are accessible in different formats, such as ASCII and NetCDF.

For typhoon Lingling, in addition to the stations from the GTS provided by the Korea Meteorological Administration (KMA), data from one more station were provided by the buoy observations supported by Yellow Sea Ocean/East China Sea Observation and Research Station of OMORN.

3.7.4 Altimeter Data

In addition to ground (buoy) data, 10m wind speed and significant wave height of altimeter data from polar orbiting satellites were also used for the validation of the two source input schemes. Altimeter data can provide both significant

TABLE 3.5: Locations and details of wave buoys.

ID	Location	Water Depth (m)	Anemometer Height (m)
41001	34.75 N 72.19 W	4486	3.8
41004	32.50 N 79.09 W	35	4.1
41013	33.44 N 77.76 W	33	4.1
41025	35.01 N 75.45 W	48.8	3.8
41047	27.46 N 71.46 W	5340	4.1
41049	27.49 N 62.93 W	5459	4.1
22103	34.00 N 127.50 E	79	N.G.
22104	33.8 N 126.10 E	98.9	N.G
22187	33.13 N 127.02 E	106.6	N.G.
22191	36.13 N 124.06 E	N.G.	N.G.
22192	34.00 N 123.26 E	N.G.	N.G
*S*6	30.715 N 123.13 E	N.G	10

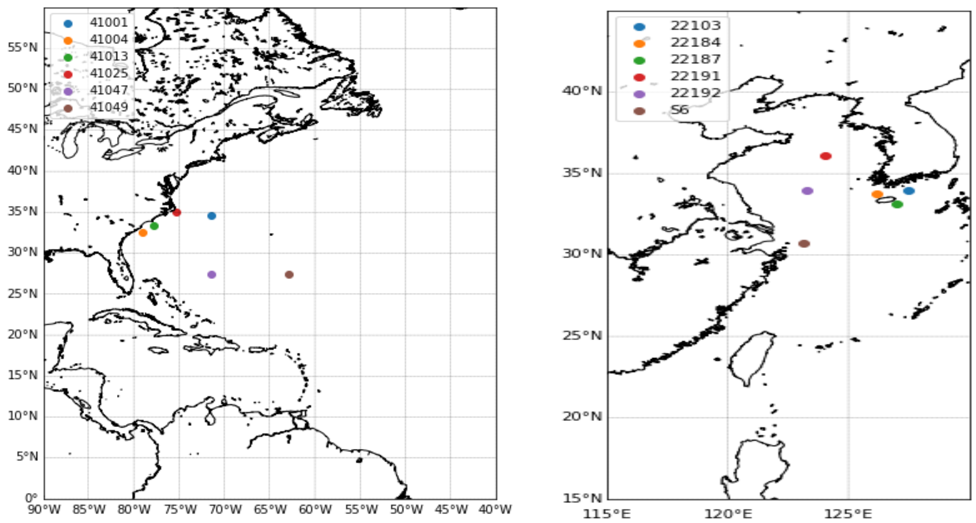

(a) (b)

FIGURE 3.6: Locations of moored buoys used for the validation of the model. a) Wave buoys in the Atlantic for hurricanes Dorian (41001,41004, 41013, 41025) and Teddy (41047,41049) wind and wave observations b) Wave buoys in Yellow Sea for typhoons Lingling (22184, S6) Bavi (22103, 22187, 22191, 22192).

wave height and wind speed measurements, as well as other oceanographic parameters. The process of measuring the significant wave height using the altimeter is quite simple and it is based on the signal produced from the satellite. A spherical radar signal is sent by the satellite towards to nadir. This signal is then reflected by the surface of the sea and it is sent back to the satellite. The time that the signal needs to go and come back can give the distance between the satellite and the sea surface. It is easy to understand that the sea state affects the time that the signal requires to fully return to the transmitter, with wave crests reflecting the signal before the troughs of the waves. Hence, the slope of the front in the radar altimeter wave form can resolve the significant wave height. When the return signals are more spread in time, higher waves are indicated. That means that longer delays between the first return and the full return of the signal, give long shadows in the waveform, which suggest higher sea states. The waveform is schematically shown in Figure 3.7

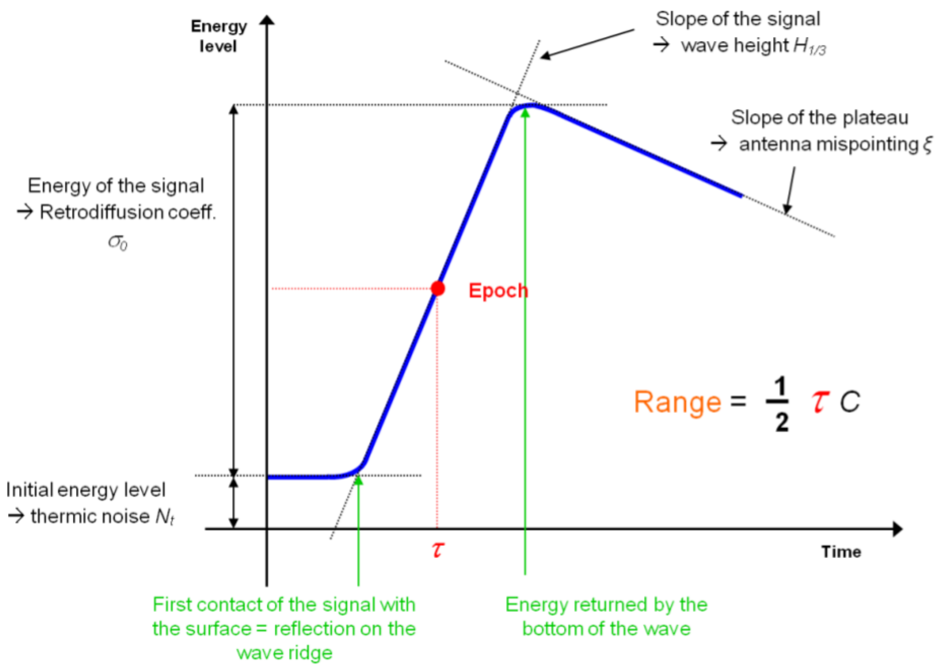

FIGURE 3.7: Altimeter Waveform. Figure taken from Copernicus Marine Quality Information Document (https://resources.marine.copernicus.eu/documents/QUID/CMEMS-MOB-QUID-015-008.pdf)

Wind speed measurements are connected to the small gravity-capillary waves and hence are found to be associated with the back scatter coefficient, σ_0 shown in Figure 3.7 as these short waves (ripples) tend to scatter away the signal that would otherwise return to the satellite antenna. Different approaches have been used for calculating the wind speed based on the back scatter coefficient. For the 10 m surface wind speed the wind speed model function is usually used.

The altimeter data used in this thesis are Near-Real-Time (NRT) level 2 and 3 along track products. These measurements came from satellites Jason 3 (J3), Sentinel 3a (S3a), Sentinel 3b (S3b) and CryoSat-2 (C2). The missions are running over different periods. Jason 3 runs from 13/12/2016 to present, Sentinel 3a from 17/02/2016 to present, Sentinel 3b from 06/06/2018 to present and CryoSat-2 from 01/01/2011 to present.

Two different providers were used in this thesis. Data from the Copernicus Marine Service (https://marine.copernicus.eu/) are (currently) available for the years 2020 and 2021. As mentioned before in this thesis the case studies used are from 2019 and 2020. For this reason data for 2019 extended using NOAA CoastWatch/OceanWatch (https://coastwatch.noaa.gov/cw/index.html). Both these providers gave the significant wave height and the 10 meters wind speeds. The data are freely distributed thought the providers' File Transfer Protocol (ftp) pages.

Satellite tracks cover the whole globe, with roughly 7km spacial resolution (corresponding to 1 observation every second). The temporal repeat depends on the mission. For Jason 3 that is 10 days (or more precisely 9.9156), for Sentinel 3a and Sentinel 3b it is 7 days, and for CryoSat it is 369 days with 29 days sub-cycle. Main characteristics for the satellites are summarised in Table 3.6

Table 3.6: Details of the altimeter sources.

Mission	Partnership	Period of availability	Cycle duration
Jason-3	EUMETSAT/NOAA	13/12/2016 to present	10
Sentinel-3a	ESA/EUMETSAT	17/02/2016 to present	27
Sentinel-3b	ESA/EUMETSAT	06/06/2018 to present	27
CryoSat-2	ESA	01/01/2011 to present.	369 (29 sub-cycle)

The data were in NetCDF format, with all having the form of Latitude, Longitude, Time, Variable 1 (e.g. significant wave height), Variable 2 (e.g. wind speed) etc. It is important to mention here that one needs to be careful with the time units. Copernicus Marine give the time in seconds from 01/01/2000, while for NOAA time unit is in seconds from 01/01/1985. For Copernicus Marine, the measurements are given in files that include 3 hours timesteps, while NOAA provide one file for each day. The form of the data for each provider are shown in Tables 3.7 and 3.8. All data have passed the quality control and only valid values were used, using different criteria such as parameter thresholds and quality flags. Particularly, for the significant wave height all satellites have a 30m maximum threshold. Additionally 30 m/s is used as a maximum threshold for wind speeds.

TABLE 3.7: File formats for merged altimeter data from Copernicus Marine

Name	Standard Name	Long Name	Units
time	time	time (sec. since 2000-01-01)	seconds since 2000-01-01 00:00:00.0
latitude	latitude	latitude	degrees North (-90 to 90)
longitude	longitude	longitude	degrees East (0 to 360)
VAVH	sea_surface_wave_significant_height	significant wave height on main altimeter frequency band	m
VAVH_UNFILTERED	sea_surface_wave_significant_height	significant wave height on main altimeter frequency band	m
WIND_SPEED	wind_speed	Equivalent 10-m wind speed derived from altimeter measurements	m/s

As the measurements from the satellites are along track, i.e. they are not stable in space, it is important here to explain the procedure of analysing this type of data.

The whole process was done in python using mainly the toolbox of python pandas. The first step was the extraction of the data from the satellites. Dataframes with the time, latitude, longitude, significant wave height and wind speed for all given (per second) time steps were firstly created. Then, using the columns of latitude and longitude, the specific domains of the case studies was extracted in a new dataframe. Again all the per second times were kept in this step. Based on the new dataframe's latitude and longitude columns, the significant wave height and wind speed values for the two schemes were extracted from the model results, and two other panda dataframes, for each scheme, were created. Then the three dataframes (one from satellites and the two of the schemes) were combined in one. Then, in order to be comparable (having the same times, and so on shape) as the model outputs are hourly, the first time from the satellite was kept, and for having the best possible measurement of the per second ones, the median values were used. This method is good enough, as in any way we already accept the assumption that the whole interval of the model's timestep, the significant wave height and wind speed have one value. At the same time in order to have the best possible comparisons spatially, the each model grid point in the domain is compared to the mean of each seven points of the satellites, as due to model and satellites resolution every model grid box holds about seven satellite points.

TABLE 3.8: File Formats for merged altimeter data from NOAA

Name	Standard Name	Long Name	Units
time	time	time	seconds since 1985-01-01 00:00:00 UTC
lat	latitude	latitude	degrees North (-90 to 90)
lon	longitude	longitude	degrees East (-180 to 180)
swh	sea_surface_wave_significant_height	Ku-band significant wave height	m
wind_speed	wind_speed	altimeter wind speed	m/s

Chapter 4

Testing of the WBLM

4.1 Introduction

Using storm Ciara as case study, this chapter presents results of the i) model calibration; ii) sensitivity analysis of the WBLM scheme; and iii) the sensitivity to coupling (i.e. difference between coupled and un-coupled simulations). In this Chapter the first test run, using initial conditions for Storm Ciara, is presented. That was the main test run used during the implementation, until the results of drag and Charnock coefficient were of the expected magnitude. In addition to that, the examination of the sensitivity of the WBLM scheme to the first guess of drag coefficient is shown here. Finally, the importance of the coupling is shown using plots of the coupling is presented.

4.2 Calibration of the WBLM scheme

As shown in Figure 4.1, using the WBLM significantly reduces the Charnock coefficient. For Janssen's scheme (shown with green to yellow colorbar), there are values that reach even 0.1 for winds of 20 m/s or above. For 10m wind speeds of the same magnitude, WBLM scheme gives lower values, with the majority of the entries between between 0.025 to 0.050. However, WBLM yields some outliers that reach even values of 0.2.

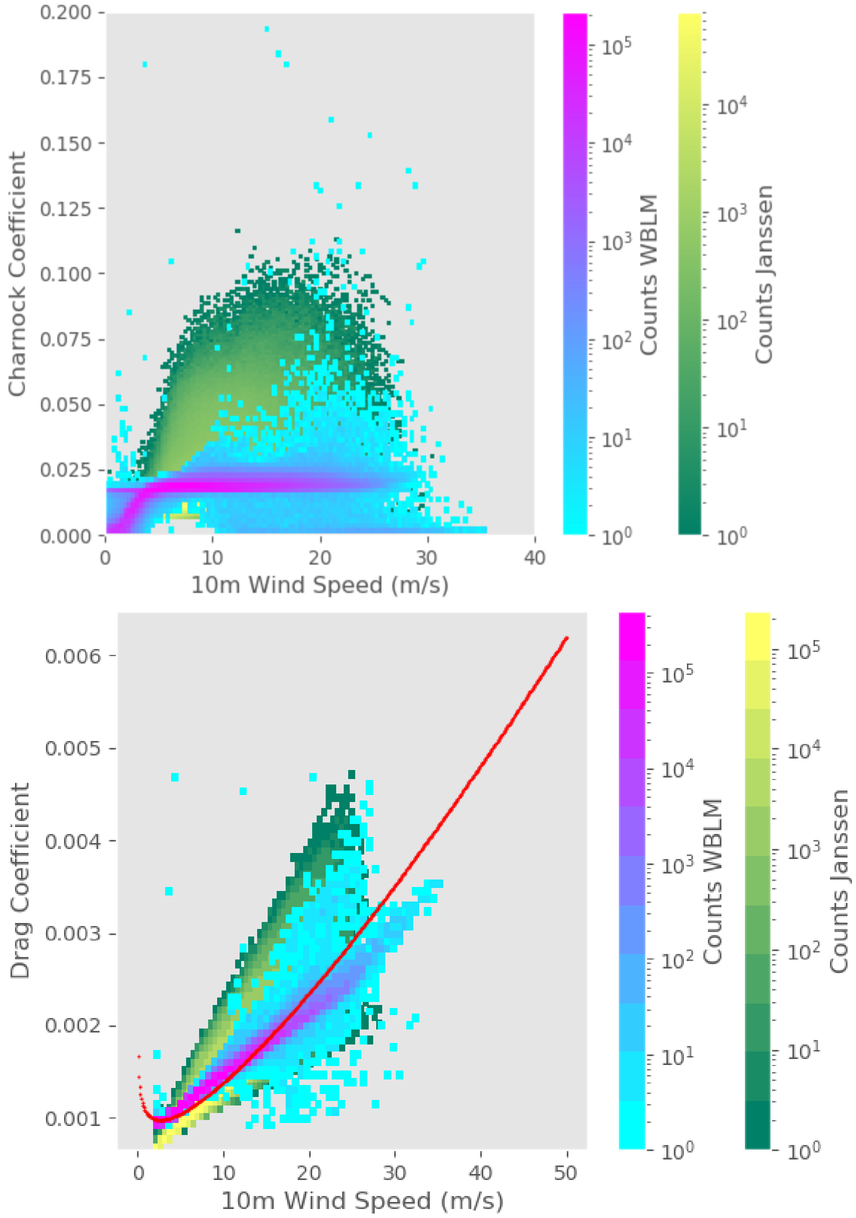

FIGURE 4.1: Correlation plots of Charnock (top) and Drag (bottom) coefficients for the forecasting period during storm Ciara (6-11 of February 2020) for the global domain. The red solid line shows the Drag coefficient as calculated by Edson et al. (2013)

Correspondingly, the drag coefficient calculated from the WBLM is lower than the one given from Janssen's source input function. In addition, the colourbar, which shows the number of entries, reveals that the majority of the values ($> 10^4$), for WBLM, is close to the best fit, as well as the drag coefficient calculated from Edson et al. (2013) (shown with red solid line). At the same time, it was found that the scatter around the mean is reduced when WBLM is used, while Janssen's scheme is significantly more scattered.

4.3 Sensitivity Test on the Drag Coefficient First Guess

As mentioned before, the WBLM source input function works by guessing a first drag coefficient, which is then updated based on the calculation of the stress and the wind profile. Hence, it was important, prior to conducting the main analysis of the case studies of the extreme events (tropical cyclones), to check that the new source input function scheme is robust, meaning that is not sensitive to this first guess of C_d.

Figure 4.2 shows the simulated drag coefficient from WBLM, using Du et al. (2019) first guess (orange) and against the simulated C_d using WBLM with Edson et al. (2013) first guess of C_d (blue). Two main findings are revealed from the plot. Firstly and most importantly, the scheme is stable when the different first guesses of drag coefficient is used. That means that the scheme works well with any starting point of C_d, and i for any case. Secondly, the first guess of C_d used by Du et al. (2019) increased the very low values of the drag coefficient for winds around 25m/s, and a slight reduction in scatter can be seen.

4.4 The importance of coupled simulations

In this section, plots of uncoupled against coupled simulations are presented, in order to access the sensitivity to coupling. Using the WBLM option, Figure 4.3 presents the differences between coupled, where the wave part of the model communicates with the atmospheric part through the stress, and uncoupled simulations, where the feedback from the waves to the atmosphere is not taken into consideration. Simulations shown are for 10m wind speed and

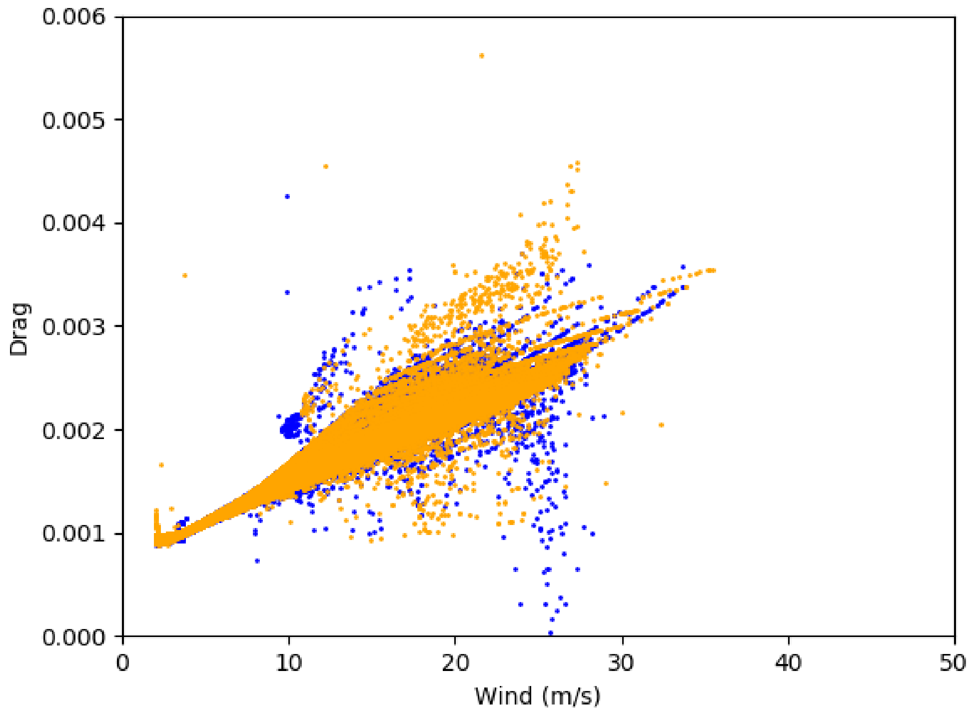

FIGURE 4.2: Comparison of WBLM simulated drag using first guess of Du et al. (2019) (orange) and Edson et al. (2013) (blue)

significant wave height.As shown from the wind speed plot Figure 4.3a in most of the domain the winds are reduced, due to the feedback increased roughness (momentum loss due to wave generation). However, in areas where the winds have their highest intensity (i.e. north and south parts of the cyclone), winds have an increase of more than 3m/s when coupling is turned on. That can be linked to the decreased drag, which then allows the winds to reinforce, but also one cannot discard the possibility of a small shift in the cyclone motion since the whole atmosphere evolution is adapting to different settings. In comparison, significant wave height Figure 4.3b shows a general decrease when the coupling is turned on, expect for the areas of steep waves associated to the cyclone (e.g. south part of the cyclone).

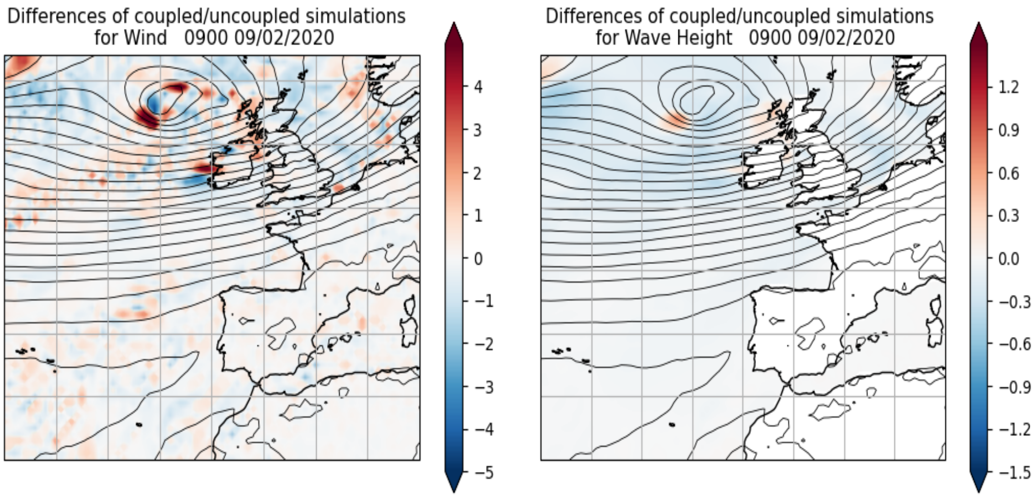

(a) (b)

FIGURE 4.3: Distribution of (a) wind speed differences and (b) significant wave height between coupled and uncoupled simulation for storm Ciara. Snapshot: 09:00 UTC 09/02/2020. Isobars shown in both plots come from the coupled simulation.

4.5 Summary

In this chapter important tests using storm Ciara as case study of the scheme's sensitivity, based on the initial guess of C_d were performed and presented. These tests showed that the new approach of the source input function is reliable in terms of the Charnock and Drag Coefficient magnitude, as both are in agreement with previous studies. That allowed us to continue the analysis for case studies with winds above 30m/s (hurricane and typhoon conditions), in order to analyse how the scheme can affect the predictions during extreme conditions.

Chapter 5

Impact of the WBLM Scheme on Simulations During Tropical Cyclones

5.1 Introduction

The focus of this chapter is on experiments during tropical cyclones. These runs use the highest possible resolution and initial conditions of extreme events. For each case study (each initial conditions) the main analysis is based on comparing the correlation of the drag and Charnock coefficients with 10 m wind speeds from the two schemes. The plots include the entire forecasting period of the runs and whole (global) domain. That means that not only the area, time and conditions of the extreme events were under consideration, but all different areas and atmosphere/sea state conditions were taken into account. Considering the whole area and period allows better representation of different conditions, which permits better comparison of the two schemes.

Furthermore, global spatial wind distribution plots for the different cyclone cases are also discussed. These plots can instantly show if and how the new approach of the WBLM scheme affects the model predictions. Again, the total forecasting periods produced and the global domain are presented on the plots.

The gamma method is used for fitting the distribution of the winds. This method was found to better work with the model outputs. Supporting wind roses are also used in order to examine the dominant directions and intensities of the wind speeds as calculated from the two source input functions.

Lastly, for each specific tropical cyclone, differences maps of surface winds and significant wave height were produced at the location and the time of the storm passing. The specific time steps were chosen in order to capture the differences of the two schemes during or close to the peak of each cyclone.

It is important to highlight here that the initial conditions for hurricane Dorian and typhoon Lingling overlap, due to the fact that the two events were close in time. However, it was decided that both forecasting periods will be reviewed, as different conditions may reveal different findings.

5.2 The impact of the WBLM scheme on global forecasting during periods of Tropical Cyclones

5.2.1 Charnock and Drag Coefficient Outcomes

Correlation plots for the Charnock coefficient for all the different periods and for both schemes are shown in Figures 5.1 (Dorian and Teddy) and 5.2 (Lingling and Bavi). Each plot includes both Janssen and WBLM source inputs. For Janssen the correlation is shown with the green to yellow colorbar, which gives the number of entries of each point. That means that higher (more yellow) areas of the colorbar have more points in the domain that give a specific value of the Charnock coefficient for the corresponding 10m wind speed. For WBLM the corresponding colors are blue to pink. Maximum counts for both schemes are in the order of magnitude of 10^6. Maximum Charnock coefficient values are reaching 0.125, with outliers extending to 0.2.

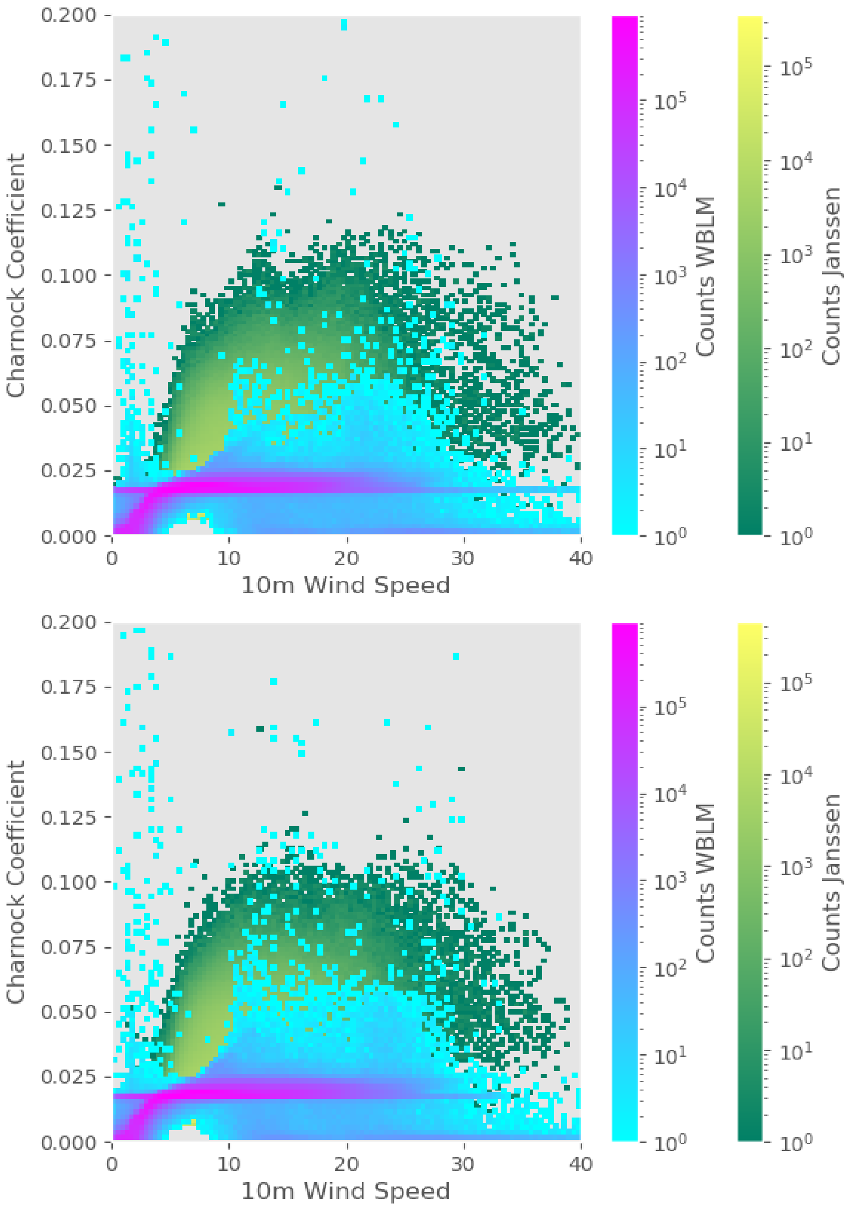

Figure 5.1: Correlation of the Charnock Coefficient with 10m Wind Speed for the periods 02 to 09 September 2019 (Dorian initial conditions) (top) and 17 to 24 September 2020 (Teddy initial conditions) (bottom). WBLM is shown with cool (blue to pink) colorbar and Janssen (1991) with summer (green to yellow) colorbar. The colorbars show the counts of entries for each scheme.

It is important to point out here that the default value of Charnock parameter (0.018) is visible in the plots. This is due to the facts that i) the Charnock parameter is an output of the atmospheric model and ii) the wave model does not cover all points that are considered to be sea points by the atmospheric model. For those points, the IFS will instead use the default value of 0.018. That is an issue that will be corrected in the latest versions of IFS, however it was still an existing issue in the version used here (CY40R1V2).

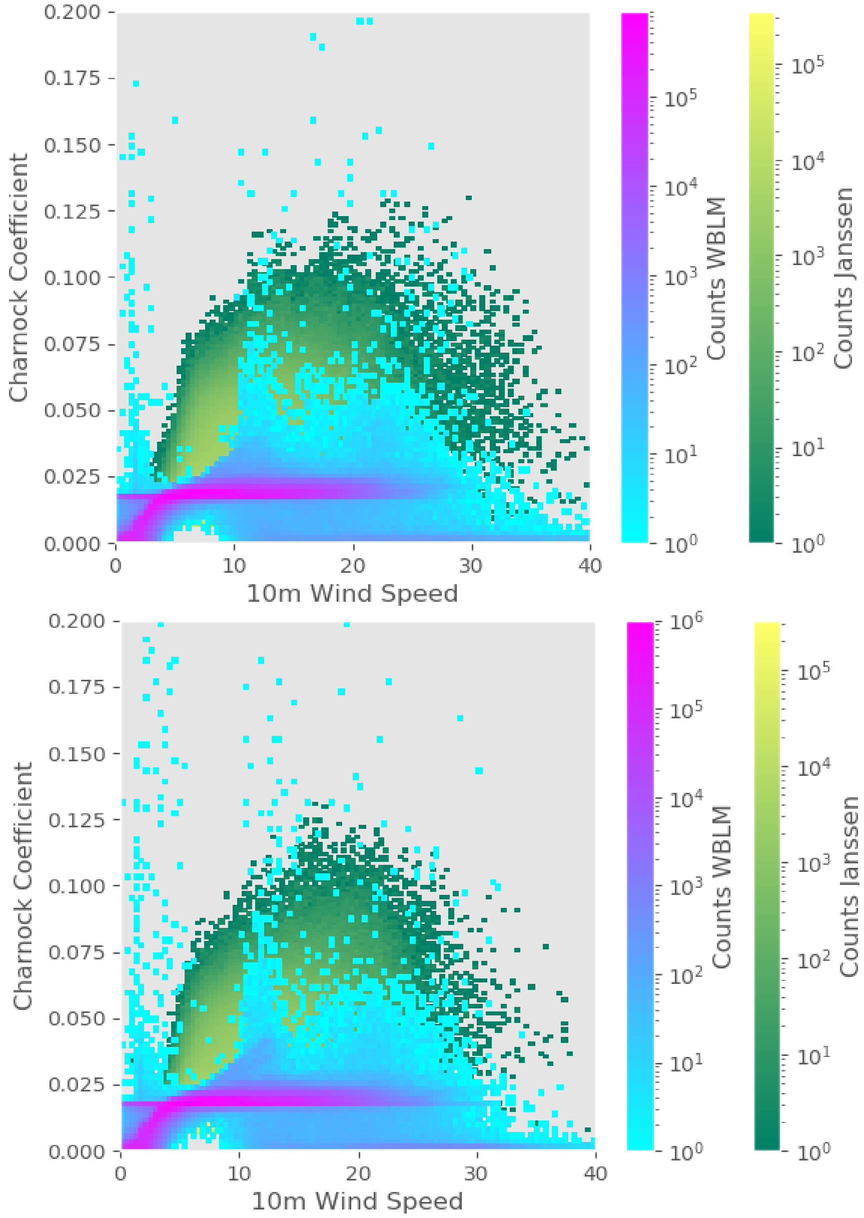

FIGURE 5.2: Correlation of Charnock Coefficient with 10m Wind Speed for the period 04 to 11 of September 2019 (Lingling initial conditions) (top)and 24 to 31 of August 2020 (Bavi initial conditions) (bottom). WBLM is shown with cool (blue to pink) colorbar and Janssen (1991) with summer (green to yellow) colorbar. The colorbars show the counts of entries for each scheme.

Overall both schemes keep the expected shape of the Charnock coefficient versus U10: where initially there is a constant increase of its values with wind speed, whereas later (around 25 to 30 m/s) there is a steady decrease of the mean value. For both source inputs most entries are in the centre of the graph, i.e. the mean area of the correlation.

The Charnock coefficient from the WBLM source input function is generally closer to the constant value of 0.0185 (or mean value of the plot) compared to Janssen's scheme, while the default source input shows a lot of scattering around the mean. In low wind speeds (lower than 5 m/s) the two schemes are in good agreement, however WBLM gives some extreme estimations, that even reach 0.175 for wind speeds around 1 m/s. These outliers can be explained based on the fact that the scheme is highly depends on the condition of convergence used, in order to find the "best possible" value of C_d. During the implementation part, it has been seen that in case that the scheme does not converge, some criteria are used in order to find the best possible solution, based on a number of iterations. These criteria, hold some randomness in choosing the best drag coefficient, which can then give unrealistic values of Charnock. The different simulations showed that there are many times that the convergence was not reached, and the aforementioned criteria was needed. For this reason some outliers are found. In moderate winds there is significant decrease of Charnock calculated from the WBLM. In addition, the same source input function continues to compute several high values that extent up to 0.2 for wind speeds around 20 m/s. In moderate winds, the Charnock coefficient as per Janssen's scheme shows its higher scatter around the mean values, having some very high estimations, with the highest entries around 0.12. In general, it is notable that for wind speeds from 15 to 30 m/s for Janssen calculations there are many entries constantly above 0.075. For the extreme wind speeds, which is the main area of the interest of this thesis, Charnock values from WBLM are much lower than the ones from Janssen's scheme. Usually, they are about 0.050, while Janssen's scheme for the

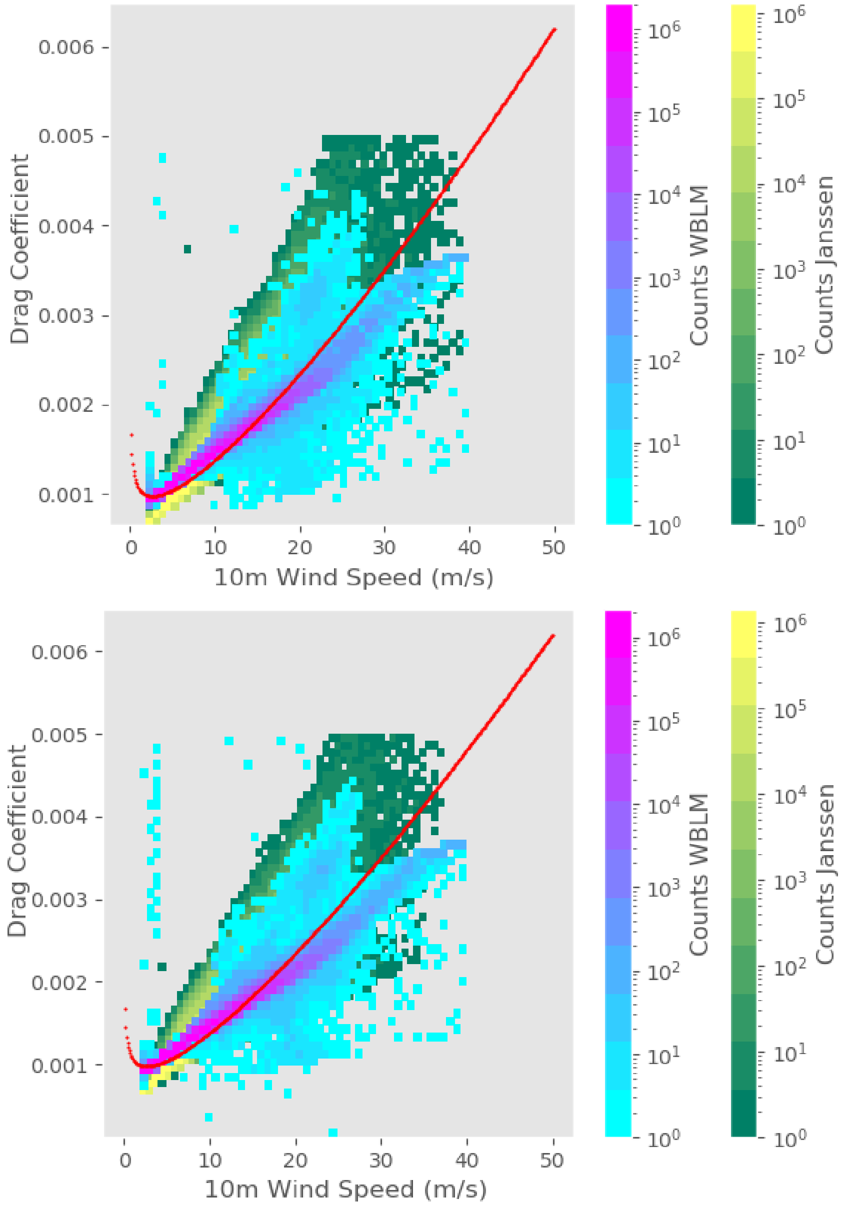

FIGURE 5.3: Correlation of Drag Coefficient with 10m Wind Speed for the periods 02 Sept to 09 September 2019 (Dorian initial conditions) (top) and 17 to 24 of September 2020 (Teddy initial conditions) (bottom). WBLM is shown with cool (blue to pink) colorbar and Janssen (1991) with summer (green to yellow) colorbar. The colorbars show the counts of entries for each scheme and the red line shows the drag coefficient of Edson et al. (2013) for reference.

same area has many entries that are double the magnitude of the WBLM.

In general discarding some high values in low and moderate winds, the new scheme significantly decreases the Charnock coefficient when used in all different simulations.

Corresponding drag coefficient values from the two schemes are shown in Figures 5.3 and 5.4. The colorbars show the number of entries of each correlation. Green to yellow colors represent Janssen's scheme and blue to pink colors show the WBLM results. In these plots the drag coefficient as calculated from Edson et al. (2013) is also shown (solid red line), in order to have a reference point for the two source input functions. Again, similarly to Charnock, the number of entries are of 10^6, with maximum values of drag coefficient reaching 0.005 for Janssen scheme.

Similarly to the Charnock coefficient results, the drag coefficient values are also accumulated closer to Edson et al. (2013) estimation, therefore to the mean values. Even in low wind speeds, scatter from Janssen's source input is greater than the WBLM. That continues until moderate and high winds (15-30 m/s), where the calculated drag from the WBLM also develops some scatter. For WBLM, scatter appears mainly in the lower part of the mean values (Figure 5.3 both panels). At the same point comparing the two panels in Figure 5.3 the mean line of WBLM drag decreases, and it becomes lower than the values of Edson et al. (2013) and Janssen's scheme. However, the scatter from Janssen's parameterisation is again greater than the WBLM. In the critical part of the extreme wind speeds, there is a significant decrease of Janssen's (Figure 5.3 both panels green colorbar) overestimated drag when the model runs using the WBLM source input. In this area of the plot Janssen's scheme holds a lot of scatter, which even reaches 0.005 in some cases. During the same events WBLM values stay close to the predicted values from Edson et al. (2013), where values are even lower than 0.004. It is also interesting that for very low winds, WBLM follows the trend of higher drag coefficient, as shown in Edson et al. (2013), while Janssen's keeps the lowest predicted value. That is because the viscous contribution is taken into consideration for z_0 in the WBLM, while in the model version used here this is not the case for ECWAM with Janssen's scheme. In explanation, even though C_d using Janssen's scheme includes the viscous

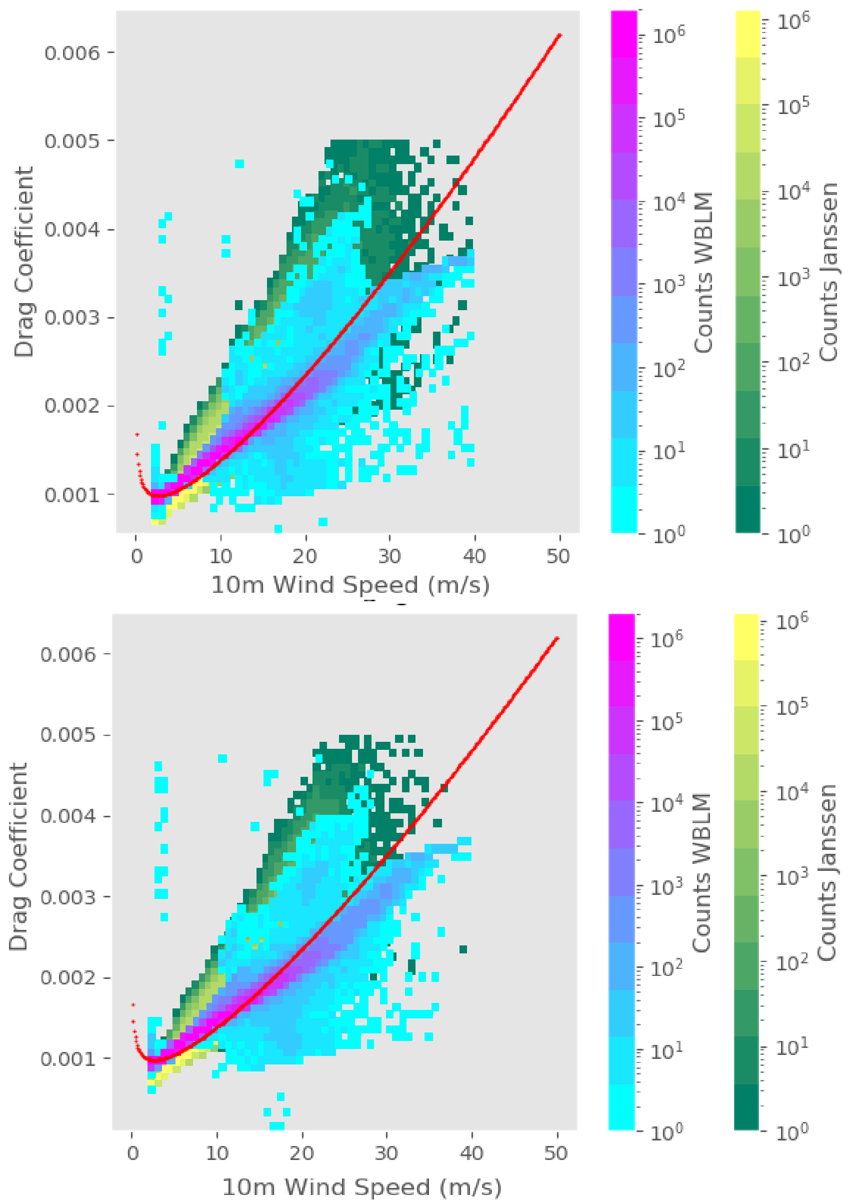

FIGURE 5.4: Correlation of Drag Coefficient with 10m Wind Speed for the periods 04 to 11 of September 2019 (Lingling initial conditions) (top) and 24 to 31 of August 2020 (Bavi initial conditions) (bottom). WBLM is shown with cool (blue to pink) colorbar and Janssen (1991) with summer (green to yellow) colorbar. The colorbars show the counts of entries for each scheme.

contribution for the atmosphere, and is easy to be added in ECWAM, it was neglected because it had no impact on the waves. Some C_d outliers estimated using WBLM are also found here, similarly to Charnock high predicted values for low winds.

5.2.2 Wind Distribution

The wind distribution is shown in Figure 5.5. Blue distribution is the one given from Janssen's source input function, while the corresponding distribution from WBLM is colored red.The distribution is shown with both bar plots, as well as with normal distribution using gamma method. This estimation was chosen as it was found to best represent the wind distribution. Density from the bar plots reaches frequencies of about 0.1 while the highest values normal distribution are just bellow 0.12. In general, from wind distribution plots it is found that wind density is initially increases with wind speed and reaches its first peak at about 2-3 m/s. It then decreases for winds between 4 to 8 m/s model conditions and then increases again until winds of 10 m/s. After this the density decreases constantly and it gets close to zero as the wind speeds reach extreme less frequent/tale of distribution values.

For all initial conditions comparing WBLM with the Janssen scheme, wind speeds below 4 m/s give very similar density for both source input functions. For the peak densities (winds of 4-10 m/s) there is a general increase when the WBLM input function is used. This is more obvious for the initial conditions of hurricane Dorian and typhoon Bavi, where the difference reaches about 0.002 in the density scale. However, for the same events there is a constant or almost constant probability of these wind speeds of 4-10 m/s, while for the other two cases the density increases with wind speeds. At higher winds (above 10 m/s) density decreases when the WBLM is used.

Figures 5.6 and 5.7 show the wind roses for global wind speeds for all initial conditions and for both Janssen's and WBLM schemes. Figure 5.6 includes the initial conditions of 2019 (first row 02-09 September 2019 and second row 04-11 September 2019). The first column (plots (a) and (c)) has the wind roses as produced with Janssen scheme and the second column (plots (b) and (d)) shows the wind roses as produced by the WBLM. Similarly, Figure 5.7 presents the

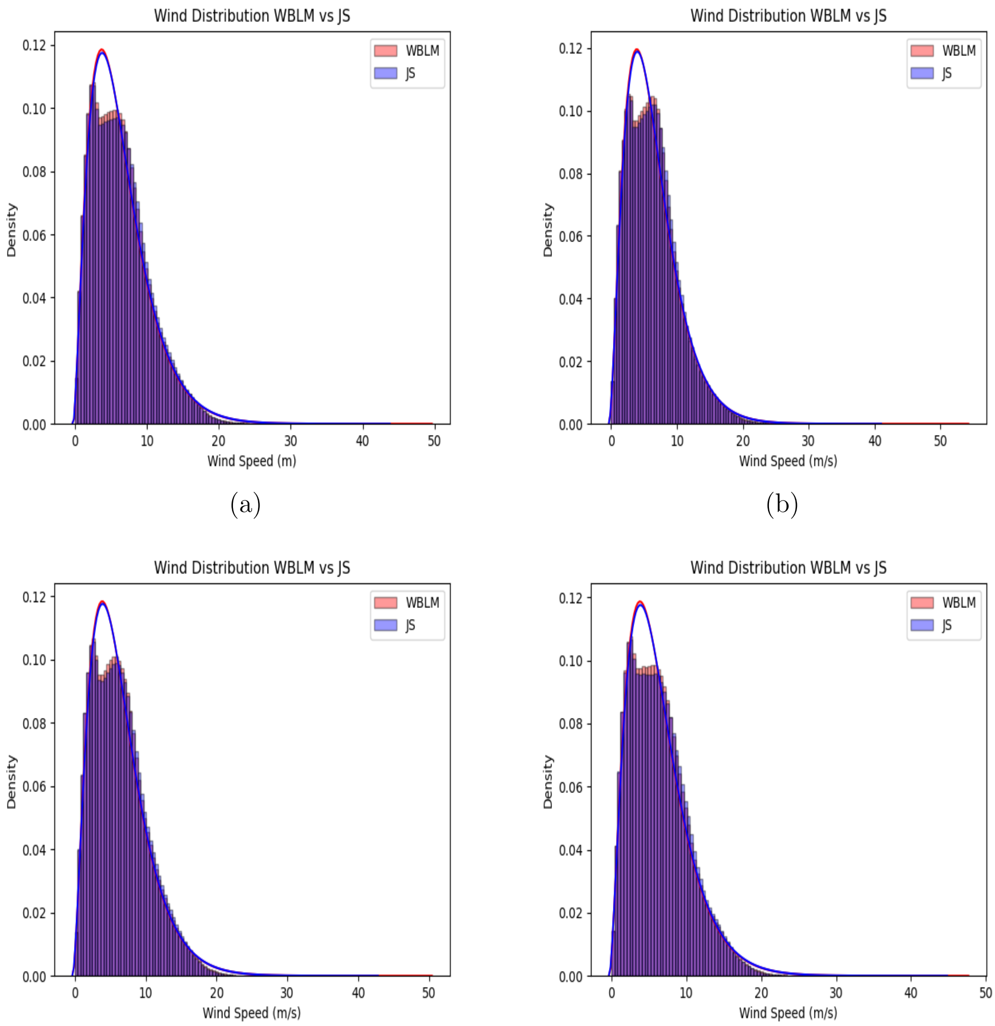

(a) (b) (c) (d)

FIGURE 5.5: Spatial wind distribution for the periods a) 02 Sept to 09 September 2019 (Dorian initial conditions) b) 17 to 24 of September 2020 (Teddy initial conditions) c) 04 to 11 of September 2019 (Lingling initial conditions) and d) 24 to 31 of August 2020 (Bavi initial conditions). WBLM scheme is shown with red and Janssen scheme is shown with blue.

initial conditions of the year 2020 (first row 24-31 August 2020 and second row 19-26 September 2020). In both Figures 5.6 and 5.7 subplots (a) and (c) present the wind roses of Janssen's scheme while plots (b) and (d) show the wind roses from WBLM. The wind speeds are divided in five classes of intensity. The wind speeds between 1 and 4 m/s are shown with blue, the light blue class are winds between 4 to 8 m/s, the green class are the wind of 8 to 12 m/s, the fourth class is colored orange and it includes the wind speeds between 12 and 18 m/s, and lastly the fifth class indicated with dark red is for wind speeds above 18 m/s. Wind roses divide the directions in 16 bins.

For the events of September 2019 (Figure 5.6) it is shown that dominant winds are from the E and W, with winds from E-SE to be more frequent. However, when extreme winds occur (>18m/s) the dominant direction is the W-SW. Between the two schemes, even though the overall general description is the same for both, when OpenIFS runs with WBLM turned on, moderate winds (4-8m/s) increase, while higher winds between 8-12 and 12-18 m/s decrease. The extreme winds (>18 m/s) in some cases show an increase (e.g. NW winds in plot 5.7 panel (d)), while in other cases they decrease (e.g. W-SW in plot 5.6 panel (d)).

For the 2020 events the dominant direction between the two dates of initial conditions differs more. It is noted that the dates do not overlap (as in Figure 5.6) since they occurred during different months (August and September). For August, dominant winds are the ones from E-SE and W-SW directions. Wind speeds above 18 m/s, as was the case of hurricane Teddy and typhoon Bavi, follow a W-NW direction. Again, between the two schemes there is an increase of the winds of 4-8m/s, whereas for wind speeds between 8-12 m/s and 12-18 m/s there is some decrease, but less than in the 2019 cases. Extreme winds (above 18 m/s) have either the same frequency or they slightly increase for August wind roses (e.g N-NW and W directions) and they increase in September wind roses (e.g. W-NW and NW-N directions).

The above results show that WBLM impacts mainly on the intensity of the winds, and not fundamentally on the direction of the winds. Additionally, they indicate that in cases WBLM increase the underestimated winds calculated from Janssen.

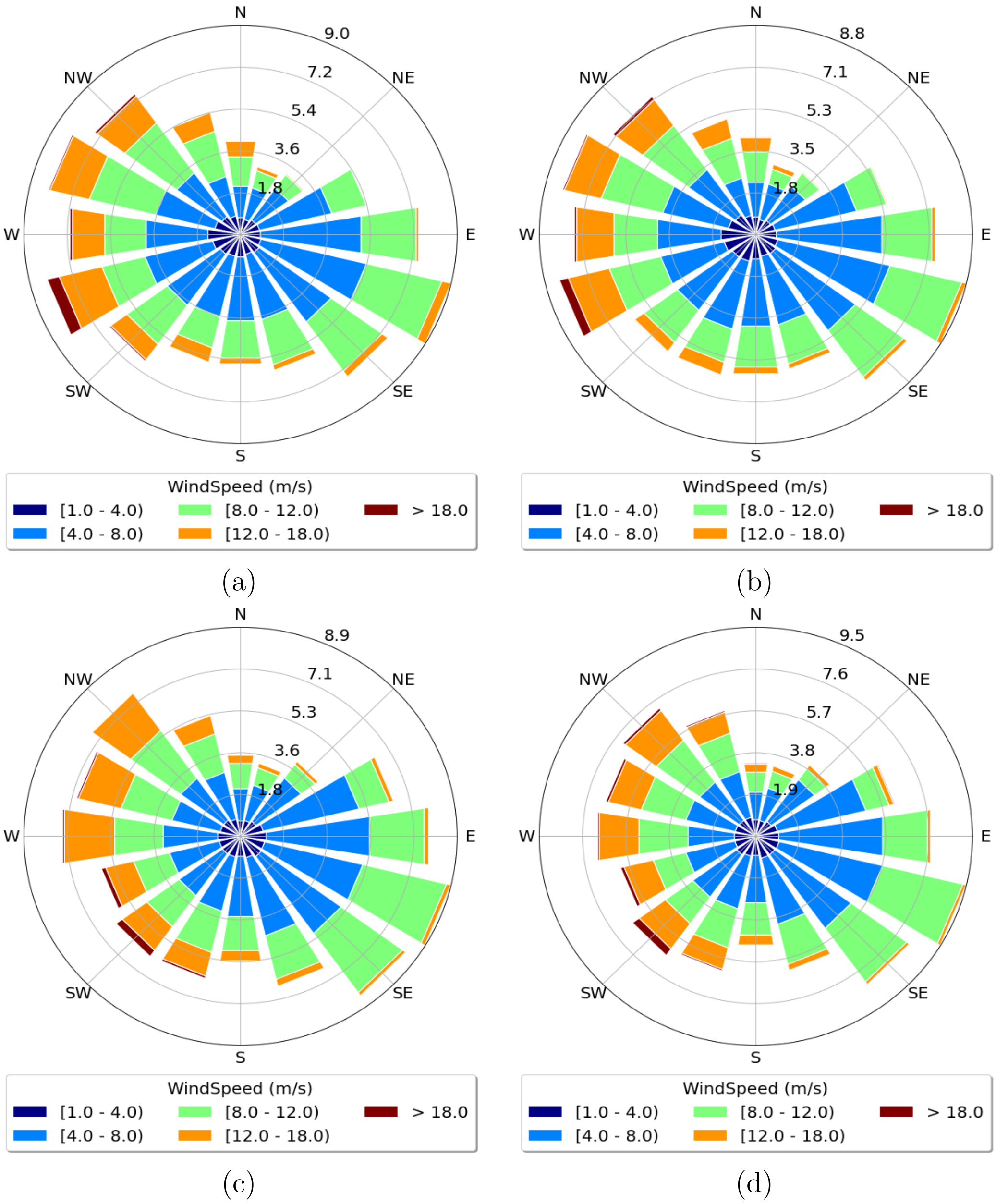

FIGURE 5.6: Wind roses for the period 02 Sept to 09 September 2019 (first row) and 04 to 11 September 2019 (second row). a) and c) winds from Janssen scheme, b) and d) wind from WBLM.

5.3 The Impact of the WBLM scheme on Tropical Cyclone Wind Speeds and Significant Wave Height

In this section the focus is on the area of each tropical cyclone in order to analyse the impact of the WBLM on extreme wind speeds (U10) and significant

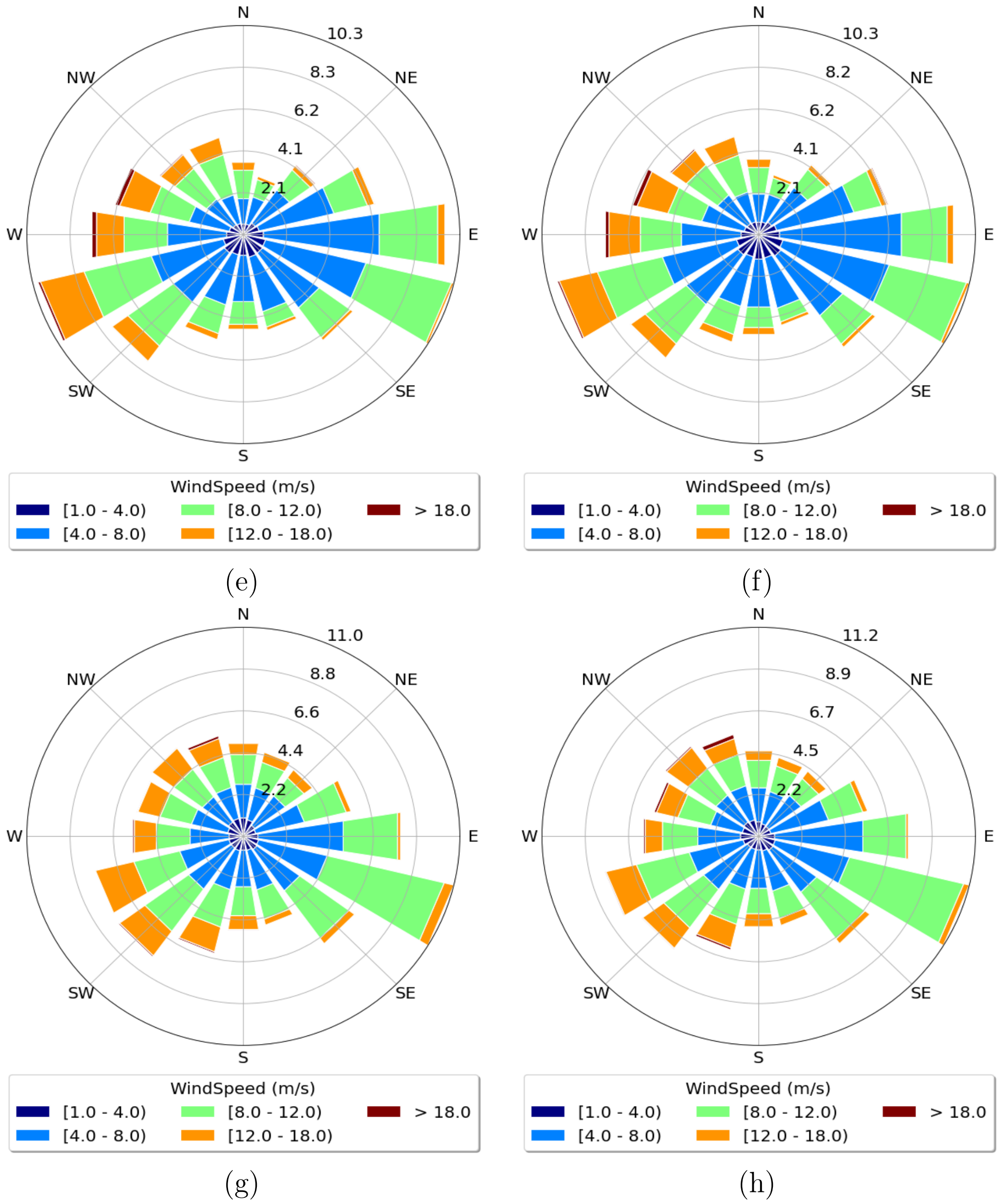

FIGURE 5.7: Wind roses for the period 24 to 31 of August 2020 (first row) and 19 to 26 of September 2020 (second row), a) winds from Janssen scheme, b) winds from WBLM.

wave heights (SWH). In order to examine the effect of the new approach, maps with the difference of 10 m wind speed and significant wave height, between the WBLM results ($U10_{WBLM}$ and SWH_{WBLM}, respectively) and Janssen's scheme ($U10_{Js}$ and SWH_{Js}, respectively) are presented. Positive values (shown with red on the maps) indicate an increase of the wind or the waves when the WBLM is used, while negative values (shown with blue) indicate a decrease of wind or

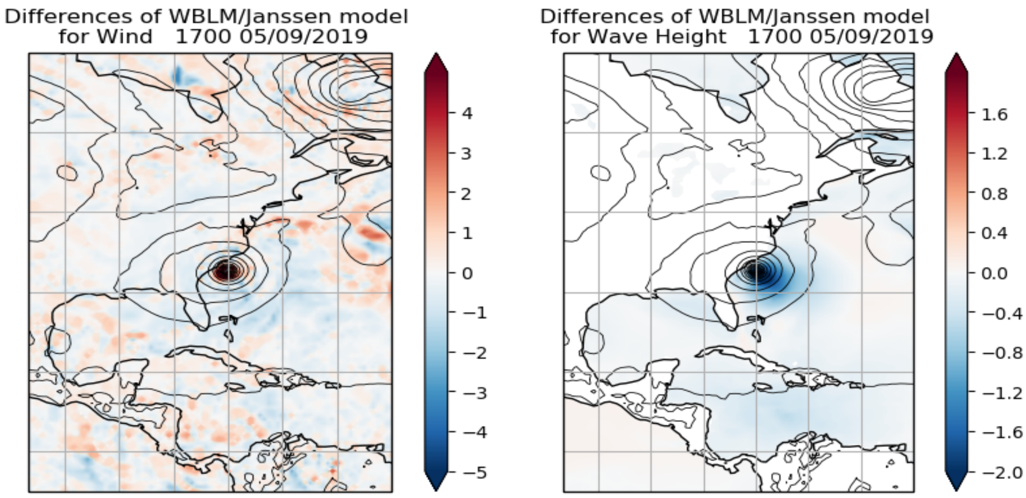

(a) (b)

FIGURE 5.8: Horizontal distribution of (a) wind speed differences and (b) significant wave height between WBLM and Janssen schemes for hurricane Dorian. Snapshot: 17:00 UTC 05/09/2019

waves when the WBLM is used for the simulations. In all figures the mean sea level pressure as calculated by the WBLM source input function is plotted on top as a reference of the location and the intensity of the cyclones.

5.3.1 Hurricane Dorian

The snapshot of the area and time of a peak of hurricane Dorian (05/09/2019 17:00 UTC) is displayed in Figure 5.8. The plot indicates an increase of the wind speed close to the eye of the cyclone when the WBLM scheme was used. This is the same area where the highest winds appear. The increase as found from the map is about 3 m/s or more. Further away from the eye, there is an evident reduction of the winds speeds at 10 m height as calculated by the WBLM (Figure 5.8a). That shows that for extreme winds, WBLM succeeds in strengthening the winds, that has been proven to be underestimated by Janssen's scheme (Jenssen and Cardone, 2006; Pineau-Guillou et al., 2018).

At the same time the significant wave height in the area of the hurricane is generally smaller for WBLM, with bigger differences located at the east side of the cyclone, and especially the right back quadrant of the cyclone. The differences reach about 1.6 m or more (Figure 5.8b).

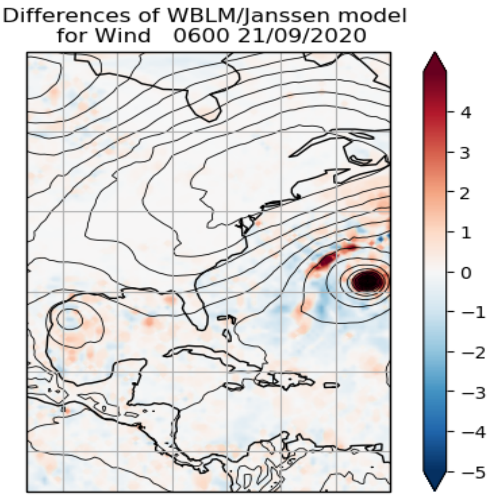

(a)

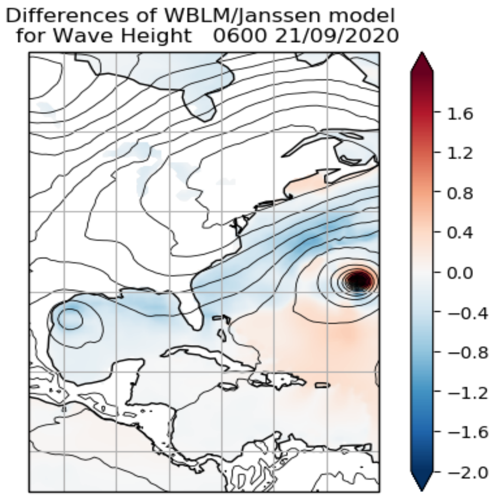

(b)

FIGURE 5.9: Horizontal distribution of (a) wind speed differences and (b) significant wave height between WBLM and Janssen schemes for hurricane Teddy. Snapshot: 06:00 UTC 21/09/2020

5.3.2 Hurricane Teddy

For hurricane Teddy, the snapshot of the 21st of September 2020 at 6:00 UTC (Figure 5.9), shows that there is an obvious increase for both wind speeds and wave heights close to the centre of the cyclone. Particularly, wind speeds calculated from WBLM exceed a 4 m/s increment compared to the winds calculated from Janssen's scheme. At the outer part of the cyclone there is a decrease of the winds of about 2 to 3 m/s. Again, at the outer part of the cyclone there is a high increment of the wind speeds in the front quadrant of the hurricane (Figure 5.9a).

The significant wave height (Figure 5.9b) shows similar behaviour as for the wind speed when the new source input function is used for the simulations. Again, in the centre of the hurricane the highest differences are observed, where the WBLM waves are even >1.6m higher than the ones calculated from

Janssen's source input function. In the outer part there is a small decrease of the wave height (around 0.4 m), but interestingly there is a small increment in the SW part of the cyclone even though wind speeds have decreased in the same area when using the WBLM.

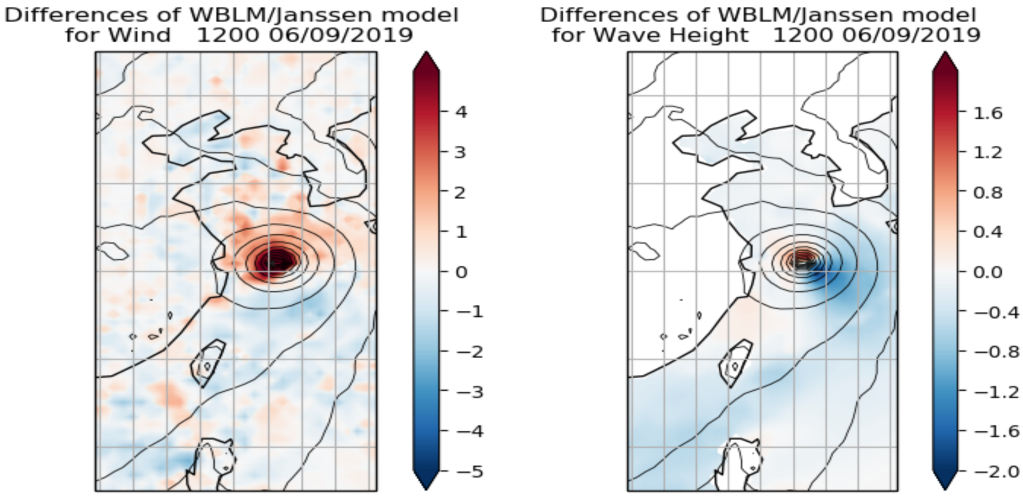

(a) (b)

FIGURE 5.10: Horizontal distribution of (a) wind speed differences and (b) significant wave height between WBLM and Janssen schemes for typhoon Lingling. Snapshot: 12:00 UTC 06/09/2019

5.3.3 Typhoon Lingling

For typhoon Lingling, Figure 5.10 shows the snapshots of wind speeds at 10m and significant wave height for the 6th of September 2019 at 12:00 UTC. Figure 5.10a plot of the wind shows that 10m wind speeds increased when the WBLM is used in the forecasts. Differences are even greater than 4 m/s in the same areas. For the north part of the cyclone there is still some increase when the WBLM is used (about 2 m/s). Contrarily, winds at the southern part of the cyclone are higher when Janssen's scheme is used for the predictions.

Lingling's significant wave height (Figure 5.10b) gives a general decrease in the area of the Yellow and East China Sea when the WBLM is used. Interestingly, the left front quadrant of the typhoon has the highest increment in the significant wave height when the WBLM is used (about 1.2 m) and the right rear quadrant of the cyclone has the highest decrease of the significant wave height when the new source input function is turned on in the model (about 1.2 m).

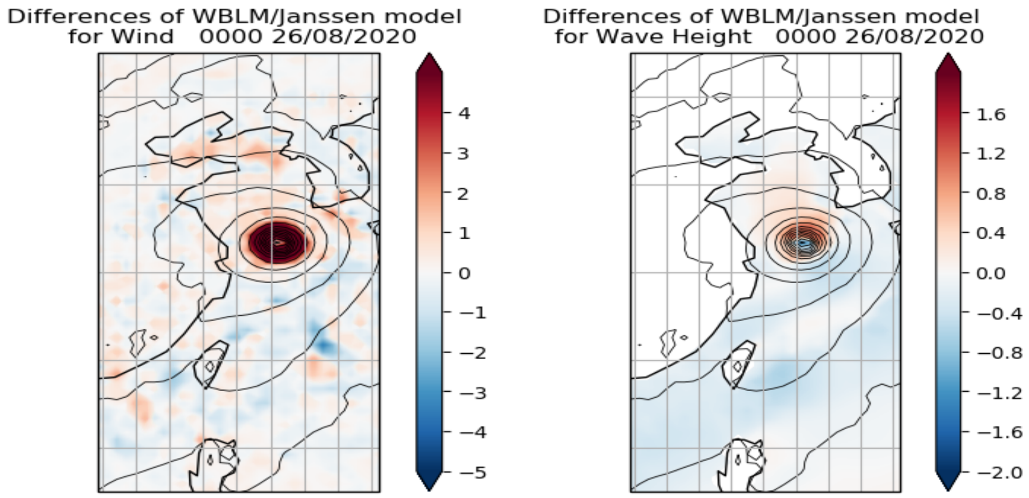

(a) (b)

FIGURE 5.11: Horizontal distribution of (a) wind speed differences and (b) significant wave height between WBLM and Janssen schemes for typhoon Bavi. Snapshot: 00:00 UTC 26/08/2020

5.3.4 Typhoon Bavi

The WBLM-Janssen 10 m wind speed differences map for typhoon Bavi (Figure 5.11a), for the 26th of August 2020 00 UTC, shows that the whole central part of the cyclone is increasing when the new approach is used for the model predictions. The difference reaches values above the 5 m/s and creates an almost perfect cycle following the shape of the isobars. Generally, in the area of the Yellow and East China Sea their parts that Janssen calculates higher winds speeds, but for the extreme conditions there is only an increase of winds speeds when the new approach is used for the simulations.

For the significant wave height (Figure 5.11b) most of the cyclone has an increase of the waves around 0.4 to 0.8 m. Only in the centre of the typhoon, close to the eye, a small decrease of the wave height, around 0.4 m, is observed when the WBLM is turned on for the simulations.

5.4 Summary

This chapter examined the impact of the implementation of the new approach on calculating the source input function, both on the global prediction as well as in specific extreme events (Tropical Cyclones). The analysis was based on the global domain for correlation plots of Charnock and drag coefficient with the surface wind, as well as on wind intensity and direction spatial distribution. Results from this part of the analysis showed that the WBLM reduces the drag and the Charnock coefficients estimations compared to Janssen's scheme. In cases of moderate to high wind speeds, for the Charnock coefficient values are even half than the corresponding values calculated from Janssen's scheme, where maximum values from WBLM are around 0.05 and from Janssen they are 0.1. For extreme wind speeds, as is the case for tropical cyclone events, the reduction of Charnock is similar, where the higher values are about 0.055 for Janssen and 0.025 for WBLM. Corresponding results of the drag coefficient, show that WBLM for most of the time is closer to the mean values, while Janssen's scheme has a lot of scatter around the mean. For extreme winds, the reduction of the drag coefficient is a lot more evident where maximum values of drag coefficient from Janssen scheme are about 0.005, while for the same area the drag coefficient from the WBLM is less than 0.004. The main parameters that are significantly affected by the switch of an input function scheme, and the ones that are closely linked to everyday life and economic sectors are the significant wave height and the 10m wind speed. It was then clear that testing the impact of the WBLM on these parameters during the extreme conditions was important for the analysis. The wind distribution showed that for very low winds the density is lower when the WBLM is turned on in the model.

For winds between 5-12 m/s the density is higher when the WBLM is used for the runs, sifting the winds more towards moderated areas. For higher wind speeds the distribution is again lower when the WBLM is used. However, this type of plots gives only a general picture of the distribution, while lacking on resolution. For this reason wind roses were produced in order to better analyse the impact of the new approach on the wind intensities and directions. From the wind roses extreme values of wind values were more visible. These results showed that in some cases extreme wind speeds are increased when the WBLM is used. Generally, the direction remains the same with only small shifts observed. For increasing the understanding on the changes due to the WBLM on the extreme conditions, the analysis was then moved in the specific area of the extreme events. Maps of differences of winds and waves between the two schemes revealed that in extreme conditions the underestimations of the wind speeds when using Janssen's scheme is even higher (even for more than 4 m/s in certain cases). The significant wave height is overall decreased when using WBLM while in places some increases were found (e.g., eye of the typhoon/hurricane).

Chapter 6

Validation of WBLM with in-situ Observations

6.1 Introduction

In this chapter each case study is analysed separately, by focusing on the area of the event, and not on the whole (global) domain. Here the total time of the forecast is used in order to examine the evolution of the cyclones, as well as validating the model results against real observations. The goal is to specifically examine how the scheme impacts the extreme conditions and especially the peak of the cyclones. In addition, the timeseries of wind speeds and significant wave height produced, will help to follow how the evolution of the storm is captured by the two schemes. Using the same in-situ stations for each case study, statistical analysis for the significant wave height is carried out using the Taylor plots. Taylor diagrams (Taylor, 2001) allow graphical summaries of how much a model or a set of different models succeeded in predicting observations. The plot includes the correlation coefficient, root-mean-square difference and the standard deviations of the predicted values to the real values. This type of diagram has been found useful in order to evaluate the model skill. The position of each scheme on the diagram quantifies how well the simulated significant wave height matches the observations. Here centered root-mean-square (RMS) is indicated by the black dotted contour, the correlation coefficient is shown with the dashed dotted lines, and black dotted lines present the standard deviation. Observations are shown with the red dotted line. In addition to that, statistics are also summarised in corresponding tables.

6.2 Hurricane Dorian

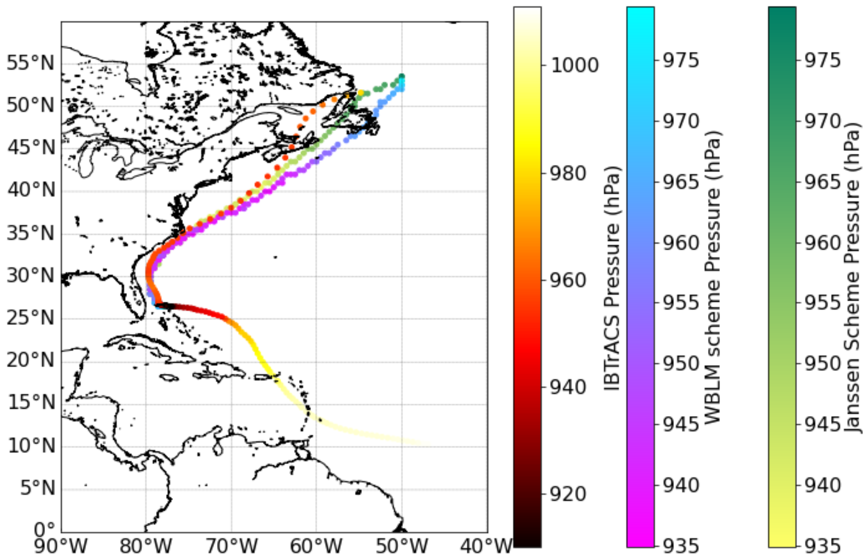

FIGURE 6.1: Comparison of Hurricane Dorian Trajectory as taken by the model output using WBLM (pink to light bue corobar) and Janssen (yellow to green colorbar), with the real trajectory from the IBTrACS dataset

.

Both schemes have successfully predicted the trajectory of hurricane Dorian (Figure 6.1), at least for the first part, which is also the area where the buoys used for the analysis are located. As the hurricane propagates and moves towards landfall to Nova Scotia, both schemes are quite off the hurricanes real trajectory. The main reason for this issue is that as the hurricane moves towards the land, the forecast moves further away from the initial condition date, which can cause inaccurate predictions. At that forecast time range (over 7 days), a single forecast is not enough. Operational centres rely on producing an ensemble of forecasts in an attempt to capture the inerrant uncertainty of the forecast to guide forecasters.

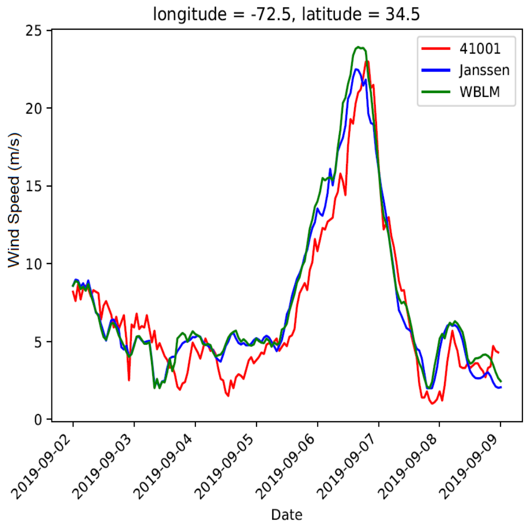

(a)

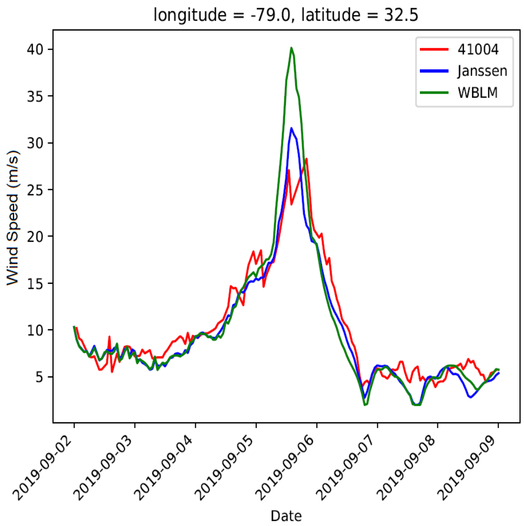

(b)

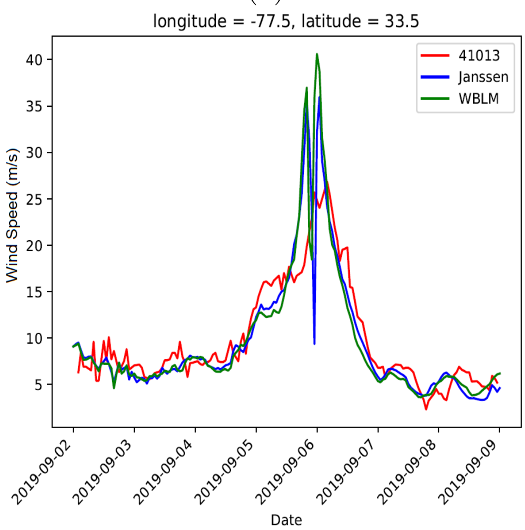

(c)

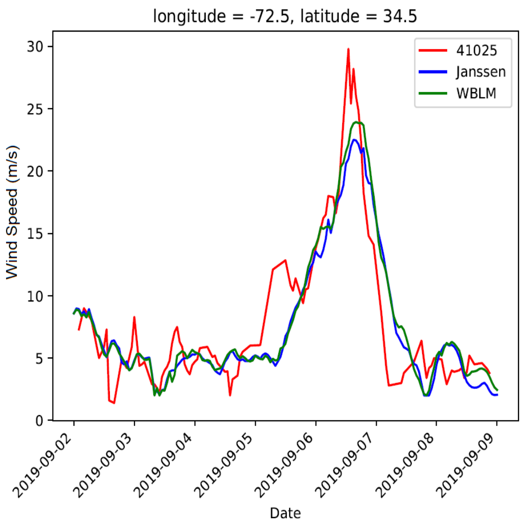

(d)

FIGURE 6.2: Comparisons of wind speed timeseries for hurricane Dorian. WBLM is shown with green line, Janssen is shown with blue, and the in-situ observations for buoys (a) 41001, (b) 41004, (c) 41013 and (d) 41025 with red.

Using in-situ observations from buoys, simple validation of the schemes is achieved by plotting the timeseries of the evolution of the significant wave height and the wind speed as shown in Figure 6.3 and Figure 6.2, respectively.

For buoy 41001 (Figure 6.3 a) , which is at the deepest point compared to the rest of the stations, results show that both models have correctly represented the magnitude and duration of the hurricane. Janssen's scheme is found to agree better with the peak point, but seems to miss local peaks, like the one on the 8th of September, which WBLM appears to have captured, albeit with a delay. Similarly, the wind speeds at 10m height (Figure 6.2 a), for the same location, display good agreement between the two models and the observations. Here it is found that both, the WBLM and the Janssen schemes have predicted peak points rather well. Both have lost the sharp drop of the wind on the 5th of September. For the peak points of the wind, again the two models have successfully predicted it, only slightly sooner than it happened.

WBLM and Janssen highly agree at 41004 buoy (Figure 6.3 b). However, they have both overestimated the peak height. For lower wind speeds, both have similar problems, missing how the wave developed during the 3rd and 4th of September 2019, and underestimating the wind speed before the peak occurs, giving a very steep change. For this station, there is a big overestimation of winds from the WBLM, whereas Janssen gave a better prediction of the wind speed. For low and moderate winds both source input functions have worked similarly well (Figure 6.2 b).

Real observations for the significant wave height at buoy 41013 (Figure 6.3 c) agree better with WBLM predictions for the peak of the hurricane. WBLM, as well as Janssen's scheme, have predicted a big drop of the waves height, which is not shown from the observations. This implies that in the models, the eye of the storm has passed over the buoy locations, whereas in reality the buoy stayed slightly off the eye. However, after this drop, Janssen continues to have a quite big overestimation of the wave height, while WBLM achieves a better agreement to the measurement. For the low and moderate wind speeds there are similar problems as mentioned before. The drop of the significant wave height

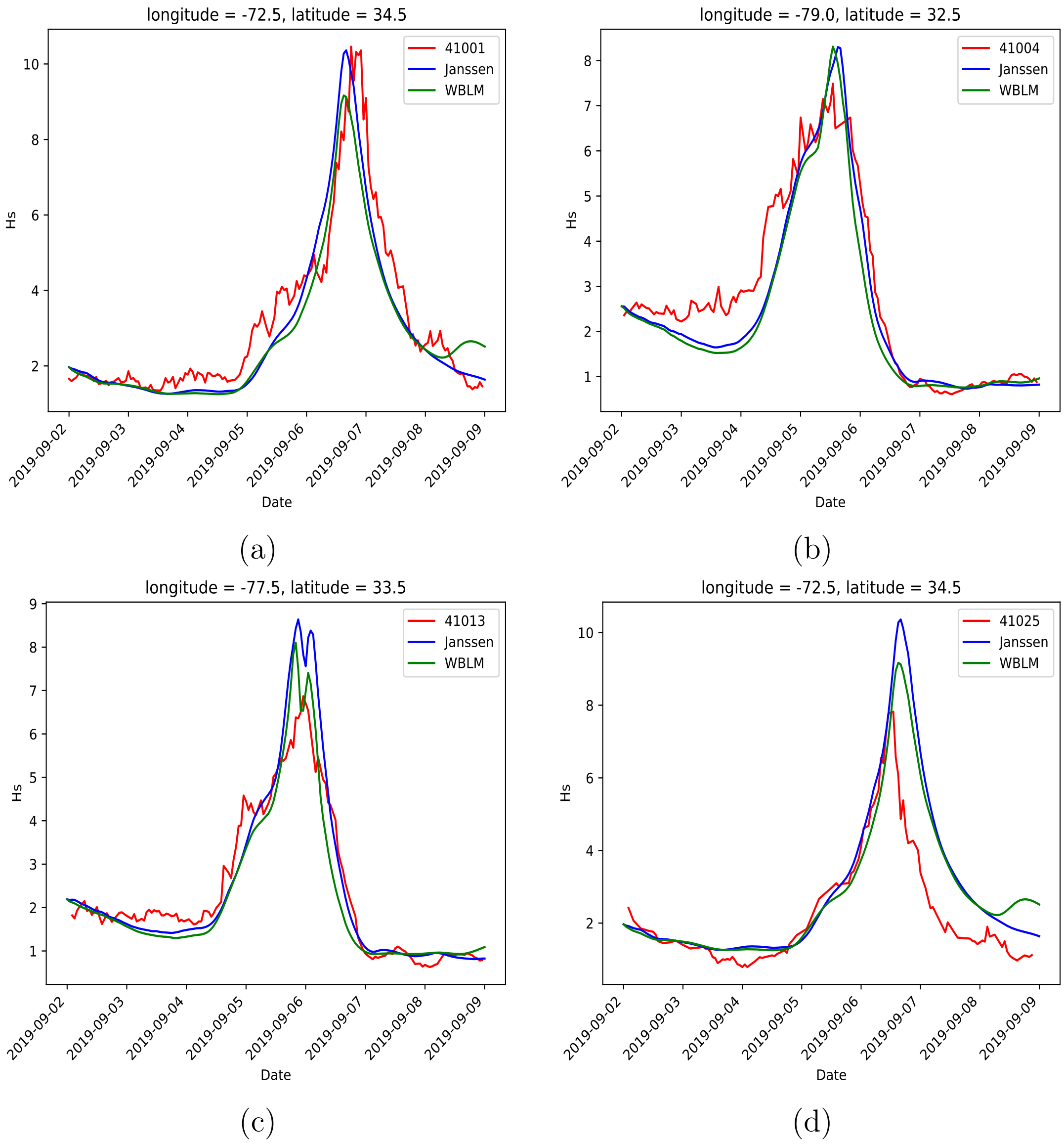

FIGURE 6.3: Comparisons of the significant wave height timeseries for the case of hurricane Dorian. WBLM is shown with green line, Janssen is shown with blue, and the in-situ observations for buoys a) 4001, (b) 41004, (c) 41013 and (d) 41025 with red.

is supported from the timeseries of surface wind speeds (Figure 6.2 c). There is again a big drop on the prediction of the winds, which is not explained by the real observations. Here both input functions have generally overestimated the wind speed for the peak and underestimated it in all other times.

Buoy and model comparisons for the location 41025 show that Janssen has highly overestimated the significant wave height (Figure 6.3 d), while WBLM is lower, but still above the real recordings. There is also an obvious overestimation of the wave height after the peak. Regarding the wind speeds, Figure 6.3d shows an underestimation from both schemes, both at the peak point, as well as in most of the other times. Once again WBLM appears to be closer to the real values.

Statistical results for hurricane Dorian are presented in Figure 6.4 and in Table 6.1. For station 41001 it is shown that the correlation of Janssen's scheme with the observations is about 0.95, while for WBLM it is 0.93. The RMS error for Janssen is 0.72, while the RMS error for the WBLM is 0.78. For the standard deviation the distance of the radial from the origin shows that WBLM standard deviation, which is about 1.92, is clearly lower that the red arc line of the observations which is 2.18m. Janssen's standard deviation is higher (2.22), but closer to the one for observations.

For buoy 41004, the correlation coefficient for Janssen is 0.91 and for WBLM is 0.90. The RMS error is 0.83 for Janssen's scheme and 0.84 for WBLM. The standard deviation is 2.01 and 1.91 for Janssen and WBLM, respectively. In this case, both schemes give higher standard deviation compare to the observations, which reaches a value of 1.89.

For buoy 41013, the correlation coefficient for WBLM slightly lower (0.94) than the one for Janssen scheme (0.95). The RMS error between the observations and the simulated values of Janssen is 0.68, while the RMS error of the WBLM is significantly lower (0.56). Janssen gives again high standard deviation (2.03) than the one from WBLM (1.73). Furthermore, the standard deviation given by the observations was the lowest value.

Finally, for buoy 41025, the correlation coefficient of Janssen is 0.86 and it is 0.83 for WBLM. The RMS error of Janssen is higher (about 0.13) than the one of WBLM, of about 0.13. As in most of the previous buoys, SWH the observational standard deviation is again lower (1.54) compare to Janssen (2.23) and WBLM

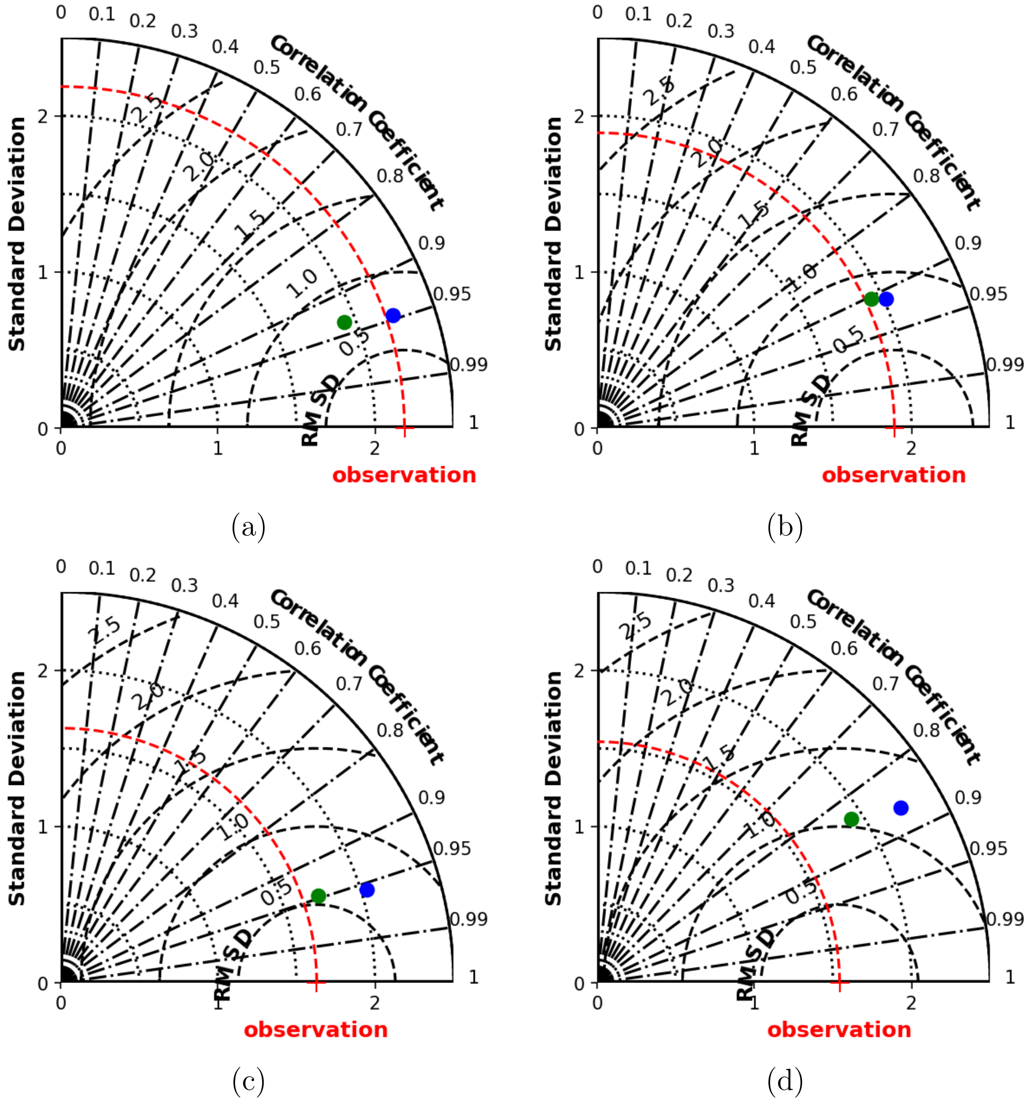

FIGURE 6.4: Taylor plots for Dorian Hurricane, where WBLM is shown with green dot, Janssen is shown with blue dot, and the in-situ observations with the red cross. (a) is for buoy 41001, (b) for 41004, (c) for 41013 and (d) for 41025

(1.92)

6.3 Hurricane Teddy

For hurricane Teddy, the trajectory of the cyclone as calculated by the WBLM scheme agrees well with the data from the IBTrACS (Figure 6.5). Some errors in capturing the track are again found when the run is further into the forecast, with WBLM giving better predictions than the default source input of Janssen's

TABLE 6.1: Comparison of the main performances between Janssen and WBLM of the simulated significant wave height against observations during Hurricane Dorian. Records (of each buoy): 169

Buoy 41001

	Janssen	WBLM
CC	0.95	0.93
RMSE	0.72	0.78
STD obs	2.18	2.18
STD model	2.22	1.92

Buoy 41004

	Janssen	WBLM
CC	0.91	0.90
RMSE	0.83	0.84
STD obs	1.89	1.89
STD model	2.01	1.92

Buoy 41013

	Janssen	WBLM
CC	0.95	0.94
RMSE	0.68	0.56
STD obs	1.63	1.63
STD model	2.03	1.73

Buoy 41025

	Janssen	WBLM
CC	0.86	0.83
RMSE	1.18	1.05
STD obs	1.54	1.54
STD model	2.23	1.92

scheme.

The locations of the available stations from the moored buoy data were not in good agreement with the trajectory of this cyclone case. Additionally, good quality drifting buoy data for the significant wave height were available as part of a targeted deployment ahead of the hurricane (new technology based on GPS signal processing to retrieve wave information). For this reason, in this section the analysis is done in a somewhat different way. Evolution timeseries plots

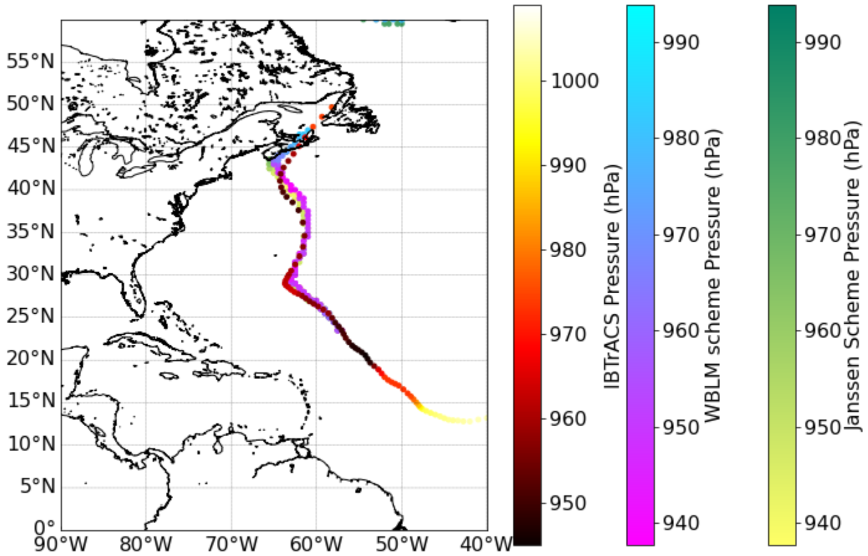

FIGURE 6.5: Comparison of Hurricane Teddy Trajectory as taken by the model output using WBLM (pink to light bue corobar) and Janssen (yellow to green colorbar), with the real trajectory from the IBTrACS dataset

.

for wind speeds and wave heights are made for only two stations of moored buoy data. However, data from 8 drifting buoys are plotted against collated short-range forecasts (1 day) for both schemes.

For the wind speeds at 10 metres it is shown that both schemes agree with the observations during the peak intensity of the hurricane. However, they are both off when it comes to the changes of the wind intensity after the typhoon passage. Around the 23rd and the 25th of September, there is a big underestimation and then overestimation respectively, of about 2m/s for both schemes. Predictions of the significant wave height from both the default and the new approach for the location close to buoy 41047 give a big underestimation, of about 2m (Figure 6.7a).

Measurements of surface wind speed from buoy 41049 are in better agreement with the WBLM predictions, while Janssen's scheme gives an underestimation

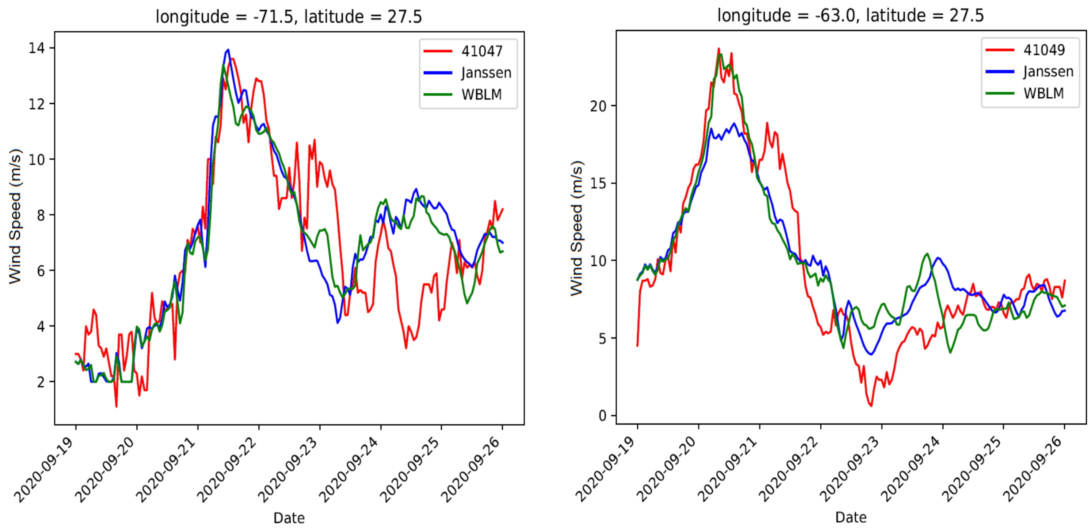

(a) (b)

FIGURE 6.6: Comparisons of wind speed timeseries for hurricane Teddy. WBLM is shown with green line, Janssen is shown with blue, and the in-situ observations for buoys (a) 41047, and (b)41049 with red.

of 2.5 m/s (Figure 6.6b). Both schemes were unable to capture the increment of the wind after the peak (around 01 UTS of the 21st of September), while later they both overestimated the peaks just before the 24th of September.

For the significant wave height at the same location, both models have successfully captured the peak, with the WBLM predicting it accurately. The inaccuracy of the second peak shown on Figure 6.7b, is also found here, where the two schemes underestimate the 21st of September at 01 - 02 UTC of about 2m.

The comparison of the short-range forecast (20 to 21st of September) against observations from the drifting buoys (Figure 6.7c,d), show that both schemes underestimate the significant wave height when low waves occur (2.4m). However, for high waves (above 6 m) both models for most tend to overestimate the significant wave height. Th biggest biases is with buoys 4101789 and 4101794. Generally, both source input functions estimate well the significant wave height at boys 4101791 and 4101793. Buoy 4101805 shows similar relation to both source input functions. In general, based on the drifting buoy data it is shown that

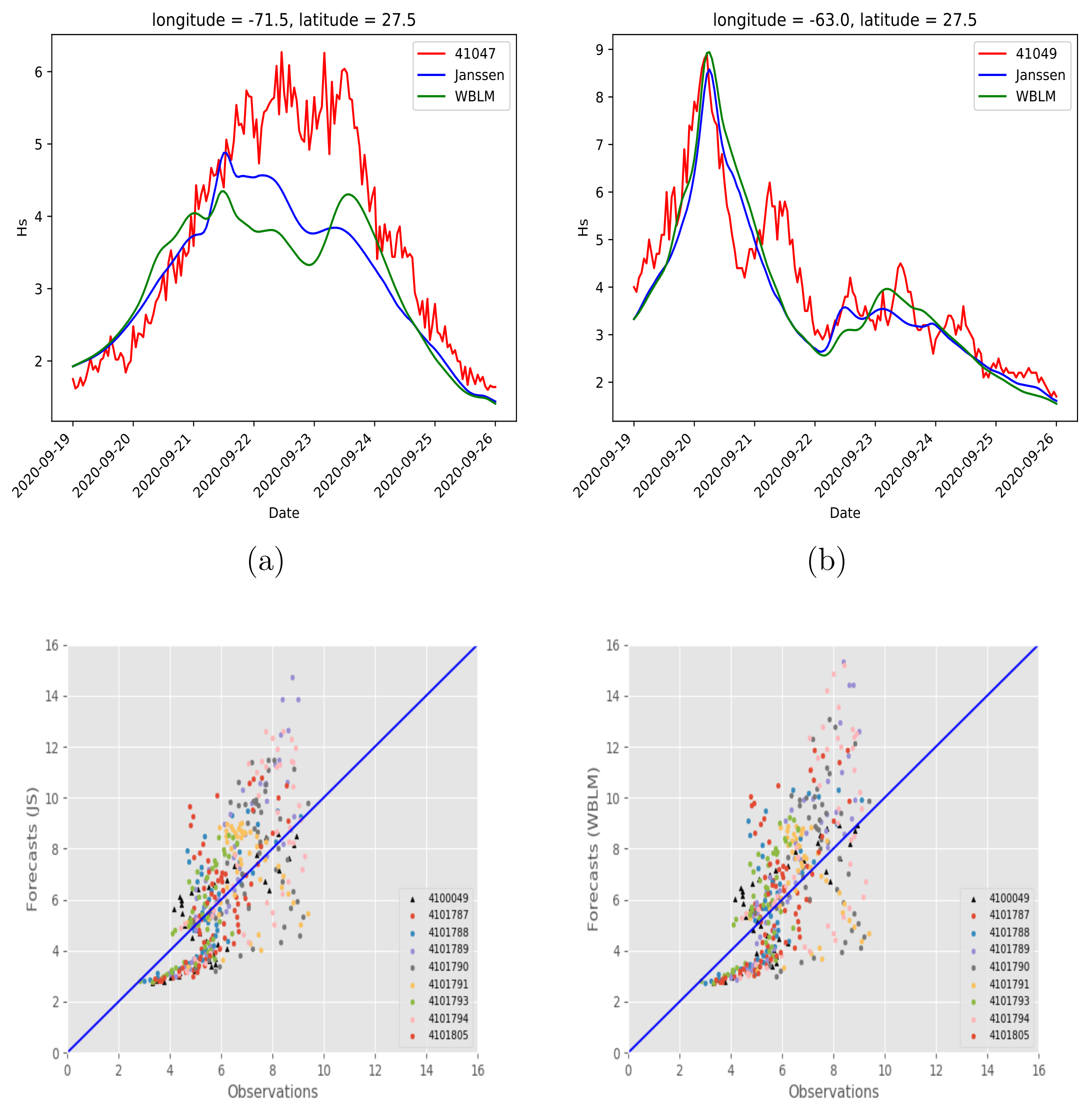

(a) (b)

(c) (d)

FIGURE 6.7: Comparisons of the significant wave height for the case of hurricane Teddy. Timeseries in subplots (a),(b) show WBLM is shown with green line, Janssen is shown with blue, and the in-situ observations for buoys (a) 41047, and (b) 41049 with red. Sub-plots (c) and (d) are collated short range forecasts of 1 day (20-21 of September 2020) against 8 drifting buoys data (as shown on the plot).

estimations of the significant wave height for hurricane Teddy from Janssen's scheme are closer to the observed values.

For Hurricane Teddy, only two stations of the total seven days forecast (41027 and 41049) are used for the statistical analysis. The results are given in Figure 6.8 and on Table 6.2.

For station 41047, it is shown that Janssen has better correlation with the observations (0.90), compare to WBLM (with smaller correlation, 0.84). The RMS error is again better for Janssen (0.71) in contrast to the WBLM (0.85). However, the standard deviations from both models are smaller than the one from the observations (1.46), while WBLM showed the lowest scatter around the mean (0.98 for Janssen and 0.90 for WBLM).

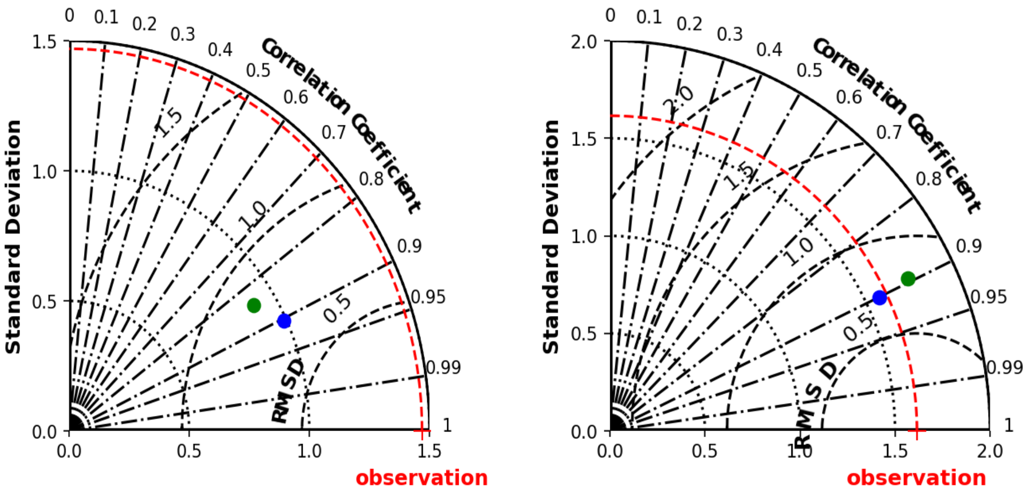

(a) (b)

FIGURE 6.8: Taylor plots for Hurricane Teddy, where WBLM is shown with green dot, Janssen is shown with blue dot, and the in-situ observations with the red cross. (a) is for buoy 41047, (b) for 41049

Equally to station 41047 Janssen gives slightly higher correlation coefficient (0.90) against WBLM (0.89) for buoy 41049, with again better RMSE (0.71 for Janssen against 0.78 for WBLM). The standard deviation of the observations is about 1.61, while for Janssen it is 1.57. WBLM presents the highest STD value at around 1.74.

6.4 Typhoon Lingling

Similarly to the hurricane cases, we first look at the trajectory of the cyclone. For typhoon Lingling (Figure 6.9) both schemes are in very good agreement with the trajectory from the observations. A small-scale offset is found as the

Table 6.2: Comparison of the main performances between Janssen and WBLM of the simulated significant wave height against observations during Hurricane Teddy. Records (of each buoy): 169

Buoy 41047

	Janssen	WBLM
CC	0.90	0.84
RMSE	0.71	0.85
STD obs	1.46	1.46
STD model	0.98	0.90

Buoy 41049

	Janssen	WBLM
CC	0.90	0.89
RMSE	0.71	0.78
STD obs	1.61	1.61
STD model	1.57	1.74

cyclone moves into inshore waters (Yellow sea) and before its landfall. Again, the known issue of the inaccurate predictions when we are further into the forecast can explain the errors found here.

As buoys 22191 and 22192 were not available during the time of the event of typhoon Lingling. The best possible option from the database of ECMWF was buoy 22184 (Figure 6.10). Timeseries show that the WBLM slightly overestimates the peak of the wind speeds at the location of buoy 22184, while Janssen's scheme is in very good agreement with the observations. In addition, both source input functions are about half an hour late at the peak point. At the same time, the WBLM overestimates the second increment at the highest winds which is the reason for the overall overestimation. For low and moderate winds, similarly to the previous case studies, both schemes miss to accurately capture the local peaks, particularly after the passage of the typhoon. However, during these intensities the WBLM better predicted the surface winds, and this is more obvious during the last local peak.

Figure 6.11 shows the timeseries for the significant wave height for the location

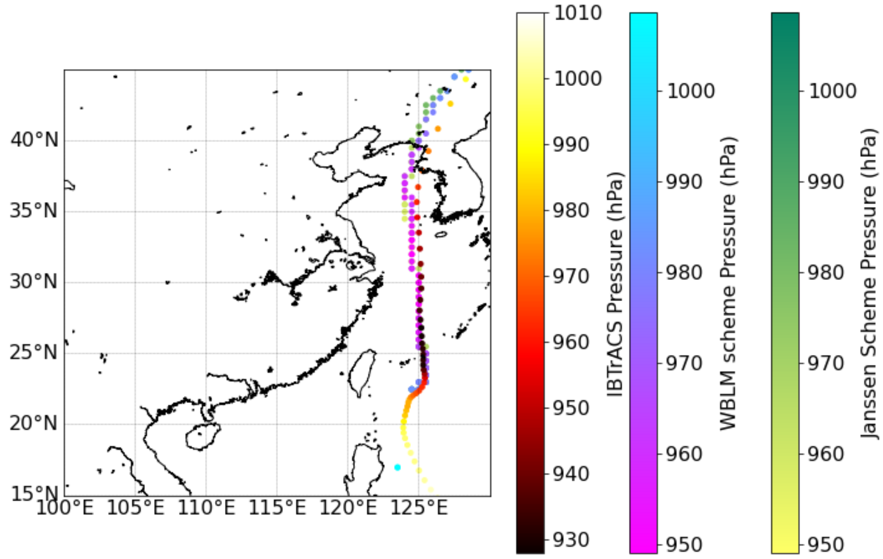

FIGURE 6.9: Comparison of Typhoon Lingling Trajectory as taken by the model output using WBLM (pink to light bue corobar) and Janssen (yellow to green colorbar), with the real trajectory from the IBTrACS dataset

.

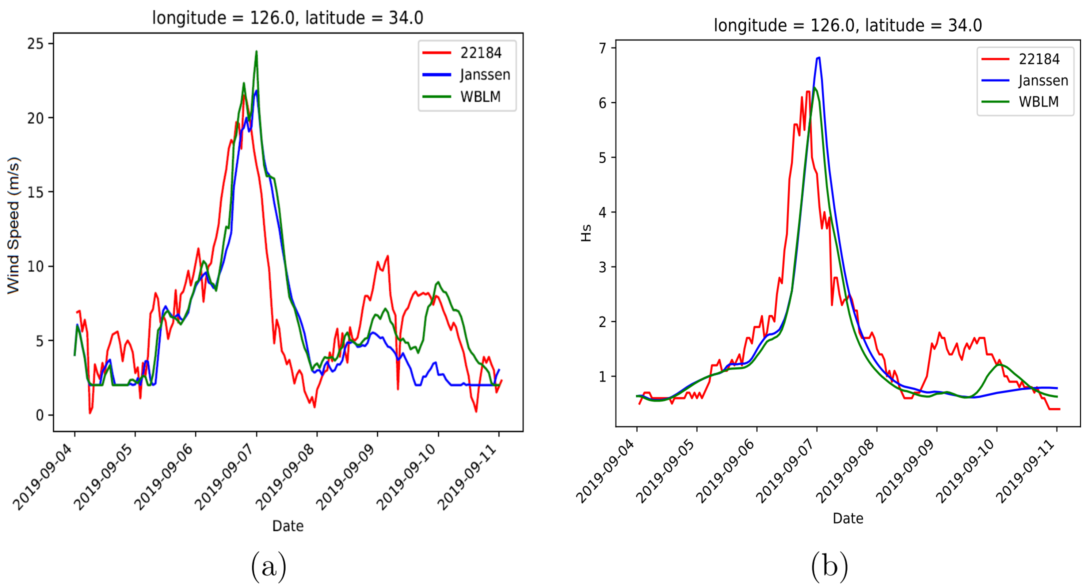

FIGURE 6.10: Comparisons timeseries for (a) wind speed and (b) significant wave height for typhoon Lingling at buoy 22184. WBLM is shown with green line, Janssen is shown with blue, and the in-situ observations with red.

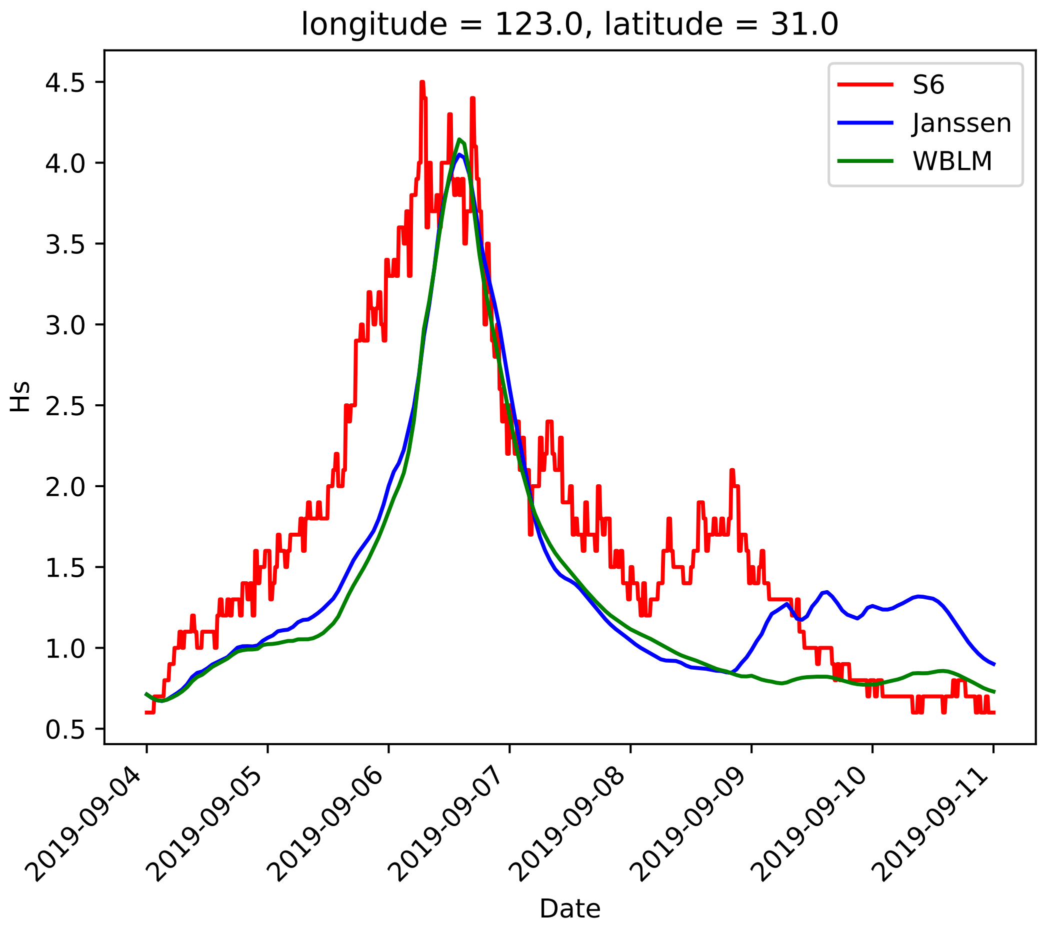

Figure 6.11: Timeseries of the significant wave height for the case of Lingling for location of Buoy S6. WBLM is shown with green line, Janssen is shown with blue, and the in-situ observations with red.

of buoy S6. As mentioned before, that is an extra location of which the data have been received from Yellow Sea Ocean/East China Sea Observation and Research Station of OMORN.

Observations from buoy 21184 for the significant wave height show better agreement to the WBLM predictions, while Janssen's scheme overestimates the results. Both schemes were unable to capture the increase of the wave around the 9th of September 2019, however the WBLM reacted better to the change. Buoy S6, shows that both models are in good agreement to the observations. WBLM is slightly closer to the peak of the observations; however, Janssen's source input function is able to reproduce the local peak after the typhoon passage, although delayed.

Similarly to the hurricane cases, basic statistical analysis for Typhoon Lingling is also presented in Taylor plots (Figure 6.12) and corresponding statistics tables (Table 6.3) for the two available stations (22184 and S6).

TABLE 6.3: Comparison of the main performances between Janssen and WBLM of the simulated significant wave height against observations during Typhoon Lingling. Records (of each buoy): 169

Buoy 22184

	Janssen	WBLM
CC	0.80	0.83
RMSE	0.84	0.73
STD obs	1.29	1.29
STD model	1.38	1.26

Buoy S6

	Janssen	WBLM
CC	0.81	0.87
RMSE	0.55	0.46
STD obs	0.95	0.95
STD model	0.78	0.82

Results showed that for both stations, WBLM has higher correlation coefficients than the one given from the simulations using Janssen's parameterisation (0.83 against 0.80 at 22184 and 0.87 against 0.81 at S6). Correspondingly, RMS errors decrease (to 0.73 from 0.84 for 22184 and from 0.55 to 0.46 for buoy S6) against the corresponding values (0.80 and 0.81 for correlation coefficients; 0.84 and 0.55 for RMSE). Particularly, the RMSE of the model comparison against S6 buoy is one of the lowest values found. Standard deviations from both schemes are slightly high for buoy 22184 (1.38 for Janssen and 1.26 for WBLM), while for S6 STD for both schemes is lower (0.78 for Janssen and 0.82 for WBLM). In both cases observational standard deviation was high (1.29 for 22184 and 0.95 for S6).

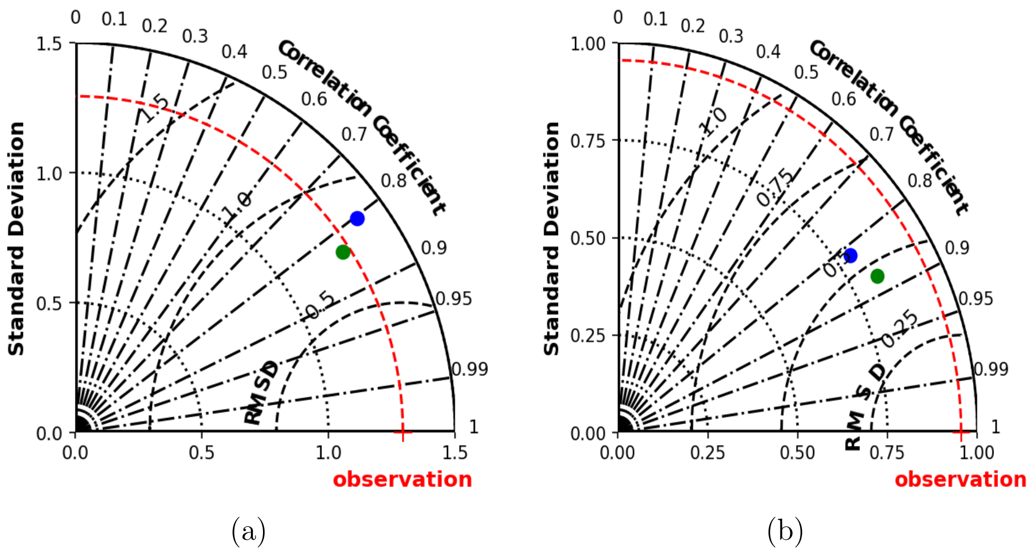

FIGURE 6.12: Taylor plots for Typhoon Lingling, where WBLM is shown with green dot, Janssen is shown with blue dot, and the in-situ observations with the red cross. (a) is for buoy 22184, (b) for S6. Records (of each buoy): 169

6.5 Typhoon Bavi

Comparing the trajectory from the IBTrACS with the trajectories given from the two source input functions, it is shown that initially both schemes have problems in correctly tracing the beginning of the typhoon path (Figure 6.13). However, later in time and for the section of the track with the highest intensity, both the WBLM and the Janssen's scheme are in very good agreement with the observed path. Similar to all previous cases, the schemes are slightly offset after the landfall of the cyclone, where the friction is higher.

Timeseries for the wind speeds and significant wave height are shown in Figures 6.14 and 6.15. Results show that both schemes captured the magnitude and the growth of the winds and waves fairly well.

At station 22103 (Figure 6.14a) there is a small overestimation of the wind speed from Janssen, while WBLM agrees slightly better with the observations. Both schemes have predicted the local peaks after the passage of the typhoon. However, they overestimated them, and the response in the changes is delayed.

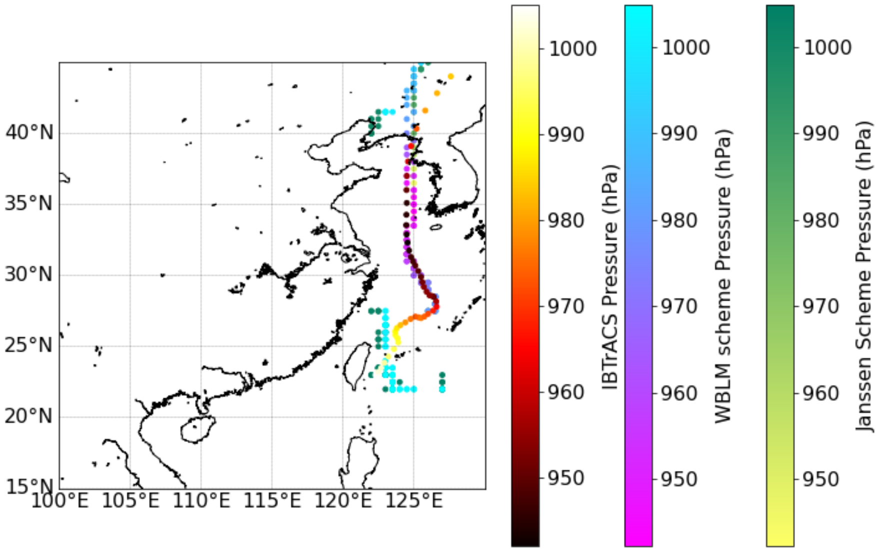

FIGURE 6.13: Comparison of Typhoon Bavi Trajectory as taken by the model output using WBLM (pink to light bue corobar) and Janssen (yellow to green colorbar), with the real trajectory from the IBTrACS dataset

.

For the significant wave height, Janssen's scheme agreed better with the observations, where a big underestimation of the waves height is shown for the WBLM (Figure 6.15a). Once again, both schemes had issues to resolve the local peaks and disruptions.

Buoy 22187 (Figure 6.14b), the model wind speeds are similar for both models, which are found to overestimate the observations. The significant wave height as simulated with the WBLM agrees better with the buoy measurements, while Janssen's scheme gives a small overestimation of the significant wave height (Figure 6.15b).

Wind speeds close to the location of buoy 22191 show that there is a very big overestimation from WBLM close to 15 m/s for the peak of the typhoon. The predicted significant wave height using the WBLM agrees very well with the

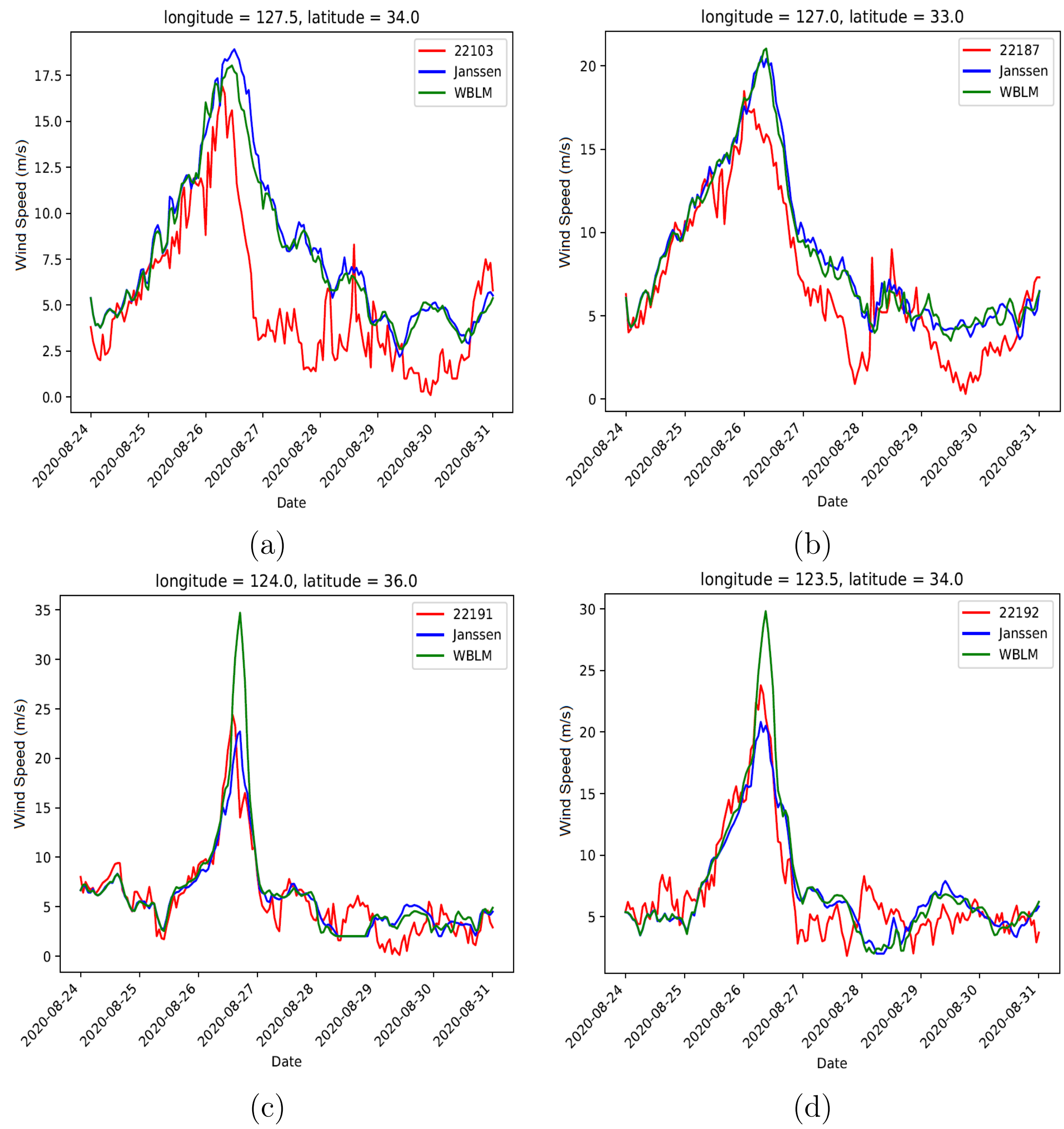

FIGURE 6.14: Comparisons of wind speed timeseries for typhoon Bavi, where WBLM is shown with green line, Janssen is shown with blue, and the in-situ observations for buoys (a) 22103, (b) 22187, (c) 22191 and (d) 22192 with red.

observations, while Janssen underestimates the peak waves, even up to 2m. Finally, at buoy 22192 (Figure 6.14c) there is again high overestimation of the wind speeds from the WBLM (up to 5 m/s). At the same point, Janssen underestimates the wind speeds, but it is closer to the observed values. For the significant wave height (Figure 6.15c), there is a small overestimation from the WBLM, however this is not considered as significant as for the wind speed. For this location, Janssen shows a very good agreement with the buoy observations.

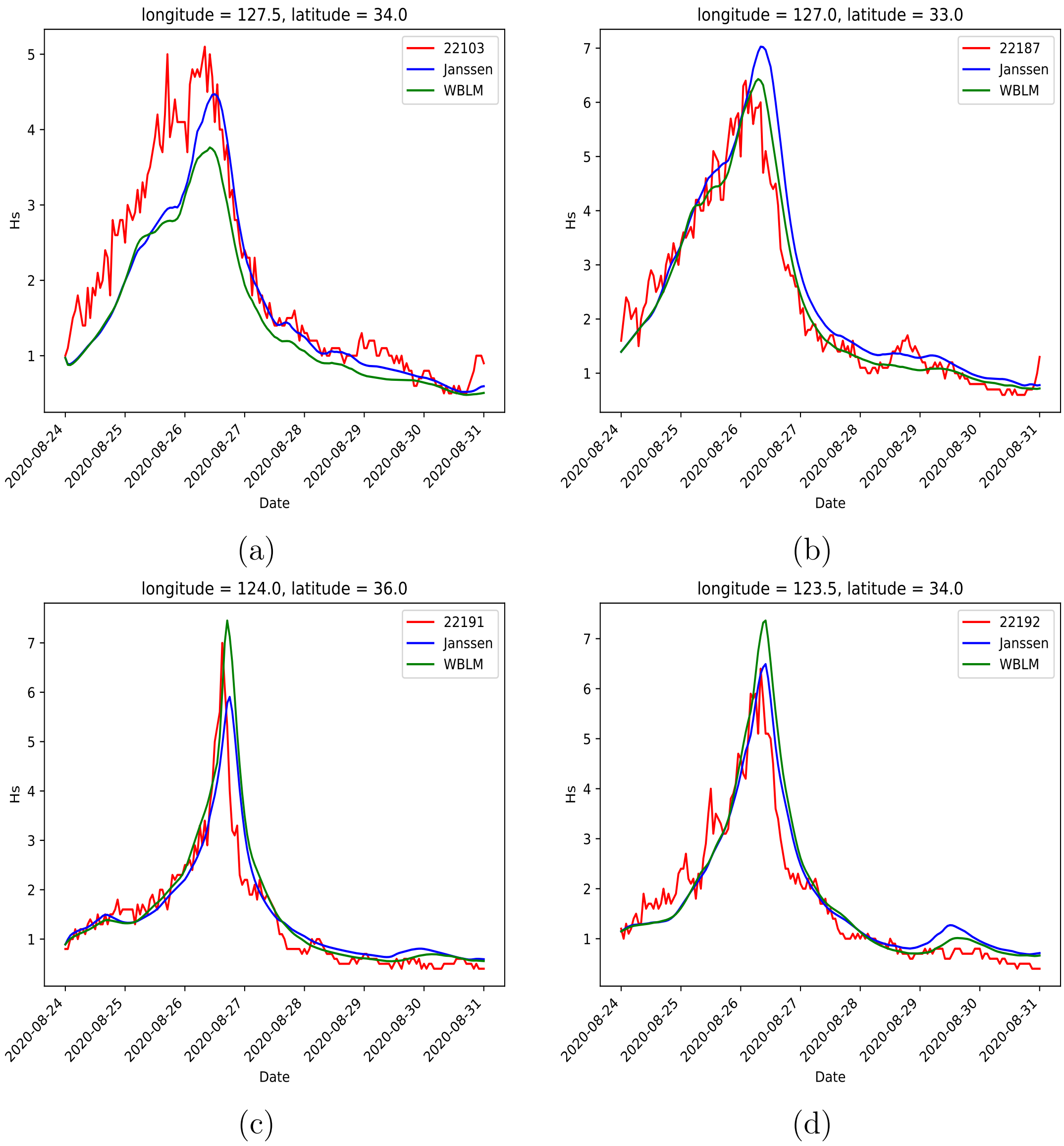

FIGURE 6.15: Comparisons of significant wave height timeseries for the case of typhoon Bavi. WBLM is shown with green line, Janssen is shown with blue, and the in-situ observations for buoys (a) 22103, (b) 22187, (c) 22191 and (d) 22192 with red.

Buoys that gave inaccurate predictions were in the main path of the typhoon (22191, 22192), which could reveal an issue for the scheme (more in the discussion).

For the case study of typhoon Bavi, statistical analysis is based on the observations of the four available buoys (22103, 22187, 22191 and 22192), and results are shown in Figure 6.16 and on Table 6.4.

Comparison between model output for the two schemes and buoy 22103 showed

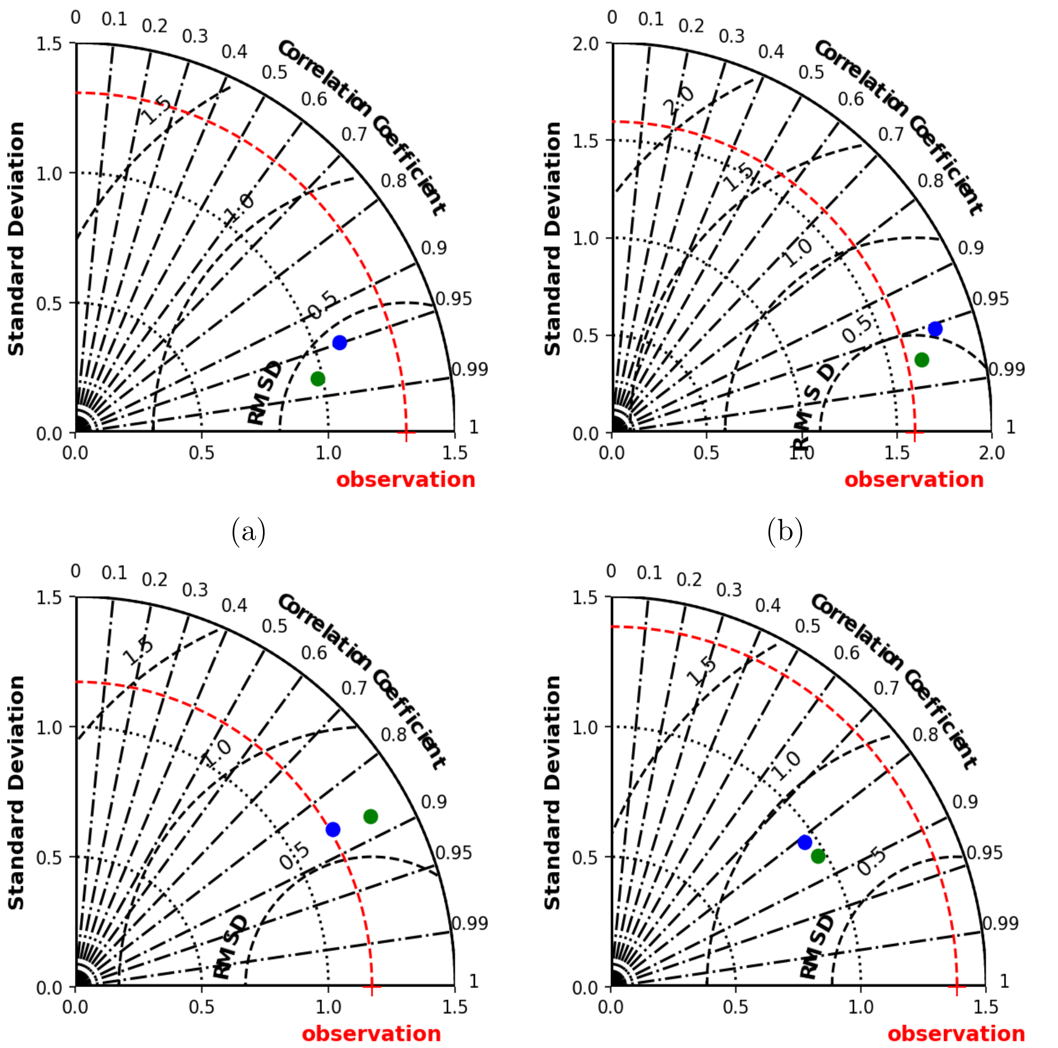

(a) (b)

(c) (d)

FIGURE 6.16: Taylor plots for Typhoon Bavi. WBLM is shown with green dot, Janssen is shown with blue dot, and the in-situ observations with the red cross. Subplot (a) is for buoy 22103, (b) for 22187, (c) for 22191 and (d) for 22192. Records (of each buoy): 169

that for both the correlation coefficient and the RMSE, WBLM resulted in better values (0.97 for CC and 0.40 for RMSE). The corresponding values for Janssen are slightly poorer, with a correlation coefficient of 0.94 and a RMSE of 0.43. WBLM is also better when checking the standard deviation (0.97 versus 1.10 for Janssen). At the same time, the standard deviation of the observations for buoy 22103 is 1.31.

Comparisons with buoy 22187 also showed that in general, the new approach gives better predictions, since the correlation coefficient is 0.97, whereas for Janssen it is 0.95 and the RMSE of WBLM is only 0.37 whilst Janssen's was 0.54. The standard deviation of WBLM is also better (1.67), as Janssen seemed to have greater scatter around the mean with a value of 1.78. In this case, the observational standard deviation was the lowest (1.59).

TABLE 6.4: Comparison of the main performances between Janssen and WBLM of the simulated significant wave height against observations during Typhoon Bavi

Buoy 22103

	Janssen	WBLM
CC	0.94	0.97
RMSE	0.43	0.40
STD obs	1.31	1.31
STD model	1.10	0.97

Buoy 22187

	Janssen	WBLM
CC	0.95	0.97
RMSE	0.54	0.37
STD obs	1.59	1.59
STD model	1.78	1.67

Buoy 22191

	Janssen	WBLM
CC	0.85	0.87
RMSE	0.62	0.65
STD obs	1.07	1.07
STD model	1.11	1.096

Buoy 22192

	Janssen	WBLM
CC	0.81	0.85
RMSE	0.82	0.75
STD obs	1.38	1.38
STD model	0.95	0.97

Correlation coefficients of WBLM with observations from buoy 22191 are again higher (0.87) that for Janssen (0.85). However, in this case RMSE is slightly lower for Janssen (0.62) than for the WBLM (0.65). Standard deviation is again lower for WBLM (about 1.09) than Janssen (1.11). The lowest value of standard deviation was again found in the observations (1.07).

In the last location (buoy 22192), WBLM is again generally better in predicting the significant wave height. The correlation coefficient for WBLM is about 0.85 while for Janssen it is 0.81. Meanwhile, the RMSE for the new approach is 0.75, whereas for Janssen it is 0.82. The WBLM source input gives slightly more scatter around the mean (STD = 0.97) than Janssen (STD = 0.95), while in this case, observations have a quite high standard deviation (1.38)

6.6 Comparisons of Minimum Pressure against Maximum Winds

Figure 6.17 shows the pairs of the maximum 10m wind speed with the corresponding minimum mean sea level pressure (central pressure) of all four tropical cyclones. A comparison with the estimates from the IBTrACS dataset, is performed. This is done for simulation results from both the WBLM source input function (left hand side plot) and the Janssen (reference) source input function (right hand side). Results from all four tropical cyclones and 7 days of forecasts, are shown in Figure 6.17.

Results of the WBLM simulation compared with the corresponding Janssen outputs showed that when the new approach for the source input function is used, the pair of maximum 10m wind speeds and minimum mean sea level pressure is closer to real observations. That is more evident for high wind speeds, of 30m/s and above, with higher corrections as wind speed increases.

6.7 Summary

In this chapter the validation of the WBLM scheme was done by using the available in-situ (ground) observations. In all cyclone cases, results for the

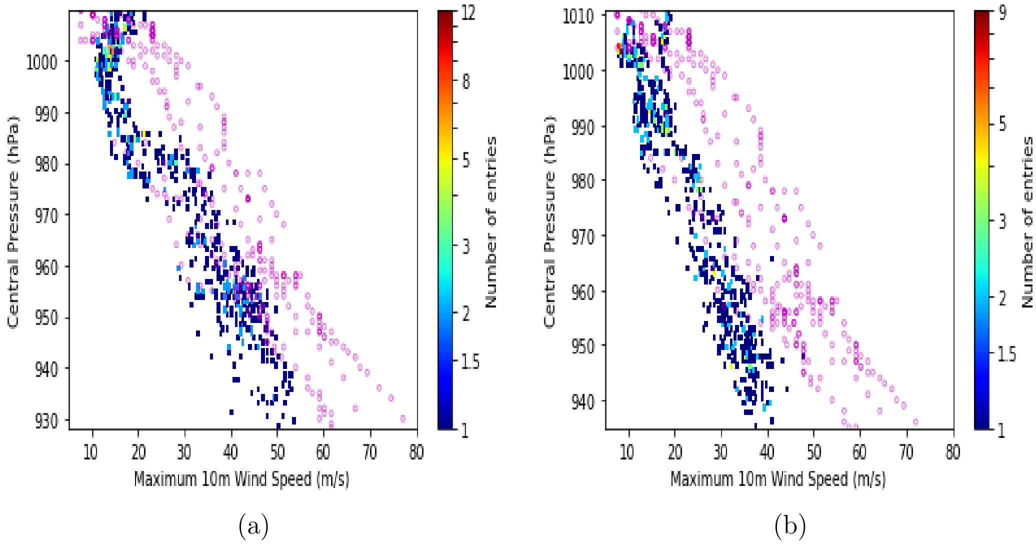

FIGURE 6.17: Correlation of the maximum 10m wind speed and corresponding minimum mean sea level pressure for all 7-days of forecast from all 4 tropical cyclones: (a) WBLM; and (b) Janssen scheme (coloured squares from model results and purple circles for IBTrACS dataset).

runs using the default (Janssen) scheme are also given as a reference. Firstly, trajectory plots showed that both schemes were able to accurately capture the path of the cyclone. In both source input schemes, the trajectories from the models are less reliable compared to the real trajectories, when the cyclone moves towards the land, and we are already a few days into the forecast. Wind speed and significant wave height validation locations from buoys, showed that in some cases WBLM improves the predictions of winds and waves, however there are times that Janssen's scheme better captures the significant wave and wind conditions.

Basic statistical analysis was also presented in this chapter, based on Taylor plots, and its corresponding statistics tables. This analysis showed that in the typhoon cases (Lingling and Bavi) WBLM generally gives more successful predictions of the significant wave height. For the hurricane cases (Dorian and Teddy), in some locations WBLM improves the predictions, while in other points Janssen is more successful, which could be a result from the outliers in drag and Charnock coefficients calculated by WBLM. However, when Janssen gives better predictions, statistics showed that the differences with the WBLM are not large, while there are cases whereas RMSE is significantly lower when the WBLM is used (e.g. buoy 4401 for Dorian). Finally, the standard deviation is lower when the WBLM is used for the simulations, in almost all cases. That means that WBLM has improved the scatter around the mean, which is resulted from the corresponding reduction of scatter in C_d and Charnock coefficient.

Chapter 7

Validation of WBLM with Altimeter Data

7.1 Introduction

This chapter focuses on the validation of the model outputs using the WBLM source input function based on the altimeter data. For comparison, the reference (Janssen parameterisation) run is also shown. For the analysis four satellites were used, namely Jason-3 (J3), Sentinel-3a (S3a), Sentinel-3b (S3b) and CryoSat-2 (C2). Space borne altimeters were primary designed to estimate the sea surface height, helping on the monitoring of the oceans. They also provide observations of significant wave height and wind speed estimates. This chapter presents correlation plots between the model output and the corresponding measurements from the altimeter data, both for the 10m wind speed and the significant wave height. All four tropical cyclone cases are included in this analysis. The analysis focused on the domain of each case study for all seven days of forecast: the North-West Atlantic (90W to40W and 20N to 45N) for the two Hurricane cases, and the Yellow Sea (115E to 140E and 15N to 40N) for the two Typhoons.

In order to better understand the impact of the new approach on the forecast, statistical measurements were also produced and presented here. As the records from the satellites cover a larger area around the storms compared to ground observations from buoys, the statistics analysis using altimeter data could be considered as more reliable. The number of records used are included in the statistics tables. The hurricane cases have higher number of records as the domain (open sea) is bigger, than the area of the Yellow Sea. Furthermore, it is important to acknowledge that the analysis did not include long periods and large domains. The statistical analysis was based on Taylor plots and table of statistical measurements.

7.2 Hurricane Dorian

Correlation plots of the seven days forecast period during hurricane Dorian (02-09/09/2019) are shown in Figure 7.1. The left hand side plot shows the 10m wind speed results, while the right hand side displays the results for the significant wave height. The WBLM scheme is shown with green, the reference run with Janssen's scheme is shown with blue and the identity (1:1) line is also given for reference.

The WBLM initially overestimates the 10m wind speed, until about 6 m/s. The results up to that point are very similar to the reference run. Above that, the scheme constantly underestimates the winds. Higher winds show bigger underestimation. Additionally, the scatter around the best fit was also bigger as 10m wind speed increases. Yet, WBLM is somewhat better than the default parameterisation, and has better agreement with the satellite observations during higher winds. However, WBLM gives some very high values of 35 m/s (outliers) when corresponding satellites measurement were about 25 m/s. For lower wind speeds, below 15 m/s, scatter was less when the WBLM scheme was turned on during the simulations, compared to Janssen's parameterisation scheme. It is important to point out that some differences could be attributed to the thresholds used from the model and the satellites. For the high winds, satellites have a maximum threshold of 30 m/s. However, the model is capable to calculate significantly higher winds than this threshold. Hence, in cases of big differences between the model and the observations, one needs to take this threshold under consideration.

Correlation scatters for the significant wave height (Figure 7.1b) show similar behaviour to the wind speed. It was found that initially, and for waves height up to 2.5 m, simulated values had very good agreement with the records from the satellites. In general, WBLM showed an improvement of the scatter around the mean. With the new approach, values from Janssen, which has previously reached up to 12m/s, were reduced. The highest recorded values from the satellites are about 8m. In general, WBLM gave slightly higher underestimation than Janssen, when was used as source input. However, the best fit lines for both schemes are very close to each other, and generally in very good agreement with the observations.

As mentioned in the introduction of the chapter, the statistical analysis was performed separately for each satellite in order to better understand the findings. In all plots, WBLM is shown with a green dot, while Janssen is shown with a blue dot for reference purposes.

Statistical results for Hurricane Dorian are shown in Figure 7.2 and verified statistics for each satellite are in Table 7.1. It was found that, in general, when using the WBLM results were in very good agreement with the observations from Cryosat-2 (Figure 7.2a). Even though, the default source input function gives slightly better agreement with the satellite observations, the differences with the WBLM outputs are not significant for this station. From the statistics Table (first section of Table 7.1), the correlation coefficient between WBLM and the observations from the satellite was 0.77. That value was slightly smaller than the Janssen's correlation coefficient (0.80). At the same time, the RMSE for WBLM was found higher (by 0.04) than the one of Janssen. Standard deviation

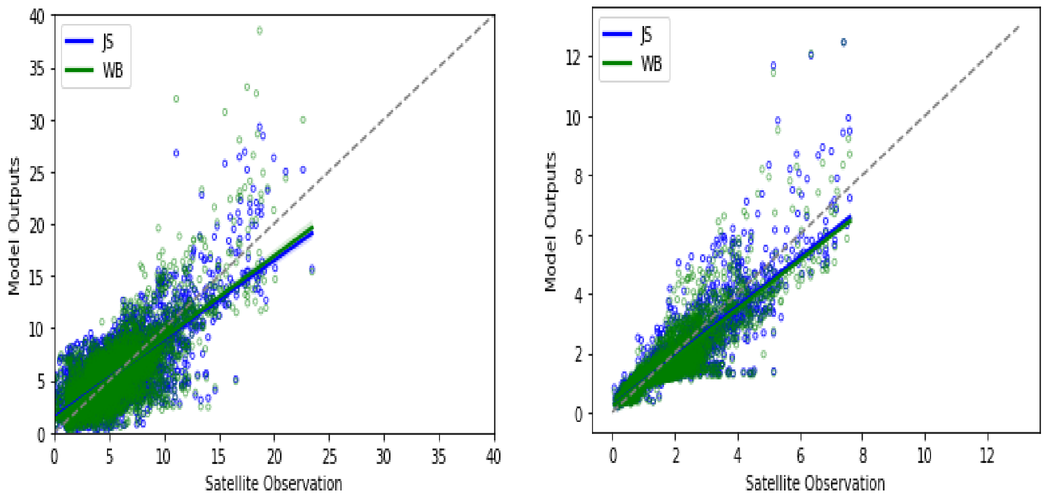

(a) (b)

FIGURE 7.1: Correlation of observations from satellite J3, S3a, S3b, and C2 against model outputs of WBLM (green), for (a) 10m wind speed (m) and (b) significant wave height (m/s) for Hurricane Dorian. The reference run with the default Janssen parameterisation (blue) is also shown. The domain covers from 90W to 40W and from 20N to 45N and the forecasting period is from 02 to 09 of September 2019. The 1:1 identity line (gray dashed line) and best fit lines are also shown on the plot for reference. Note that best fit lines stop where the scatter points (available data) stop.

of the observations was at 0.70, while for the model outputs it is 0.72 and 0.69 for WBLM and Janssen, respectively.

Statistical measures for Jason-3 during the time of hurricane Dorian are shown in Figure 7.2b and the second section of Table 7.1. When shifting to the WBLM scheme, correlation coefficients were almost the same to the default ones, and significantly higher than the one from CryoSat-2 (0.87 for WBLM and 0.88 for Janssen). RMSE for model runs are also somewhat larger than observations, with WBLM reaching 0.50 and Janssen 0.47. In this case, standard deviations are quite large, with the standard deviation of the observations reaching 0.98. That means, that the measurements significantly vary around the mean, which can indicate some mistakes in the observational instrument or variability not captured by the models. For the model results, WBLM had a lower standard deviation (0.96), which was close to the default (Janssen) one (0.94).

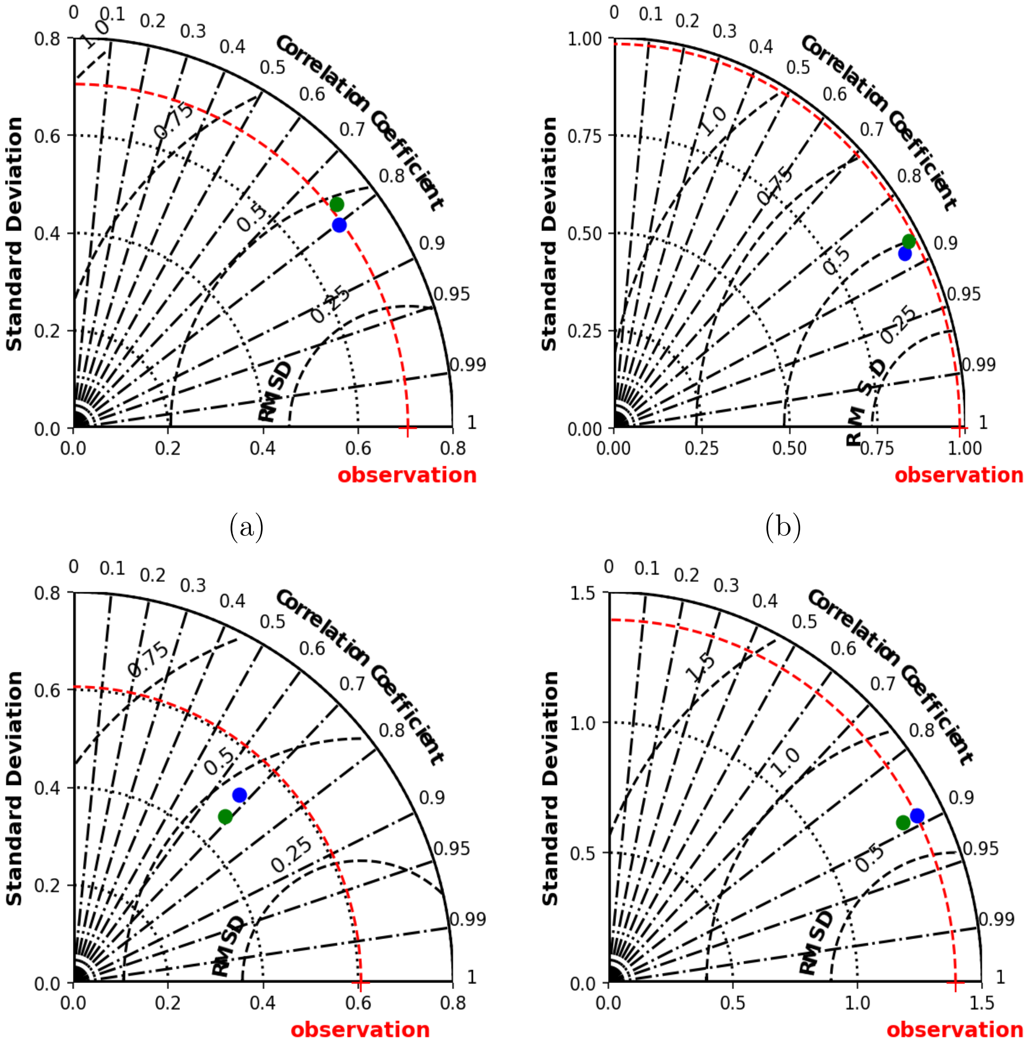

(a) (b)

(c) (d)

FIGURE 7.2: Taylor plots of model significant wave height against satellites observations significant wave height, for Hurricane Dorian. WBLM is shown with green dot, Janssen is shown with blue dot, and the satellite observations with the red cross. (a) is for CryoSat-2, (b) for Jasson-3, (c) for Sentinel-3a and (d) for Sentinel-3b

Observations from Sentinel - 3a are given in Figure 7.2c and the third section of Table 7.1. Results showed that the WBLM correlation coefficient was 0.79. That was slightly lower than the reference's run correlation coefficient. A slightly increased RMSE of about 0.03 was also found. Standard deviations were again generally low, which means there is not big variation around the mean. Again, observations had the highest STD (0.66), while WBLM had significantly lower STD (0.55). However, also in this case STD is also slightly increased compared to the reference run, whose STD was 0.49.

Comparisons with the last validation altimeter data of Sentinel-3b are given in Figure 7.2d and the last section of Table 7.1. The statistical analysis for this station showed that WBLM generally has improved the predictions. Even though the correlation coefficient is the same with the reference run (0.89), the RMSE has decreased (from 0.66 to 0.65). In addition, the standard deviation has significantly been reduced compared to the default runs (from 1.39 to 1.33). The observational standard deviation was also high with a value of 1.39, which means that the observations are scattered around the mean, which can indicate natural variability or instrumental mistakes.

7.3 Hurricane Teddy

The wind speed correlation plot for the prediction period of hurricane Teddy (19-26/09/2020), and the domain of interest is shown in Figure 7.3a. Results revealed that the model overestimated the wind speeds until about 10 m/s. Around 10 m/s the observations met the identity (gray dashed) line, agreeing with the observations. After that there is a constant underestimation of the surface wind speeds. In this case, WBLM is very close to the values taken from the default (Janssen) runs. Compared to Hurricane Dorian the underestimations for this case were smaller. Again, the WBLM (green) gives some very high predictions around 35 m/s. Due to the maximum threshold of the satellite measurements (30 m/s), the altimeter would not be able to capture, even if they were true.

The significant wave height correlation plot is shown in Figure 7.3b. Again, results showed that up to 2.5m WBLM agreed very well with the records from the satellites. Above this height, WBLM underestimates. This underestimation is to some degree higher than the default model. That means that, for this case study, Janssen's scheme (blue) is somewhat closer to the satellite predictions

TABLE 7.1: Comparison of the main performances between Janssen and WBLM of the simulated significant wave height against observations during Hurricane Dorian

CryoSat-2 (Records: 1338)

	Janssen	WBLM
CC	0.80	0.77
RMSE	0.44	0.48
STD obs	0.70	0.70
STD model	0.69	0.72

Jasson-3 (Records: 1361)

	Janssen	WBLM
CC	0.88	0.87
RMSE	0.47	0.50
STD obs	0.98	0.98
STD model	0.94	0.96

Sentinel-3a (Records: 1309)

	Janssen	WBLM
CC	0.84	0.79
RMSE	0.36	0.41
STD obs	0.66	0.66
STD model	0.49	0.55

Sentinel-3b (Records: 1320)

	Janssen	WBLM
CC	0.89	0.89
RMSE	0.66	0.65
STD obs	1.39	1.39
STD model	1.39	1.33

(closer to the identity dashed gray line). Again, some outliers from WBLM (green) reached even above the 12m wave height, while the corresponding observational height was around 6m.

Similarly to hurricane Dorian, in this study, basic statistical analysis to a possible extent is presented using Taylor plots (Figure 7.4 and statistical Table 7.2).

The statistical analysis of the model outputs with satellite observations from CryoSat-2 is given in Figure 7.4a and the first section of statistics Table 7.2.

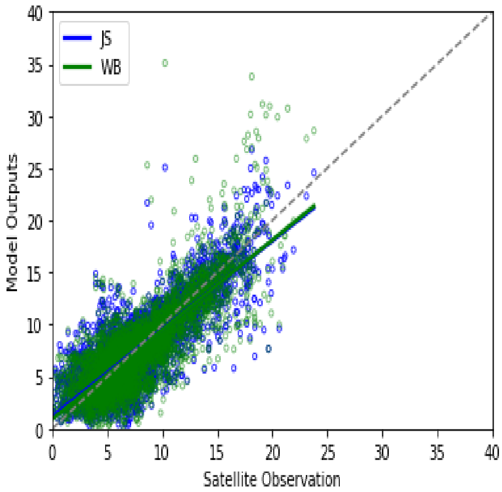

(a)

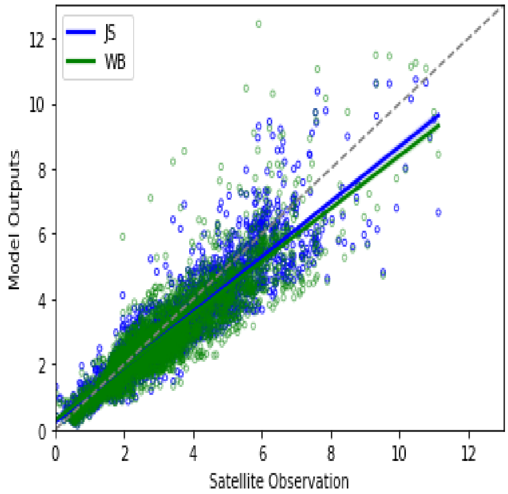

(b)

FIGURE 7.3: Correlation of observations from satellite J3, S3a, S3b, and C2 against model outputs of WBLM (green), for (a) 10m wind speed (m) and (b) significant wave height (m/s) for Hurricane Teddy. Reference run with the default from Janssen's parameterisation (blue) is also shown. The domain covers from 90W to 40W and from 20N to 45N and the forecasting period is from 19 to 26 of September 2020. The 1:1 identity line (gray dashed line) and best fit lines are also shown on the plot for reference. Note that best fit lines stop where the scatter points (available data) stop.

Results showed that overall the WBLM scheme had high correlation with the satellite records. However, it is somewhat reduced compared to the default runs, as WBLM gave a CC of 0.82 compared to 0.89 from default scheme simulations. Similarly, the RMSE was increased, with WBLM giving a value of 0.67, compared to a value of 0.54 when using the default source input. Standard deviations from the two model runs and the satellite observations were found to be high. This means, that values significantly vary around the mean. For observations the standard deviation was found to reach the values of 1.20. At the same time, for the simulations the standard deviation was 1.09 for Janssen and 1.05 for WBLM. Nonetheless, this indicates once again that there was an improvement of the standard deviation when WBLM is used therefore showing that when using the new approach, there was improvement of the scatter around the mean.

Comparisons of the model results with observations from Jason-3, are displayed in Figure 7.4b and the second section Table 7.4. Results showed that outputs from WBLM had good agreement with the observations. Furthermore, they were very similar to the reference simulations using the default source input function. The correlation coefficient between satellite records and the WBLM is high (0.93). RMSE was 0.57 marginally higher than the default results (0.53). In addition, as in the previous case, standard deviations were generally high. The observational standard deviation was about 1.58. For WBLM the same measure was close to 1.36. This was again improved compared to default run's standard deviation (1.39).

Corresponding results for Sentinel-3a are given in Figure 7.4c and the third section of Table 7.2. The statistical analysis showed that the correlation coefficient for WBLM, even though it was lower than the one of Janssen (0.92 for Janssen and 0.90 for WBLM), gave very good agreement with the satellite observations. The RMSE in this case was also higher when WBLM was used for the predictions of the wave height (0.71 for WBLM and 0.60 for Janssen). For the standard deviation, also in this case study, some high values were captured. For the observations, the standard deviation was about 1.57, whereas for the model simulations, this metric was lower, although still considered high. The standard deviation was found to be about 1.53 for the WBLM, while Janssen showed the lowest value (1.49).

Finally, statistical results from Sentinel-3b and simulations outputs are found in Figure 7.4d and the last section of Table 7.2. The statistical analysis for this case showed similar findings to the rest of satellites analysis. The correlation coefficient was again lower when WBLM was used compared to Janssen's scheme outputs (0.92 for Janssen and 0.85 for WBLM). RMSE was also higher when the WBLM is used as source input (0.53 for Janssen and 0.69 for WBLM). Additionally, also in this case the standard deviations were quite high for both

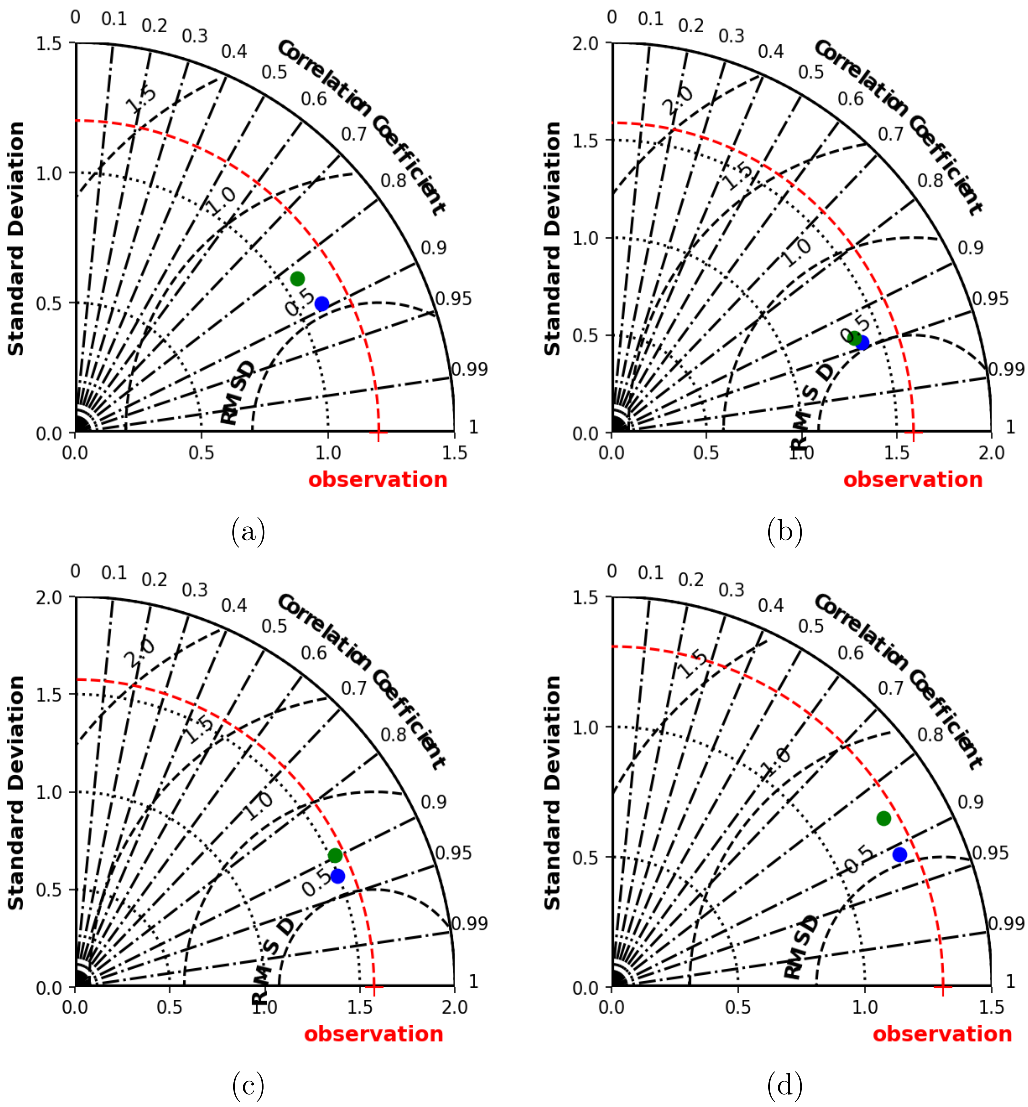

Figure 7.4: Taylor plots of model significant wave height against satellites observations significant wave height, for Hurricane Teddy. WBLM is shown with green dot, Janssen is shown with blue dot, and the satellite observations with the red cross. (a) is for CryoSat-2, (b) for Jasson-3, (c) for Sentinel-3a and (d) for Sentinel-3b

source input schemes and the observations. Observations gave the highest value (1.30), while WBLM and Janssen had very similar values (1.25 and 1.24 respectively).

Table 7.2: Main statistics, namely Correlation Coefficient (CC), RMSE, Standard deviation of observations (STD obs), standard deviation of model (STD model), for simulated against satellite observed significant wave height for Hurricane Teddy

CryoSat-2 (Records: 1336)

	Janssen	WBLM
CC	0.89	0.82
RMSE	0.54	0.67
STD obs	1.20	1.20
STD model	1.09	1.05

Jasson-3 (Records: 1381)

	Janssen	WBLM
CC	0.94	0.93
RMSE	0.53	0.57
STD obs	1.58	1.58
STD model	1.39	1.36

Sentinel-3a (Records: 1288)

	Janssen	WBLM
CC	0.92	0.90
RMSE	0.60	0.71
STD obs	1.57	1.57
STD model	1.49	1.53

Sentinel-3b (Records: 1276)

	Janssen	WBLM
CC	0.92	0.85
RMSE	0.53	0.69
STD obs	1.30	1.30
STD model	1.24	1.25

7.4 Typhoon Lingling

Correlation plots between model simulations and the satellite observations for typhoon Lingling's forecasting period (04-11/09/2019) are shown in Figure 7.5. Results indicated that for model simulations the same trend as in the hurricane cases is followed. For 10 m wind speed (Figure 7.5a) results from the WBLM source input function overestimate the observations up to 10 m/s. However, there is a somewhat improvement compared to the output from the reference run with Janssen's scheme. After that, there is a very small underestimation, where outputs from the WBLM and the default source input functions gave very similar results. The scatter around the mean both for model runs and observations, compared to previous cases is reduced. Only a number of values reached of about 27m/s wind speeds. Again, this could be linked to the maximum threshold of 30 m/s for the satellite stations, and the calibration of instruments.

For the significant wave height (Figure 7.5b), there is a significant underestimation of the high waves when the WBLM is used. This corresponds with the biggest difference with the default scheme; however, upon close inspection, the scatter in the upper part of the 1:1 identity line is larger when Janssen's scheme is used. This means, that of course, the best fit line of the default scheme will balance, higher than the WBLM one. However, as the results vary significantly around the mean, it does not mean that Janssen's scheme is actually the correct one. For lower waves, up to 2m, the model has very good agreement with the observations from the satellites.

Similarly to the hurricane cases, basic statistical analysis for the significant wave height is done using Taylor plots (Figure 7.6) and tables of statistics (Table 7.3).

Comparing observations taken for the forecasting period and for the domain of interest of Typhoon Lingling, results for satellite CryoSat-2 are shown in Figure 7.6a. It is found that WBLM predictions are very close to the observations, since the correlation coefficient is high (0.93) and the RMSE low (0.36). The correlation coefficient for WBLM is also slightly higher than the one of the reference run (0.93), whereas the RMSE is slightly lower for the default source input function scheme (0.32). The standard deviations had sensible values with the highest magnitude found in the observations (0.79), and the lowest value (0.51) for WBLM .

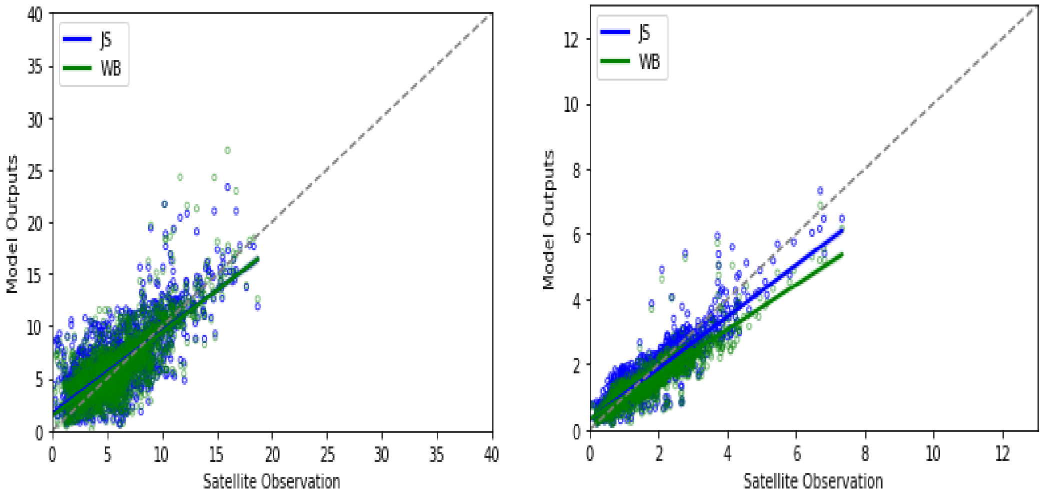

(a) (b)

FIGURE 7.5: Correlation of observations from satellite J3, S3a, S3b, and C2 against model outputs of WBLM (green), for (a) 10m wind speed (m) and (b) significant wave height (m/s) of Typhoon Lingling. Reference run with the default from the Janssen parameterisation (blue) is also shown. The domain covers from 115E to 140E and 15N to 40N and the forecasting period is 04 to 11 of September 2019. The 1:1 identity line (gray dashed line) and best fit lines are also shown on the plot for reference. Note that best fit lines stop where the scatter points (available data) stop.

Comparisons of simulated significant wave height with observations from Jason-3 give similar findings (Figure 7.6 upper right corner). The correlation coefficient of WBLM with the satellite observations is high (0.90) and equal to the one of the reference run. The RMSE is very low for WBLM source input function (0.37). Standard deviations are fairly higher than the values taken from CryoSat-2. Observations give a standard deviation of 0.89, while the WBLM source input scheme significantly improved the standard deviation when it is used (0.76 for WBLM and 0.87 for Janssen).

Analogous results are found from the comparison of the model results with Sentinel-3a (Figure 7.6 bottom left corner). The correlation coefficient of the model output with the observations is again high, with correlation coefficient of the WBLM with Sentinel-3a reaching 0.81. Similarly, the RMSE is low, giving a value of 0.41. This value is also improved compared to the default

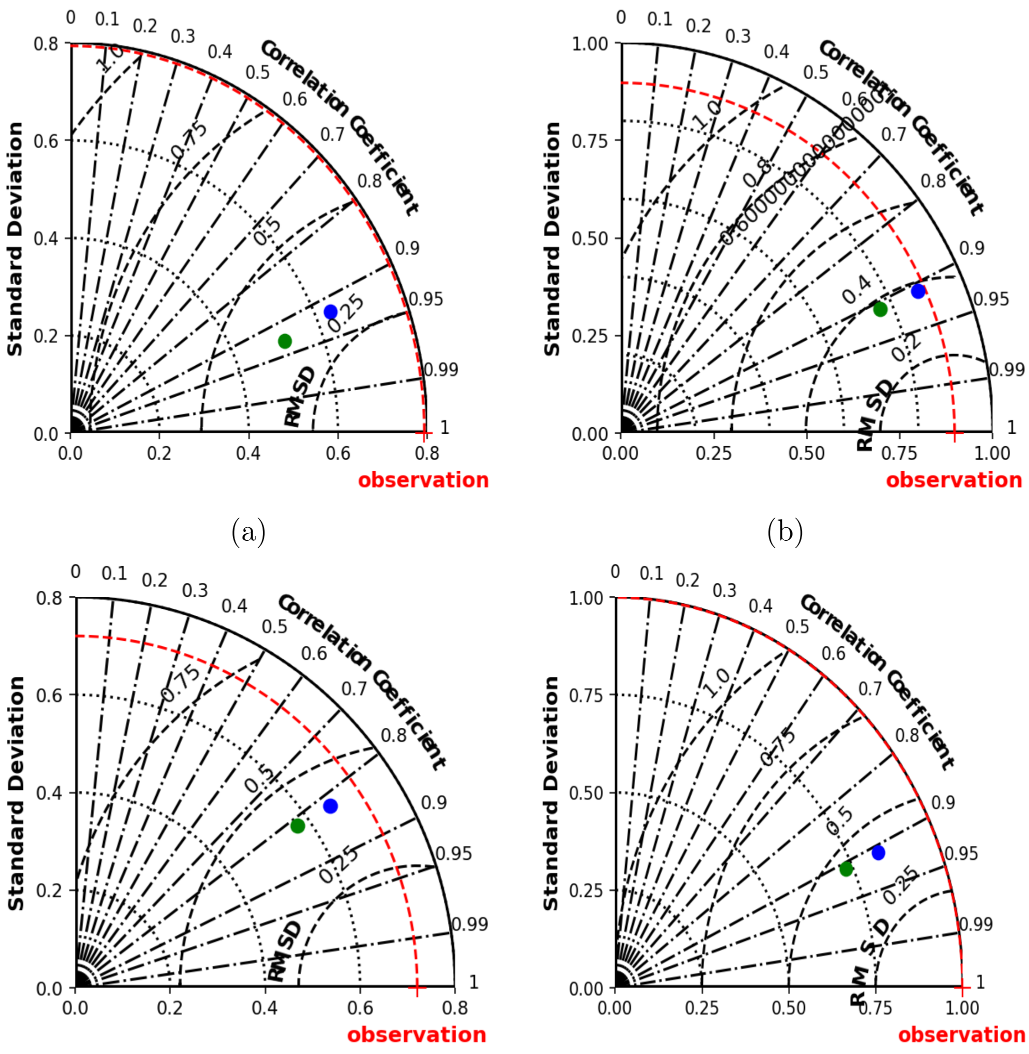

(a) (b) (c) (d)

FIGURE 7.6: Taylor plots of model significant wave height against satellites observations significant wave height, for Typhoon Lingling. WBLM is shown with green dot, Janssen is shown with blue dot, and the satellite observations with the red cross. (a) is for CryoSat-2, (b) for Jasson-3, (c) for Sentinel-3a and (d) for Sentinel-3b

parameterisation predictions. Hence, the model is in good agreement with the observations. For the standard deviations, the value calculated for WBLM is the lowest (0.57), and improved compared to the reference run. The observations have the highest standard deviation (0.72), which is still low.

Finally, Sentinel-3b observations gave again a very good correlation coefficient with WBLM (0.91). RMS errors of the WBLM output is again quite low (about 0.45). Here, the standard deviation of the observation was 0.99, while WBLM has again the lower value (0.73), which is once again highly improved compared to the default scheme (0.83).

Table 7.3: Main statistics, namely Correlation Coefficient (CC), RMSE, Standard deviation of observations (STD obs), standard deviation of model (STD model), for simulated against satellite observed significant wave height for Typhoon Lingling

	CryoSat-2 (Records: 477)	
	Janssen	WBLM
CC	0.92	0.93
RMSE	0.32	0.36
STD obs	0.79	0.79
STD model	0.63	0.51

	Jasson-3 (Records: 621)	
	Janssen	WBLM
CC	0.89	0.90
RMSE	0.37	0.37
STD obs	0.89	0.89
STD model	0.88	0.76

	Sentinel-3a (Records: 622)	
	Janssen	WBLM
CC	0.82	0.81
RMSE	0.41	0.42
STD obs	0.72	0.72
STD model	0.65	0.57

	Sentinel-3b (Records: 583)	
	Janssen	WBLM
CC	0.91	0.91
RMSE	0.42	0.45
STD obs	0.99	0.99
STD model	0.83	0.73

7.5 Typhoon Bavi

For the case of typhoon Bavi, the plots for the comparisons of the simulations with observations from the satellites are given in Figure 7.7. The plots are for the forecasting period of interest for typhoon Bavi (24-31/09/2020) and for the domain in which the cyclone occurred.

The correlation plot for the 10 m wind speed is given in Figure 7.7a. Results showed that outputs using any of the two source input functions were very close to each other and the observations. In general, the simulated surface winds are close to the satellite observations, since the prediction best fit lines are close to the identity line (gray dashed line). However, in this case, there is again a big spread of scatter around the mean, including some outliers. For example, there are some values of 10m wind speed around 40 m/s when the WBLM is used. At the same time, the corresponding satellite records are about 20 m/s. Again, one needs to keep in mind that the maximum threshold of the altimeter data is 30 m/s, and can play a significant role on the differences between the observations and the simulations. However, these values could also be outliers.

For the same forecasting period, the correlation plot for the significant wave height (Figure 7.7b) shows that both schemes started with an underestimation of the smaller wave heights (bellow 2 m). In this case, Janssen's scheme (blue) is somewhat closer to the 1:1 line (identity line). This could mean that the default scheme agrees better with the satellite observations compared to WBLM (green). However, once again the scatter around the mean in the upper part of the best fit line is higher for Janssen compared to the WBLM scheme results.

As in all previous cyclone studies, basic statistics were calculated for each satellite against model simulations for the significant wave height. The results are given in Figure 7.8 and Table 7.4. Comparisons of the results from the model simulations for the significant wave height with the observations from satellite CryoSat-2 are given in Figure 7.8a and the first section of Table 7.4. Results showed that WBLM improved the predictions of the Cryosat-2 measurements, as both the correlation coefficient and RMSE is improved when the new approach is used. The correlation coefficient for WBLM is 0.64 compared to 0.62

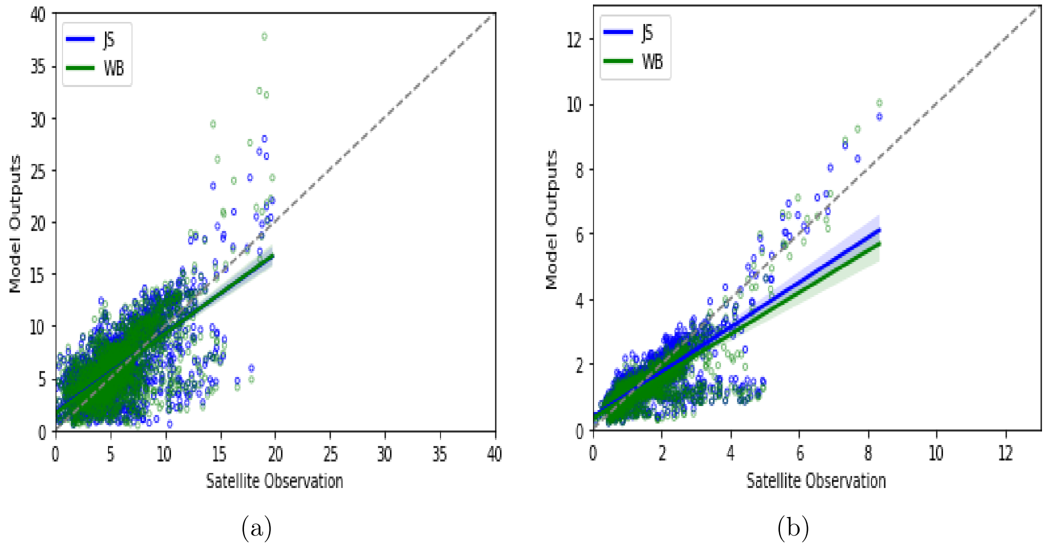

FIGURE 7.7: Correlation of observations from satellite J3, S3a, S3b, and C2 against model outputs of WBLM (green), for (a) 10m wind speed (m) and (b) significant wave height (m/s) for Typhoon Bavi. Reference run with the default from Janssen parameterisation (blue) is also shown. The domain covers from 115E to 140E and from 15N to 40N and the forecasting period is from 24 to 31 August 2020. The 1:1 identity line (gray dashed line) and best fit lines are also shown on the plot for reference. Note that best fit lines stop where the scatter points (available data) stop.

from the reference run. At the same time, RMSE of WBLM is 0.62 compared to 0.63 for the default parameterisation. The standard deviation of the simulated results is reduced when WBLM is used around 0.06. That means that when WBLM is used, the scatter around mean is reduced. The corresponding observational standard deviation is 0.80.

Statistics of the comparisons of the simulated significant wave height compared to observations of satellite Jason-3 are given in Figure 7.8b and the second section of Table 7.4. Again, the correlation with observations from Jason-3 showed that when WBLM is used predictions of the significant wave height were very close to the observations. The correlation coefficient was slightly reduced when the WBLM was used (to 0.90 from 0.91). For the RMSE, the WBLM simulations gave again similar values to the reference run but slightly larger (0.55 versus 0.53). Once more, the standard deviations were high. The observational standard deviation was about 1.24, the standard deviation of the WBLM source input function was 1.93. In this case, the reference run gave a better standard deviation of 1.22.

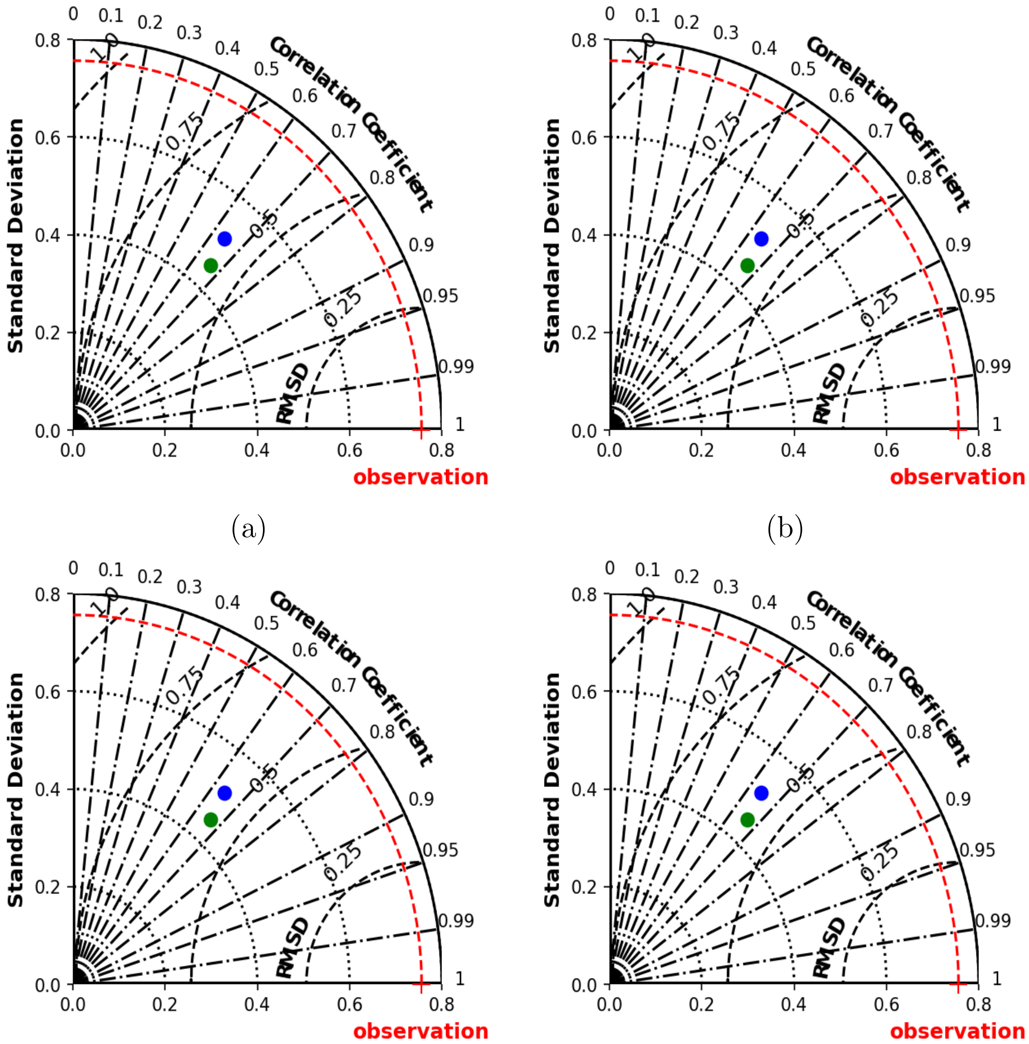

(a) (b) (c) (d)

FIGURE 7.8: Taylor plots of model significant wave height against satellites observations significant wave height, for Typhoon Bavi. WBLM is shown with green dot, Janssen is shown with blue dot, and the satellite observations with the red cross. (a) is for CryoSat-2, (b) for Jasson-3, (c) for Sentinel-3a and (d) for Sentinel-3b

Sentinel-3a results for the significant wave height are given in Figure 7.8c and the third section of Table 7.4. The correlation coefficient is slightly improved when the WBLM source input function is used compared to the reference run

(0.69 and 0.68 respectively). RMSE was again improved when the new approach was turned on, from 0.46 for Janssen's scheme to 0.44 for the WBLM. The means the WBLM predictions were closer to the observations of Sentinel-3a compared to the results from Janssen's scheme. In addition, the standard deviations calculated for Sentinel-3a were in a good scale (0.61). The standard deviation for the model outputs of WBLM holds the lowest value (0.48), which is highly improved compared to the default parameterisation (0.53). These results indicate that the observations can be considered to be reliable and that the values for the WBLM are close to the mean values.

Finally, results from the comparison of model simulations of significant wave height against observations from Sentinel-3b are given in Figure 7.8d and the last section of Table 7.4. Results showed that the simulations gave good correlation to the satellite observations (0.65). The RMSE for WBLM is quite high (0.77). In this case, the standard deviation is also high, with the observational standard deviation to be 0.99. However, the standard deviation of the WBLM showed a big improvement compared to the reference run.

7.6 Summary

In this chapter the validation of the model simulations for the 10m wind speed and the significant wave height based on altimeter data was presented. The altimeter data used were obtained from four different satellites, namely CryoSat-2, Jason-3, Sentinel-3a and Sentinel-3b.

The analysis was based on correlation (scatter) plots of the model results for both parameters (wind speed and significant wave height) against the observations (Figures 7.1,7.3,7.5,7.7) . The plots presented both the WBLM (green) and the default Janssen (blue) source input functions, in order to have the default parameterisation as reference. Moreover, basic statistical analysis was made, using Taylor plots (Figures 7.2, 7.4, 7.6, 7.8) and Tables with statistics

Table 7.4: Main statistics,namely Correlation Coefficient (CC), RMSE, Standard deviation of observations (STD obs), standard deviation of model (STD model), for simulated against satellite observed significant wave height for Typhoon Bavi

CryoSat-2 (Records: 502)		
	Janssen	WBLM
CC	0.62	0.64
RMSE	0.63	0.62
STD obs	0.80	0.80
STD model	0.53	0.47

Jasson-3 (Records: 583)		
	Janssen	WBLM
CC	0.91	0.90
RMSE	0.53	0.55
STD obs	1.24	1.24
STD model	1.22	1.93

Sentinel-3a (Records: 614)		
	Janssen	WBLM
CC	0.68	0.69
RMSE	0.46	0.44
STD obs	0.61	0.61
STD model	0.53	0.48

Sentinel-3b (Records: 564)		
	Janssen	WBLM
CC	0.67	0.65
RMSE	0.76	0.77
STD obs	0.99	0.99
STD model	0.84	0.77

(Tables 7.1 to 7.4).

In general, results from the scatter plots showed that there was an underestimation of both the significant wave height and the wind speed for all case studies. In addition, there were cases (Hurricane Teddy) where Janssen's scheme has better captured the cyclones, whereas in other cases WBLM was more successful.

The above mixed behaviour of the two schemes was also supported by the statistical analysis, since in some cases correlation coefficients and RMSEs for wave heights indicated a better representation when the WBLM source input scheme was used, whereas in other cases Janssen's scheme provided better agreement. Finally, it was found that for most cases, WBLM constantly gives lower standard deviations from the default parameterisation. That means that WBLM reduces the scatter around the mean. Observations always have the highest standard deviation, even if the the data has passed quality control. This is expected since some measurements can significantly differ from the mean. In general, the Hurricane Teddy case study and Jasson-3 were found to give quite high standard deviations. More specifically, hurricane Teddy is one of the most difficult case studies since the high standard deviations do not allows drawing clear conclusions. That means that one must be cautious when the results vary significantly around mean (best fit), as outliers can work in such a way to falsely improve the total forecast.

Chapter 8

Synthesis and Conclusions

8.1 Discussion

The Wave Boundary Model (WBLM) has been previously used in wave studies in order to theoretically approach the parameterisation of the surface stresses through the drag coefficient (C_d) and roughness length (z_0) (e.g. Hara and Belcher (2002); Moon et al. (2004)). However, only recently the WBLM was used in order to explicitly calculate the wind profile and the turbulent and wave stresses in each height (Du et al., 2017, 2019). Hence, this approach is used to directly calculate the S_{in}. However, the WBLM as used in this approach was developed in a stand-alone wave model (SWAN). Since the importance of coupled models has been highlighted by many studies (Janssen, 1991; ECMWF, 2020; Gentile et al., 2021), in this PhD project the scheme was implemented and tested in a coupled forecasting system (OpenIFS), where a coupler is not required, and errors during the passage of the stresses between the sea and the atmosphere are avoided.

It has been seen by many studies that the right choice of Miles parameter, C_β, can highly impact the calculation of the drag coefficient and the source input function (C_d, S_{in}) through wave growth, given by Equation 3.26. Different studies have worked out different values of C_β. For example, Hara and Belcher (2002) used a $C_\beta = 40$; Moon et al. (2004) found a value of $C_\beta = 32$, while Chen and Yu (2016) gave a $C_\beta = 25$. However, the WBLM follows the calculation of 3.27 from Janssen (1991), where the Miles parameter is explicitly calculated, using a constant $\beta_{max} = 1.6$. This is used in the wave part of OpenIFS (ECWAM) and it was adjusted from $\beta_{max} = 1.2$ in earlier versions of the model (ECMWF (2020)), which as a result controls the C_d.

In addition, in order for the scheme to correctly work in a coupled model, in this study we corrected the roughness length parameterisation. The bulk parameterisation of z_0 used by Du et al. (2019) (equation 3.47) was replaced by the wave induced parameterisation (equation 3.48) found by Janssen (1991).

Furthermore, the scheme successfully takes into consideration the sheltering mechanism suggested by previous studies Ardhuin et al. (2010); Babanin et al. (2010).

This approach was successful in controlling and reducing the drag coefficient for high wind speeds when the WBLM is used. It even yielded C_d reduction of 0.002 for the extreme winds under tropical cyclone conditions. These results are in very good agreement with recent studies in literature and operational models (e.g. ECMWF, 2020; Li et al., 2021; Valiente et al., 2021). In addition, even though there were not many entries in extreme winds, the drag coefficient saturation above 35m/s is also shown here, and agrees well with the literature (e.g. Donelan et al., 2004; Curcic and Haus, 2020). As shown from Pineau-Guillou et al. (2018), correction of the Charnock parameter reduces its magnitude. The WBLM also showed these reductions of the Charnock parameter following its impact on the wind input source term, and in turn on the wave induced stress. Furthermore, a reduction of the scatter around the mean is also found, reducing the variance around the mean values.

As found by Pineau-Guillou et al. (2018) for mid-latitude storms, a larger Charnock parameter generally results in a higher roughness length, which leads to a higher drag coefficient, and therefore higher wind stress and as a result lower wind speed. However, they show that when the Charnock parameter is lower results show higher wind speeds and a lower central pressure of the storm. In their study for typhoon conditions Li et al. (2021), when testing a new roughness length parameterisation based on the recent update to ECWAM (ECMWF, 2020; Bidlot et al., 2020) showed that winds are generally higher around the typhoon, in comparison to results from the old parameterisation. Here, similar results are found. For wind predictions under mid-latitude storms and tropical cyclones when the WBLM is used there is a general increase, after the correction of the overestimated wind stress of Janssen (1991). Higher wind speeds are shown in all the study cases, and bigger differences were found near the centre of the cyclone. Specifically, for typhoon Lingling, which is used here and in Li et al. (2021) with results yield very similar findings. The significant wave height is in good agreement with results found in Li et al. (2021), with a general decrease of the wave heights when the parameterisation for a reduced drag coefficient is used. In addition, comparisons of the tropical cyclones' maximum wind speed and corresponding minimum mean sea level pressure, gave improved predictions with the WBLM method, with better agreement with the best track measurements. This is also in agreement with other studies, such as the new parameterisation used in the operational model of ECMWF (Bidlot et al., 2020).

In this study, the validation was performed with in-situ observations from buoys as well as altimeter (satellite) data. For the validation with the buoy data it is shown that for most of the tropical cyclones cases, when WBLM is used the predictions of the significant wave height are better than the ones from the default parameterisation. In the cases where the model does not agree well with the predictions, there is a general overestimation of the waves from the model simulations, mainly at the peak of the cyclone. However, studies have discussed the issues that buoy data may suffer during extreme events (e.g. Zabolotskikh et al., 2013). In this study, buoys used for the validation of the model are moored in a single point system. That allows the wave buoys to match conditions of wind and wave. However, buoys have been found to have problems in recording large short-crested waves, since buoys may move around the wave and hence misscapturing it (Liu et al., 2015). In addition and more importantly, mistakes are also linked to timing issues as the simulations move further into the forecast. Closer inspection would show the connection of these mistakes to the along track errors which result to the cyclone in the model and in reality to not be entirely in phase (ECMWF, 2021). For these reasons, the model often gives higher predictions than the observations, but they are closer to real wave heights. In addition to this, difficulties also arise due to the availability of the validation data from buoys. There are cases, such as the two typhoons and Hurricane Teddy, where limited data were available, since there were not many buoys in the cyclones' path. Hence, data availability constrains the analysis of the simulation results.

Another issue in correctly capturing the cyclone is related to the issues that the models face during the so-called re-intensification of the cyclones. Specifically, for the North Atlantic it has been found that around 45% of tropical cyclones interact with the mid-latitude flow after re-curvature and they undergo extratropical transition, with more than 50% of these storms re-intensifying as extratropical cyclones (Xiande et al., 2018). Currently, more studies try to focus in this area (e.g. Ryglicki et al., 2019).

In order to improve domain coverage, satellite altimeter data were used. Satellite ground tracks of the satellites when combined together can cover almost the whole globe in any time required. Four satellites were used (CryoSat-2, Jason-3, Sentinel-3a and Sentinel-3b) in order to overcome the issue of data availability from buoys. Results from the analysis of the altimeter data lead to similar findings to the analysis of the buoy observations. Again, the scatter around the mean has been significantly reduced in most cases when the WBLM is used, while in cases the observations showed better agreement with the simulations from the new approach (e.g. Hurricane Bavi and Sentinel-3 7.4).

Nonetheless, there are still cases for which Janssen's scheme was more successful in capturing the cyclones (e.g. Hurricane Dorian and CryoSat-2 7.1) However, the abilities and calibration of the instrument can also give incorrect recordings. For example, the limit of the wind speeds for the satellites is 30m/s, while the model can calculate significantly higher speeds than this. In addition, in reality wind speeds can also be significantly higher than these values. Studies have tried to work out the reliability of the satellites (Yang et al., 2020). Wind speeds compared with buoy data and Advanced Scatterometer (ASCAT) data showed that in general Sentinel-3a and Sentinel-3b wind speeds have been found to be more accurate compared to Jason-3. At the same time, significant wave heights from Jason-3 are accurate records, compared to the two Sentinels. Moreover, measurements of satellite CryoSat-2 validated with observations from the numerical model results of the ECMWF, as well as measurements by buoys showed that its records are in good agreement with the in-situ observations Yang et al. (2020). However, even the ASCAT data used in Yang et al. (2020) study as reference point, have been found in other studies to underestimate the wind speeds (Pineau-Guillou et al. (2018)).

For the present study results also showed the importance of the quality of the observations, since statistical analysis can not easily conclude on the best scheme, out of the two used here. In addition, for different areas and cases satellite records give lower variability, with Sentinel-3b being give high STDs while Sentinel-3a is usually the most stable in the scatter around the mean.

All the above, in addition to the known errors from buoys, can only conclude to the fact that no observations can be fully trusted. That means deeper investigations are still needed in order to understand the quality of the in-situ, as well as the altimeter, wind and wave measurements. More datasets are required in order to calibrate the remote-sensing conditions, especially under extreme conditions.

Furthermore, another point that must be taken into consideration when analysing the results, is the resolution of the model. The resolution used in this study, is the highest possible for OpenIFS (TL1279 (16km) for the atmospheric model and 0.25 degrees (28km) for the wave model). However, particularly for the typhoon case studies, for which a big part of their path is in a closed sea (Yellow Sea), the resolution could cause errors in the simulations. The spatial resolution may miss differences in depth as well as sea conditions, and generally underestimate the strong gradients that exist in and around these storms. For this reason current studies and operational models use higher resolution than the ones used here. For example ECMWF's operational model has a 9km spatial resolution for the atmospheric part and 0.1 degrees for the wave part of the model (ECMWF, 2020).

Finally, the source input function presented here, has been found to require high computational time. This chapter presents the idea and analysis of the final changes that are required in order to reduce the computational cost of the Wave Boundary Layer Model (WBLM).

New approaches and parameterisation schemes, in order to be used in operational forecast models, need to fulfill two requirements: 1) the scheme needs to give results in the correct order of magnitude and 2) needs to agree well with observations. Furthermore, if this model shows better accuracy, but is very expensive computationally, it will not work for operational purposes as centres need to give the predictions on time.

8.2 Future Work: Reduction of Computational Cost of WBLM source input function

One of the most important aspects that were checked during the analysis was the computational cost of the new scheme. More specifically, the computational time of the new source input function parameterisation approach.

For all runs 144 number of processors were used. This number was chosen based on the resolution of the model, as well as for reducing the time of the run. However, by checking the time required for the model to run when the WBLM is switched on, in comparison to the reference runs from Janssen, it was found that the new scheme requires about two and a half to three (2.5-3) hours more in order to complete a run (Table 8.1).

TABLE 8.1: Computational Time for the different case studies. Comparisons of WBLM and Janssen

	Janssen	WBLM
Ciara	03:36:48	05:57:10
Dorian	06:07:53	09:00:19
Teddy	06:12:27	09:02:30
Lingling	06:14:23	09:00:04
Bavi	06:14:06	09:38:45

In order to compute the stresses and wind profile for the high frequencies (i.e. above maximum frequency of the model), the WBLM scheme artificially extends the number and maximum value of the wave model frequencies. More analytically, in equation 3.44 the first two parts are resolved using the discretised spectrum, from minimum to maximum frequencies (σ_{min} to σ_{max}). However, the last (viscous) part of the wind profile (and therefore the equation) requires the frequencies above σ_{max}.

Since $\vec{\tau}_v$ is defined as $\vec{\tau}_t(z)$, $\vec{\tau}_v$ is expressed as:

$$\vec{\tau}_v = \vec{\tau}_{tot} - \rho_w \int_{\sigma_{min}}^{\sigma_z} \int_0^{2\pi} \beta_g(\sigma, \theta) \sigma^2 N(\sigma, \theta) \frac{\vec{\kappa}}{\kappa} d\theta d\sigma \tag{8.1}$$

The above equation includes both the frequencies up to σ_{max} and the frequencies above it. So, the first integral can be written as two:

$$\int_{\sigma_{min}}^{\sigma z} \rightarrow \int_{\sigma_{min}}^{\sigma max} + \int_{\sigma_{max}}^{\sigma z} \tag{8.2}$$

The first part of the integral (up to σ_{max}) is computed by the discretised spectrum, but the second part (above σ_{max}) is computed by artificially extending the spectrum to a very high frequency (10Hz). In addition to that, the scheme uses a high number of iterations in order for that wind profile as calculated from the WBLM to match the wind at 10m from the atmosphere. So, there are two reasons for the high cost of the WBLM approach: 1) the extension to 10 Hz and 2) the iteration process to get the new wind profile.

The goal here was to find an approximation for the integral $\int_{\sigma_{max}}^{\sigma_z}$ (from now on called I_{HF}) of:

$$I_{HF} = \rho_w \int_{\sigma_{max}}^{\sigma_z} \int_0^{2\pi} \beta_g(\sigma, \theta) \sigma^2 N(\sigma, \theta) \frac{\vec{\kappa}}{\kappa} d\theta d\sigma \tag{8.3}$$

which then gives 8.1 written as:

$$\vec{\tau}_v = \vec{\tau}_{tot} - \rho_w \int_{\sigma_{min}}^{\sigma_{max}} \int_0^{2\pi} \beta_g(\sigma, \theta) \sigma^2 N(\sigma, \theta) \frac{\vec{\kappa}}{\kappa} d\theta d\sigma - I_{HF} \tag{8.4}$$

with,

$$I_{HF} = \rho_w \int_{\sigma_{max}}^{\sigma_\nu} \int_0^{2\pi} \beta_g(\sigma, \theta) \sigma^2 N(\sigma, \theta) \frac{\vec{\kappa}}{\kappa} d\theta d\sigma \tag{8.5}$$

for $z_\nu < z < \frac{g\delta}{\sigma_{max}}$, where $z_\nu = 0.1 \frac{\nu_a}{\sqrt{|\vec{\tau}_\nu / \rho_\alpha|}}$

The issue is that for calculating I_{HF}, $\vec{\tau}_\nu$ is required, but also $\vec{\tau}_\nu$ is needed to determine z_ν through I_{HF}. This means that a different iteration process may also be needed here, for starting from a given σ_ν.

However, in case of a given σ_ν we want to know if a simplified expression for I_{HF} can be extracted. In default version of ECWAM, for all frequencies above σ_{max}, the spectrum is assumed to decay as $\frac{1}{\sigma^5}$. So,

$$N(\theta, \sigma) = \frac{F(\theta, \sigma)}{\sigma} = \frac{\sigma_{max}^5}{\sigma^5}\frac{F(\theta, \sigma_{max})}{\sigma} \tag{8.6}$$

for all $\sigma > \sigma_{max}$

Because σ_{max} is high enough, I_{HF} can be considered to be mostly in the wind direction. Meaning $\kappa = \kappa(cos(\theta - \phi), 0)$, where ϕ is the wind direction.

So according to Equation 3.34 β_g can be expressed as:

$$\beta_g(\sigma, \theta) = C_\beta \sigma \frac{\rho_\alpha}{\rho_w}(\frac{u_*^l}{c})^2 max(cos(\theta - \phi), \phi)^2 \tag{8.7}$$

with,

$$c_\beta = \frac{\beta_{max}}{k^2}\lambda ln^4 \lambda \tag{8.8}$$

and

$$\lambda = \frac{gz_0}{c^2}exp[\frac{\kappa}{(\frac{u_*^l}{c} + z_\alpha)cos(\theta - \phi)}] \tag{8.9}$$

According to Janssen (1991) approach $\lambda ln^4\lambda$ is independent of direction for high frequencies. Then to compute the high frequency part of the wave induced stress See also ECMWF (2020):

$$\lambda = \frac{gz_0}{c^2}exp[\frac{\kappa}{\frac{u_*}{c} + z_\alpha}] \tag{8.10}$$

and we have,

$$I_{HF} = \rho_\alpha \sigma_{max}^5 \int_0^{2\pi} F(\theta, \sigma_{max}) max(cos(\theta - \phi), 0)^3 d\theta * \frac{\beta_{max}}{\kappa^2} \int_{\sigma_{max}}^{\sigma_v} \frac{(u'_*)^2}{c^2} \frac{1}{\sigma_3} \lambda ln^4 \lambda d\sigma \tag{8.11}$$

Because waves are short and deep water dispersion relation can be assumed, we then consider:

$c = \frac{\sigma}{\kappa}$ and $\sigma^2 = g\kappa$

so,

$c = \frac{g}{\sigma}$, with $\sigma = 2\pi f$

The above results in:

$$I_{HF} = \frac{\rho_a}{g^2} (2\pi)^5 f_{max}^5 \int_0^{2\pi} F(\theta, \sigma_{max}) [max(cos(\theta - \phi), 0)]^3 d\theta * \frac{\beta_{max}}{k^2} \int_{\sigma_{max}}^{\sigma_\nu} (u'_*)^2 \frac{1}{\sigma} \lambda ln^4 \lambda d\sigma \tag{8.12}$$

Converting Eq. 8.12 to the actual frequency the model calculates $F(\theta, f)$, where f is the actual frequency, which is $F(\theta, \sigma) = \frac{F(\theta, f)}{2\pi}$

Therefore:

$$I_{HF} = \frac{\rho_a}{g^2} (2\pi)^4 f_{max}^5 \int_0^{2\pi} F(\theta, f_{max}) [max(cos(\theta - \phi), 0)]^3 d\theta * \frac{\beta_{max}}{k^2} \int_{\sigma_{max}}^{\sigma_\nu} (u^l_*)^2 \frac{\lambda ln^4 \lambda}{\sigma} d\sigma \tag{8.13}$$

One of main differences is that u^l_* is also calculated over frequencies, and for this reason it is passed in the integral.

Since,

$$(u^l_{*(\sigma)})^2 = (u^l_{*(\sigma_{max})})^2 - \int_{\sigma_{max}}^{\sigma} \frac{d\sigma'}{\sigma'} \lambda ln^4 \lambda \tag{8.14}$$

the final I_{HF} can be resolved numerically as:

$$I_{HF} = \frac{\rho_\alpha}{g^2}(2\pi)^4 f_{max}^5 \int_0^{2\pi} F(\theta, f_{max})[max(cos(\theta - \phi), 0)]^3 d\theta * \frac{\beta_{max}}{k^2} \int_{\sigma_{max}}^{\sigma_\nu} (u_*^l(\sigma)^2) \frac{\lambda ln^4 \lambda}{\sigma'} d\sigma' \tag{8.15}$$

However, in all cases, $\lambda \leq 1$, which means that there is an upper bound limit for σ'.

According to Equation 8.9:

$$\lambda = \frac{g z_0}{c^2} exp[\frac{k}{\frac{u_*}{c} + z_\alpha}] \tag{8.16}$$

This means that the exponential is always ≥ 1, the upper bound for $\lambda = 1$ is when $\lambda = \frac{g z_0}{c^2} = 1$ with, $c = g/\sigma'$ therefore, $\lambda = 1$ only when $\sigma' = \sqrt{\frac{g}{z_0}}$ so, the last part of Equation 8.15 is:

$$\frac{\beta_{max}}{k^2} \int_{\sigma_{max}}^{\sigma_\nu} (u_*^l)^2 \frac{\lambda ln^4 \lambda}{\sigma'} d\sigma' \tag{8.17}$$

can now be written as:

$$\frac{\beta_{max}}{k^2} \int_{\sigma_{max}\sqrt{\frac{z\phi}{g}}}^{min(1, \sigma_\nu \sqrt{\frac{z_0}{g}})} (u_*^l)^2 \lambda ln^4 \lambda \frac{dY}{Y} \tag{8.18}$$

where, $Y = \sigma' \sqrt{\frac{z_0}{g}}$.

Finally, as mentioned in the IFS documentation, it can be seen that it is more efficient to take into consideration that the lower bound of the integral is not always $\sigma_{max}\sqrt{\frac{z_0}{g}}$, but $max(\sigma_{max}\sqrt{\frac{z_0}{g}}, x_0 \frac{g}{u_*}\sqrt{\frac{z_0}{g}})$, where $x_0 \sim 0.05$.

That can be explained as

$$\lambda = \frac{g z_0}{c^2} exp[\frac{\kappa}{\frac{u_*}{c} + z_\alpha}] \tag{8.19}$$

with, $c = \frac{g}{\sigma}$ and $z_0 = \frac{\alpha u_*^2}{g}$, where α is the Charnock coefficient. Then,

$$\lambda = \alpha \frac{\sigma}{g/u_*} exp[\frac{\kappa}{\frac{\sigma}{g/u_*} + z_\alpha}] \tag{8.20}$$

but again, $\lambda \leq 1$. So, numerically one can find for which value of $x = \frac{\sigma}{g/u_*}$,

$$\alpha x^2 exp(\frac{\kappa}{x + z_\alpha}) = 1 \tag{8.21}$$

where for typical values of α and z_α $x = x_0 \sim 0.05$.

Then, following one extra change of variable $X = ln(Y)$, Equation 8.18 it can be numerically evaluated efficiently, using the Simpson integration method with few ($\sim$ 13) points to discretise the interval over which the integration is computed (ECMWF, 2020).

So, based on all the above, Du et al. (2017, 2019) scheme requires the computation of τ_ν using frequencies above σ_{max}. In order to do so, the scheme artificially extends the discretised spectra beyond σ_{max}, using a large number of frequencies (10Hz). Here, we have described how using the same approach used by Janssen (1991), the contribution of the high frequencies integral Eq. 8.1 for all components above σ_{max} can be reduced to the product of two one-dimensional integrals: one over discredited directions and one over a rescaled frequency range. The latter integral should be computed numerically with only a few points. The scheme will still need to be integrated since one has to start with an estimation of z_ν based on viscous stress. However, this new way can reduce the number of iterations and the cost. It can also help on the resolution above σ_{max}, resulting in more accurate predictions.

8.3 Thesis Conclusions

This thesis presented the implementation and validation of the new wind input source function parameterisation approach introduced recently by Du et al.

(2017, 2019). This approach has been previously introduced to a different wave model (SWAN), in order to improve the calculation of the drag and Charnock coefficients (C_d, α) and as a results the improvement of wind and wave predictions. However, the scheme has not being tested in a coupled system, and important evaluation of both its abilities on prediction of different extreme case studies and its computational cost has not been discussed before. Here the OpenIFS system is used, with its fully coupled option. This model does not requires a coupler, but the wave model is part of the system as subroutines. In this way errors during the passage of the stresses between the atmosphere and the ocean through any coupler are avoided.

The scheme uses the Wave Boundary Layer Model (WBLM) in order to fully calculate the wind profile and the stresses for each height (frequency). In this way, the model does not assume a logarithmic profile. The scheme needs to be integrated to very high frequencies by artificially extending the discretized frequencies to very high values (10Hz), using iterations in order to achieve the convergence of the scheme.

The implementation of the scheme and all simulations are done with the OpenIFS cycle 40r1v2. This version was released in October 2018, and was the open access of the operational IFS cycle40r1 model of the European Centre for Medium-range Weather Forecasts (ECMWF). The version remained operational from the 19th of November 2013 to 12th of May 2015. The specific model was chosen since it is one of the most tested models, and one of the limited number of models that fully couples the atmosphere with the ocean wind waves, including the wave model (ECWAM) as subroutines inside the modelling system. The resolution of the specific version is TL1279 (16km) for the atmospheric model and 0.25 degrees (28km) for the wave model, and it can extent to 91 or 137 vertical levels. In this project, the focus is on the boundary layer simulations using 91 vertical levels, since using 137 will only increase the computational cost with no impact on the results (the extra levels are in the stratosphere).

The initial conditions of a lower impact mid-latitude storm (Storm Ciara, initial conditions 6 of February 2020) and a different first guess of drag coefficient Edson et al. (2013) were used in order to test the stability of the model. This case was ran for five forecast days. The main analysis and validation of the WBLM is done using four initial conditions datasets. These are; 02 September 2019, 04 September 2019, 24 August 2020, and 17 September 2020. These dates were chosen based on knowledge of tropical cyclone activity, either in the Atlantic (hurricanes Dorian with peak winds around the 6-7th of September 2019 and hurricane Teddy with peak winds on the 21st of September of 2020) or over the Yellow sea (typhoon Lingling with peak winds on the 7th of September 2019 and typhoon Bavi with peak winds on the 26th of August 2020). Again, both global domain runs and cyclone domain focused runs were performed. All the above cases ran for seven days of forecast.

Model results, were compared against the default (reference) parameterisation of Janssen (1991), as well as against in-situ (mooring and drifting buoys) and altimeter data from four (4) satellites (CryoSat-2, Jason-3, Sentinel-3a and Sentinel-3b). The default parameterisation is used as a reference, in order to better understand the impact and potential improvements that the new approach offers.

The main research findings that emerged from the implementation and evaluation of the WBLM can be summarized below:

1 Upon examining the impact of the implementation of the new WBLM source input function approach, results showed that WBLM reduces the drag coefficient and Charnock coefficient globally compared to Janssen's scheme. Simulations showed that the drag coefficient (C_d) is significantly reduced when the WBLM is used in the wind input source function. That is more evident for high and extreme winds. In the most cases the WBLM was closer to the mean values, while Janssen's scheme has a lot of spread around the mean. In extreme conditions, the WBLM was found to reduce the values of the drag coefficient by about 0.001. For moderate to high wind speeds, the Charnock coefficient values are in some cases half than the corresponding values calculated form Janssen's scheme. Maximum values from the WBLM are around 0.05 and from Janssen they are 0.1. In wind speeds of extreme values, where the tropical cyclone events are included, the reduction of Charnock shows a similar trend. The highest values reach 0.025 when the WBLM is used, and 0.055 when for the Janssen parameterisation is used. These come with an agreement with previous and recent studies in the literature.

2 The spacial distribution of global wind speeds has shown the shift of the winds towards higher winds, which can be explained from the decrease of the surface stress (C_d). More specifically, it is shown that WBLM for low to moderate winds (up to 12m/s) wind density is higher. For high winds (>20m/s), using WBLM decreases the wind density. It is found that extreme values of wind speeds (>30m/s) showed an increase, when the WBLM is used. In general, the direction distribution was insensitive to the source input function. Focusing on the areas of the extreme events, it was shown that the WBLM increased the underestimated wind speeds from Janssen's scheme, by more than 4 m/s. The significant wave heights are generally decreased, while in places some increases were found.

3 The validation of the WBLM scheme with the best-track observations showed that WBLM does not change significantly the path of the cyclones with respect to the reference scheme, as trajectory highly depends on the forecast lead time and the along track errors. Most issues were found for the typhoon Bavi case study. In all cases when the model is few days into the forecast, the trajectories from the models are less reliable compared to the real trajectories. Validation with buoy data showed that in many cases the WBLM improves the wind speed and significant wave height predictions. However, the default parameterisation of Janssen captured the significant wave and wind conditions more accurately in cases. Basic statistical analysis based on Taylor plots and corresponding statistics tables showed that the typhoon cases (Lingling and Bavi) WBLM generally gives more successful predictions of significant wave height. For the hurricane cases (Dorian and Teddy), in some locations the use of WBLM improves the predictions, while in other places, Janssen is more successful. However, when Janssen agreed better with the predictions, statistics showed that the differences with the WBLM were not significant, while there are cases, such as buoy 41013 for hurricane Dorian, where RMSE is significantly lowered when the WBLM is used. Finally, in almost all cases WBLM has improved the scatter around the mean (low variability), as the standard deviation is lower when the WBLM was used for the simulations.

4 Overall, validation of the model outputs with in-situ and altimeter data showed mixed forecast skill with improvement/degradation with generally better STD and RMSE for WBLM compare to the default parameterisation. The validation of the model simulations for 10m wind speed and the significant wave height, based on altimeter data, showed that the WBLM underestimated both the significant wave height and the wind speed, for all case studies. It was also found that in some cases, Janssen's scheme gave better predictions of wind speeds and significant wave height, where in other cases WBLM was more successful. These results also supported the findings from the validation with buoys, where the WBLM in most cases gave lower standard deviations compare to the default parameterisation. Hence, when the WBLM is used the big scatter around the mean was corrected. In addition, it was found that observations always have the highest standard deviation, even if the the data had passed quality control, and during the analysis techniques to avoid outliers were also used. From the case studies, hurricane Teddy gave the worst stability around the mean. Comparing the different satellites, Jason-3 seemed to give the worst stability around the mean, as the standard deviations displayed the highest values. That could be natural variability, but also false measurements. It is noted that this variation if it holds errors can falsely improve the entire forecast.

5 Another important point is that the scheme was found to be stable. Different choices of first guess parameterisations of the drag coefficient did not significantly change the model outputs. That means that the WBLM can generally be considered reliable.

6 The computational cost of the WBLM is larger and can be deemed a limitation for its application in forecasting systems. As explained in the methodology chapter (Chapter 3) the scheme works in order to calculate the viscous stress (τ_ν) using frequencies above the maximum point (σ_{max}). The model needs a large number of frequencies (10Hz) by artificially extending the disctelised spectra beyond σ_{max}. Moreover, the scheme needs to be iterated in order to determine the boundary layer wind speed profile. These characteristics together with the extended frequency range significantly increases the computational cost (by 3 hours). In addition to that, there are many times that the convergence criteria are not reached and issues occur in the model's accuracy. Here, we suggest a way in order to work out the high frequencies, using the f^{-5} tail, as in Janssen (1991). The scheme will still be integrated since one has to start with an estimation of of z_ν based on viscous stress. However, this new way, could be found to reduce the number of iterations and the cost. It could also help with the resolution above σ_{max}, and as a result improve the predictions of wind speeds and wave heights. This needs more investigation, and it is suggested as future work.

Bibliography

Ardhuin, F., Rogers, E., Babanin, A. V., Filipot, J.-F., Magne, R., Roland, A., van der Westhuysen, A., Queffeulou, P., Lefevre, J.-M., Aouf, L. and Collard, F. (2010), 'Semiempirical Dissipation Source Functions for Ocean Waves. Part I: Definition, Calibration, and Validation', *Journal of Physical Oceanography* **40**(9), 1917–1941.

Arya, S. P. (2001), *Introduction to Micrometeorology*, 2 edn, Academic Press.

Babanin, A., Tsagareli, K., Young, I. and Walker, D. (2010), 'Numerical investigation of spectral evolution of wind waves. part ii: Dissipation term and evolution tests', *Journal of Physical Oceanography* **40**, 667–683.

Banner, M. L. and Morison, R. P. (2010), 'Refined source terms in wind wave models with explicit wave breaking prediction. Part I: Model framework and validation against field data', *Ocean Modelling* **33**(1), 177–189.

Bao, J. W., Wilczak, J. M., Choi, J. K. and Kantha, L. H. (2000), 'Numerical Simulations of Air Sea Interaction under High Wind Conditions Using a Coupled Model: A Study of Hurricane Development', *Monthly Weather Review* **128**(7), 2190.

Belcher, S. E. and Hunt, J. C. R. (1993), 'Turbulent shear flow over slowly moving waves', *Journal of Fluid Mechanics* **251**, 109–148.

Bidlot, J.-R. (2012), 'Present Status of Wave Forecasting at ECMWF', *ECMWF* .

URL: *http://www.ecmwf.int/research/ifsdocs/*

Bidlot, J. R., Prates, F., Ribas, R., Mueller-Quintino, A., Crepulja, M. and Vitart, F. (2020), 'Enhancing tropical cyclone wind forecasts', *ECMWF newsletter* **164**, 33–37.

URL: *https://www.ecmwf.int/sites/default/files/elibrary/2020/19721-enhancing-tropical-cyclone-wind-forecasts.pdf*

Bolaños-Sanchez, R., Sanchez-Arcilla, A. and Cateura, J. (2007), 'Evaluation of two atmospheric models for wind wave modelling in the NW Mediterranean', *Journal of Marine Systems* **65**(1-4), 336–353.

Booij, N., Ris, R. C. and Holthuijsen, L. H. (1999), 'A third-generation wave model for coastal regions: 1. Model description and validation', **104**(C4), 7649–7666.

Charnock, H. (1955), 'Wind stress on a water surface', *Quarterly Journal of the Royal Meteorological Society* **81**(350), 639–640.

Charnock, H. (1958), 'A note on empirical wind-wave formulae', *Quarterly Journal of the Royal Meteorological Society* **84**(362), 443–447.
URL: *https://onlinelibrary.wiley.com/doi/full/10.1002/qj.49708436212 https://onlinelibrary.wiley.com/doi/abs/10.1002/qj.49708436212 https://rmets.onlinelibrary.wiley.com/doi/10.1002/qj.49708436212*

Chen, G. and Belcher, S. E. (2000), 'Effects of Long Waves on Wind-Generated Waves', *Journal of Physical Oceanography* **30**(9), 2246–2256.

Chen, Y. and Yu, X. (2016), 'Enhancement of wind stress evaluation method under storm conditions', *Climate Dynamics* **47**(12), 3833–3843.

Christakos, K., Furevik, B. R., Aarnes, O. J., Breivik, Ø., Tuomi, L. and Byrkjedal, Ø. (2020), 'The importance of wind forcing in fjord wave modelling', *Ocean Dynamics* **70**(1), 57–75.

Csanady, G. T. (2001), *Air-Sea Interaction: Laws and Mechanisms*, Cambridge Univ. Press.
URL: *http://www.meteoclub.gr/proo1/Air-Sea Interaction Laws and Mechanisms_ISBN0521796806.pdf*

Curcic, M. and Haus, B. K. (2020), 'Revised Estimates of Ocean Surface Drag in Strong Winds', **47**(10), e87647.

Donelan and A., M. (1990), 'Air-sea interaction', *The Sea* **9**, 239–292.
URL: *https://ci.nii.ac.jp/naid/10022553099/*

Donelan, M. A., Haus, B. K., Reul, N., Plant, W. J., Stiassnie, M., Graber, H. C., Brown, O. B. and Saltzman, E. S. (2004), 'On the limiting aerodynamic roughness of the ocean in very strong winds', **31**(18), L18306.

Doyle, J. D. (2002), 'Coupled Atmosphere Ocean Wave Simulations under High Wind Conditions', *Monthly Weather Review* **130**(12), 3087.

Drennan, W. M., Graber, H. C., Hauser, D. and Quentin, C. (2003), 'On the wave age dependence of wind stress over pure wind seas', *Journal of Geophysical Research* **108**(C3), 8062.
URL: *http://doi.wiley.com/10.1029/2000JC000715*

Du, J., Bolaños, R. and Guo Larsén, X. (2017), 'The use of a wave boundary layer model in SWAN', *Journal of Geophysical Research (Oceans)* **122**(1), 42–62.

Du, J., Bolaños, R., Larsén, X. G. and Kelly, M. (2019), 'Wave boundary layer model in SWAN revisited', *Ocean Science* **15**(2), 361–377.

ECMWF (2013), 'IFS Documantation', https://www.ecmwf.int/en/forecasts/documentation-and-support/changes-ecmwf-model/cycle-40r1/cycle-40r1. [Online; accessed 15-September-2021].

ECMWF (2020), 'Part VII: ECMWF wave model, in IFS Documentation CY47R1', https://www.ecmwf.int/en/elibrary/19311-part-vii-ecmwf-wave-model. [Online; accessed 20-November-2021].

ECMWF (2021), 'Tropical cyclone activities at ECMWF', https://www.ecmwf.int/en/elibrary/20228-tropical-cyclone-activities-ecmwf. [Online; accessed 11-January-2022].

Edson, J. B., Jampana, V., Weller, R. A., Bigorre, S. P., Plueddemann, A. J., Fairall, C. W., Miller, S. D., Mahrt, L., Vickers, D. and Hersbach, H. (2013), 'On the Exchange of Momentum over the Open Ocean', *Journal of Physical Oceanography* **43**(8), 1589–1610.
URL: *http://journals.ametsoc.org/doi/abs/10.1175/JPO-D-12-0173.1*

Fan, Y., Ginis, I., Hara, T., Wright, C. W. and Walsh, E. J. (2009), 'Numerical simulations and observations of surface wave fields under an extreme tropical cyclone', *Journal of Physical Oceanography* **39**(9), 2097–2116.
URL: *http://argo.colorado.edu/*

Foreman, R. J. and Emeis, S. (2010), 'Revisiting the Definition of the Drag Coefficient in the Marine Atmospheric Boundary Layer', *Journal of Physical Oceanography* **40**(10), 2325–2332.

Furevik, B. R. and Haakenstad, H. (2012), 'Near-surface marine wind profiles from rawinsonde and NORA10 hindcast', *Journal of Geophysical Research: Atmospheres* **117**(D23), n/a–n/a.
URL: *http://doi.wiley.com/10.1029/2012JD018523*

Gentile, E. S., Gray, S. L. and Lewis, H. W. (2021), 'The sensitivity of probabilistic convective-scale forecasts of an extratropical cyclone to atmosphere-ocean-wave coupling', *Quarterly Journal of the Royal Meteorological Society* .
URL: *https://onlinelibrary.wiley.com/doi/full/10.1002/qj.4225 https://onlinelibrary.wiley.com/doi/abs/10.1002/qj.4225 https://rmets.onlinelibrary.wiley.com/doi/10.1002/qj.4225*

Hara, T. and Belcher, S. E. (2002), 'Wind forcing in the equilibrium range of wind-wave spectra', *Journal of Fluid Mechanics* **470**(1), 223–245.

Hara, T. and Belcher, S. E. (2004), Wind profile and drag coefficient over mature and growing ocean surface wave spectra, *in* 'EGS - AGU - EUG Joint Assembly', EGS - AGU - EUG Joint Assembly, p. 7504.

Hasselmann, K., Barnett, T., Bouws, E., Carlson, H., Cartwright, D., Enke, K., Ewing, J., Gienapp, H., Hasselmann, D., Kruseman, P., Meerburg, A., Müller, P., Olbers, D., Richter, K., Sell, W. and Walden, H. (1973), 'Measurements of wind-wave growth and swell decay during the Joint North Sea Wave Project (JONSWAP)', *Ergänzungsheft 8-12* .
URL: *https://repository.tudelft.nl/islandora/object/uuid%3Af204e188-13b9-49d8-a6dc-4fb7c20562fc*

Hristov, T. S., Miller, S. D. and Friehe, C. A. (2003), 'Dynamical coupling of wind and ocean waves through wave-induced air flow', *Nature* **422**(6927), 55–58.
URL: *http://www.nature.com/articles/nature01382*

Janssen, P. (2004), *The Interaction of Ocean Waves and Wind*, Cambridge University Press.
URL: *https://books.google.co.uk/books?id=Rb0fRcrTiBUC*

Janssen, P. A. E. M. (1991), 'Quasi-linear Theory of Wind-Wave Generation Applied to Wave Forecasting', *Journal of Physical Oceanography* **21**(11), 1631–1642.

Janssen, P. A. E. M., Lionello, P. and Zambresky, L. (1989), 'On the Interaction of Wind and Waves', *Philosophical Transactions of the Royal Society of London Series A* **329**(1604), 289–301.

Jenssen, P. and Cardone, V. J. (2006), Performance of third generation wave models in extreme hurricanes, *in* 'paper presented in 9th International Wind and Wave Workshop', Vol. 54, p. 258.

Johnson, H. K., Vested, H. J., Hersbach, H., Højstrup, J. and Larsen, S. E. (1999), 'The Coupling between Wind and Waves in the WAM Model', *Journal of Atmospheric and Oceanic Technology* **16**(11), 1780.

Komen, G. J., Cavaleri, L., Donelan, M., Hasselmann, K., Hasselmann, S. and Janssen, P. A. E. M. (1994), *Dynamics and Modelling of Ocean Waves*, Cambridge University Press, Cambridge.
URL: *http://ebooks.cambridge.org/ref/id/CBO9780511628955*

Komen, G. J., Hasselmann, S. and Hasselmann, K. (1984), 'On the Existence of a Fully Developed Wind-Sea Spectrum', *Journal of Physical Oceanography* **14**(8), 1271–1285.

Kudryavtsev, V. N., Makin, V. K. and Chapron, B. (1999), 'Coupled sea surface-atmosphere model: 2. Spectrum of short wind waves', **104**(C4), 7625–7639.

Li, D., Staneva, J., Bidlot, J.-R., Grayek, S., Zhu, Y. and Yin, B. (2021), 'Improving regional model skills during typhoon events: A case study for super typhoon lingling over the northwest pacific ocean', *Frontiers in Marine Science* **8**, 42.
URL: *https://www.frontiersin.org/article/10.3389/fmars.2021.613913*

Liu, B., Liu, H., Xie, L., Guan, C., Zhao, D., Liu, B., Liu, H., Xie, L., Guan, C. and Zhao, D. (2011), 'A Coupled Atmosphere–Wave–Ocean Modeling System: Simulation of the Intensity of an Idealized Tropical Cyclone', *Monthly Weather Review* **139**(1), 132–152.
URL: *http://journals.ametsoc.org/doi/abs/10.1175/2010MWR3396.1*

Liu, Q., Lewis, T., Zhang, Y. and Sheng, W. (2015), 'Performance assessment of wave measurements of wave buoys', *International Journal of Marine Energy* **12**, 63–76.

Makin, V. K., Branger, H., Peirson, W. L. and Giovanangeli, J. P. (2007), 'Stress above Wind-Plus-Paddle Waves: Modeling of a Laboratory Experiment', *Journal of Physical Oceanography* **37**(12), 2824.

Makin, V. K. and Kudryavtsev, V. N. (1999), 'Coupled sea surface-atmosphere model: 1. Wind over waves coupling', **104**(C4), 7613–7623.

Miles, J. W. (1957), 'On the generation of surface waves by shear flows', *Journal of Fluid Mechanics* **3**, 185–204.

Monin, A. S. and Obukhov, A. M. (1954), 'Basic laws of turbulent mixing in the surface layer of the atmosphere', *Originally published in Tr. Akad. Nauk SSSR Geophiz. Inst* **24**(151), 163–187.

Moon, I.-J. (2005), 'Impact of a coupled ocean wave-tide-circulation system on coastal modeling', *Ocean Modelling* **8**(3), 203–236.

Moon, I.-J., Hara, T., Ginis, I., Belcher, S. E. and Tolman, H. L. (2004), 'Effect of Surface Waves on Air Sea Momentum Exchange. Part I: Effect of Mature and Growing Seas.', *Journal of Atmospheric Sciences* **61**(19), 2321–2333.

Moon, I.-J., Kwon, J.-I., Lee, J.-C., Shim, J.-S., Kang, S. K., Oh, I. S. and Kwon, S. J. (2009), 'Effect of the surface wind stress parameterization on the storm surge modeling', *Ocean Modelling* **29**(2), 115–127.

Peng, S., Li, Y. and Xie, L. (2013), 'Adjusting the Wind Stress Drag Coefficient in Storm Surge Forecasting Using an Adjoint Technique', *Journal of Atmospheric and Oceanic Technology* **30**(3), 590–608.
URL: *http://journals.ametsoc.org/doi/abs/10.1175/JTECH-D-12-00034.1*

Phillips, O. M. (1957), 'On the generation of waves by turbulent wind', *Journal of Fluid Mechanics* **2**, 417–445.

Pineau-Guillou, L., Ardhuin, F., Bouin, M., Redelsperger, J., Chapron, B., Bidlot, J. and Quilfen, Y. (2018), 'Strong winds in a coupled wave–atmosphere model during a North Atlantic storm event: evaluation against observations', *Quarterly Journal of the Royal Meteorological Society* **144**(711), 317–332.
URL: *https://onlinelibrary.wiley.com/doi/abs/10.1002/qj.3205*

Ryglicki, D. R., Doyle, J. D., Hodyss, D., Cossuth, J. H., Jin, Y., Viner, K. C. and Schmidt, J. M. (2019), 'The Unexpected Rapid Intensification of Tropical Cyclones in Moderate Vertical Wind Shear. Part III: Outflow-Environment Interaction', *Monthly Weather Review* **147**(8), 2919–2940.

Stull, R. B. (1988), *An introduction to boundary layer meteorology.*

Taylor, K. (2001), 'Summarizing multiple aspects of model performance in a single diagram', *Journal of Geophysical Research* **106**, 7183–7192.

Taylor, P. D. (2003), 'Momentum, Heat, and Vapor Fluxes', *Encyclopedia of Atmospheric Sciences* pp. 93–100.

Taylor, P. K. and Yelland, M. J. (2001), 'The Dependence of Sea Surface Roughness on the Height and Steepness of the Waves', *Journal of Physical Oceanography* **31**(2), 572–590.

Tolman, H. L. and Chalikov, D. (1996), 'Source Terms in a Third-Generation Wind Wave Model', *Journal of Physical Oceanography* **26**(11), 2497–2518.

Valiente, N. G., Saulter, A., Edwards, J. M., Lewis, H. W., Castillo Sanchez, J. M., Bruciaferri, D., Bunney, C. and Siddorn, J. (2021), 'The impact of wave model source terms and coupling strategies to rapidly developing waves across the north-west european shelf during extreme events', *Journal of Marine Science and Engineering* **9**(4).
URL: *https://www.mdpi.com/2077-1312/9/4/403*

Varlas, G., Katsafados, P., Papadopoulos, A. and Korres, G. (2018), 'Implementation of a two-way coupled atmosphere-ocean wave modeling system for assessing air-sea interaction over the Mediterranean Sea', *Atmospheric Research* **208**, 201–217.
URL: *https://www.sciencedirect.com/science/article/pii/S0169809517305860*

Webster, P. J., Holland, G. J., Curry, J. A. and Chang, H. R. (2005), 'Atmospheric science: Changes in tropical cyclone number, duration, and intensity in a warming environment', *Science* **309**(5742), 1844–1846.
URL: *www.sciencemag.org/cgi/content/full/309/5742/1841/*

Wu, J. (1982), 'Wind-Stress Coefficients Over Sea Surface From Breeze to Hurricane', **87**(C12), 9704–9706.

Wu, Z.-y., Jiang, C.-b., Deng, B., Chen, J., Cao, Y.-g. and Li, L.-j. (2018), 'Evaluation of numerical wave model for typhoon wave simulation in South China Sea', *Water Science and Engineering* **11**(3), 229–235.
URL: *https://www.sciencedirect.com/science/article/pii/S167423701830070X*

Xiande, Z., Lixin, W. U. and Qi, W. (2018), 'Extratropical Transition and Re-Intensification of Typhoon Toraji (2001): Large-Scale Circulations, Structural Characteristics, and Mechanism Analysis', *J. Ocean Univ. China (Oceanic and Coastal Sea Research* **17**(3), 461–476.
URL: *http://www.ouc.edu.cn/xbywb/*

Yang, J., Zhang, J., Jia, Y., Fan, C. and Cui, W. (2020), 'Validation of Sentinel-3A/3B and Jason-3 Altimeter Wind Speeds and Significant Wave Heights Using Buoy and ASCAT Data', *Remote Sensing* **12**(13), 2079.

Zabolotskikh, E. V., Mitnik, L. M. and Chapron, B. (2013), 'New approach for severe marine weather study using satellite passive microwave sensing', *Geophysical Research Letters* **40**(13), 3347–3350.
URL: *https://agupubs.onlinelibrary.wiley.com/doi/abs/10.1002/grl.50664*

Zieger, S., Babanin, A. V., Erick Rogers, W. and Young, I. R. (2015), 'Observation-based source terms in the third-generation wave model WAVEWATCH', *Ocean Modelling* **96**, 2–25.

Zijlema, M., van Vledder, G. and Holthuijsen, L. (2012), 'Bottom friction and wind drag for wave models', *Coastal Engineering* **65**, 19–26.
URL: *https://www.sciencedirect.com/science/article/pii/S0378383912000440*